

## **ABSTRACT**

Title of dissertation:

**PURITY MONITORING TECHNIQUES AND ELECTRONIC  
XENON TIME PROJECTION CHAMBERS**

**Jon Balajthy, Doctor of Philosophy, 2017**

Dissertation directed by:

**Professor Carter Hall  
University of Maryland**

PURITY MONITORING TECHNIQUES AND ELECTRONIC ENERGY DEPOSITION  
XENON TIME PROJECTION CHAMBERS

by

Jon Balajthy

Dissertation submitted to the Faculty of the Graduate School of the  
University of Maryland, College Park in partial fulfillment  
of the requirements for the degree of  
Doctor of Philosophy  
2017

Advisory Committee:  
Professor Carter Hall, Chair/Advisor

© Copyright by  
Jon Balajthy  
2017

## Preface

Lorem ipsum dolor sit amet, consectetuer adipiscing elit. Ut purus elit, vestibulum ut, placerat ac, adipiscing vitae, felis. Curabitur dictum gravida mauris. Nam arcu libero, nonummy eget, consectetuer id, vulputate a, magna. Donec vehicula augue eu neque. Pellentesque habitant morbi tristique senectus et netus et malesuada fames ac turpis egestas. Mauris ut leo. Cras viverra metus rhoncus sem. Nulla et lectus vestibulum urna fringilla ultrices. Phasellus eu tellus sit amet tortor gravida placerat. Integer sapien est, iaculis in, pretium quis, viverra ac, nunc. Praesent eget sem vel leo ultrices bibendum. Aenean faucibus. Morbi dolor nulla, malesuada eu, pulvinar at, mollis ac, nulla. Curabitur auctor semper nulla. Donec varius orci eget risus. Duis nibh mi, congue eu, accumsan eleifend, sagittis quis, diam. Duis eget orci sit amet orci dignissim rutrum.

## Foreword

Lorem ipsum dolor sit amet, consectetuer adipiscing elit. Ut purus elit, vestibulum ut, placerat ac, adipiscing vitae, felis. Curabitur dictum gravida mauris. Nam arcu libero, nonummy eget, consectetuer id, vulputate a, magna. Donec vehicula augue eu neque. Pellentesque habitant morbi tristique senectus et netus et malesuada fames ac turpis egestas. Mauris ut leo. Cras viverra metus rhoncus sem. Nulla et lectus vestibulum urna fringilla ultrices. Phasellus eu tellus sit amet tortor gravida placerat. Integer sapien est, iaculis in, pretium quis, viverra ac, nunc. Praesent eget sem vel leo ultrices bibendum. Aenean faucibus. Morbi dolor nulla, malesuada eu, pulvinar at, mollis ac, nulla. Curabitur auctor semper nulla. Donec varius orci eget risus. Duis nibh mi, congue eu, accumsan eleifend, sagittis quis, diam. Duis eget orci sit amet orci dignissim rutrum.

## Dedication

## Acknowledgments

## Table of Contents

Preface	ii
Foreword	iii
Dedication	iv
Acknowledgements	v
1 Cosmology Overview	1
1.1 Standard Model of Cosmology	1
1.2 The Cosmic Microwave Background	4
1.3 Dark Matter	5
1.3.1 Galaxy Clusters	6
1.3.2 Galactic Rotation Curves	7
1.3.3 Modified Newtonian Dynamics	10
1.3.4 Gravitational Lensing	10
1.4 Dark Matter Candidates	12
1.4.1 Baryonic Dark Matter	12
1.4.2 Neutrinos	13
1.4.3 Axions	13
1.4.4 WIMPs	16
1.5 WIMP Direct Detection	19
1.5.1 Cross Section	19
1.5.2 Recoil spectrum	21
1.6 Thesis Outline	28
2 Liquid Xenon Dark Matter Experiments	30
2.1 Liquid Xenon Microphysics	30
2.1.1 Combined Energy Scale	30
2.1.2 The NEST Model	30

2.2	The LUX and LZ experiments . . . . .	30
2.2.1	Electric Field Model . . . . .	32
2.2.2	Efficiency Corrections . . . . .	32
2.2.3	Electron Trains in LUX Run04 . . . . .	32
3	Building, Optimizing, and Maintaining a Xenon Cold-Trap Sampling System . . . . .	33
3.1	Technical Overview . . . . .	33
3.1.1	System Construction . . . . .	34
3.1.2	Operational Outline . . . . .	36
3.2	Idealized Cold Trap Response . . . . .	38
3.2.1	Vacuum Impedances . . . . .	39
3.2.2	Setting System Impedance . . . . .	42
3.2.3	Generalized Cold Trap System Response . . . . .	43
3.3	Actual Behavior of a Cold Trap System . . . . .	48
3.3.1	Cold Trap Geometry . . . . .	49
3.3.2	Formation of Xenon Ice . . . . .	52
3.3.3	Flow Rate Dependance . . . . .	58
3.3.4	Impedance Dependence . . . . .	61
3.3.5	Post Flow Behavior . . . . .	69
3.3.6	Diffusion and Entrainment . . . . .	73
3.3.7	Model Overview . . . . .	77
3.4	Analysis Scheme . . . . .	78
3.5	System Parameters and Optimization . . . . .	84
3.5.1	RGA Parameters . . . . .	84
3.5.2	Impedance and Flow Rate Settings . . . . .	87
3.6	Preparation of Calibration Xenon . . . . .	92
3.7	Sensitivity Demonstration at SLAC . . . . .	95
3.7.1	Blank Runs . . . . .	96
3.7.2	Mixing of ppQ Level Samples . . . . .	97
3.7.3	Measurements of ppQ Level Samples . . . . .	101
4	LUX Post-Run 04 Calibration Campaign . . . . .	103
4.1	Data Selection . . . . .	106
4.1.1	Single-Scatter Cut . . . . .	107
4.1.2	Radial Selection Cut . . . . .	110
4.2	Argon-37 Non-Gaussianities . . . . .	110
4.3	Signal Corrections fo Post-Run04 Data . . . . .	113
4.3.1	S2 Efficiency Correction from $^{37}\text{Ar}$ . . . . .	113
4.3.2	S1 corrections from Xenon-131m + Krypton-83m Doke Plot . . . . .	119
4.3.3	Applied Corrections . . . . .	123
4.4	Model of the Pathological S2 Tails . . . . .	128

5	Detector Response to $^{14}\text{C}$ Beta Decay	136
5.1	The Theoretical $^{14}\text{C}$ Beta-Spectrum . . . . .	137
5.1.1	The Allowed Spectrum . . . . .	139
5.1.2	The Fermi Function . . . . .	139
5.1.3	The Shape Factor . . . . .	141
5.2	Preliminary Measurement of Light and Charge Yields . . . . .	145
5.2.1	Accounting for Gaussian Smearing of Continuous Beta Spectra . . .	145
5.2.2	Accounting for Non-Gaussian Smearing . . . . .	148
5.3	Measurement of Recombination Fluctuations from $^{14}\text{C}$ . . . . .	149
5.4	Yields and Recombination from Updated NEST Model . . . . .	149
5.5	Measurement of the Shape of the $^{14}\text{C}$ Beta-Spectrum . . . . .	149
A	Alternate Doke-Plot Corrections	150
A.1	No $^{37}\text{Ar}$ . . . . .	150
A.2	Three Point Doke-Plot . . . . .	150
B	Alternate Tail Model	151
B.1	Flat . . . . .	151
B.2	Poisson . . . . .	151
	Bibliography	152

## Chapter 1: Cosmology Overview

### 1.1 Standard Model of Cosmology

The standard model (SM) ties together observations and theories of particle physics into a coherent and predictive picture that is well verified by experiment. In the same way, the standard model of cosmology ( $\Lambda$ -CDM) combines the observations of astronomers and cosmologists in the context of general relativity. Although the standard model paints a comprehensive picture of particles that have been observed, it accounts for only 4.9%[3] of the mass-energy content of the  $\Lambda$ -CDM model.

The  $\Lambda$ -CDM model is built on the foundation of the Robertson-Walker metric:

$$ds^2 = -c^2 dt^2 + a(t)^2 [dr^2 + S_\kappa(r)d\Omega^2] \quad (1.1)$$

$$S_\kappa(r) = \begin{cases} R_0 \sinh(r/R_0) & \text{for } \kappa = 1 \\ r & \text{for } \kappa = 0 \\ R_0 \sin(r/R_0) & \text{for } \kappa = -1 \end{cases} \quad (1.2)$$

This metric assumes an isotropic and homogenous universe, but allows for both time dependent expansion and uniform curvature. The unitless “scale factor”,  $a(t)$ , describes the expansion and contraction of the spatial part of the metric. The curvature of space is characterized by a radius of curvature  $R_0$  and the parameter  $\kappa$ , which is 0 if the universe is flat

and otherwise indicates the sign of the curvature.

The time-dependence in the scale factor can now be described to first and second order. The Friedmann equation is a solution to Einstein's field equations that relates the rate of change in the scale factor to the energy density of the universe,  $\varepsilon$ :

$$H^2 \equiv \left( \frac{\dot{a}}{a} \right)^2 = \frac{8\pi G}{3c^2} \varepsilon - \frac{\kappa c^2}{R_0^2 a^2}, \quad (1.3)$$

where  $G$  is the gravitational constant. Equation 1.3 also introduces the Hubble constant,  $H$ , which describes the expansion rate of the scale factor. The second order equation is obtained through an application of the first law of thermodynamics for an adiabatically expanding universe. This gives the fluid equation, which connects the change in energy density to pressure:

$$\dot{\varepsilon} + 3 \frac{\dot{a}}{a} (\varepsilon + P) = 0 \quad (1.4)$$

By combining equations 1.3 and 1.4, the acceleration equation is found:

$$\frac{\ddot{a}}{a} = -\frac{4\pi G}{3c^2} (\varepsilon + 3P). \quad (1.5)$$

In an empty universe where  $\varepsilon$  is zero, the time evolution of the scale factor is trivial. The curvature can be either flat or negative, but a positive curvature would lead to a non-physical result in equation 1.3. In a flat, empty universe the scale factor would be static, and in a negatively curved universe, the scale factor would increase at a constant rate for all time. To describe the time-evolution of the scale factor in a universe where  $\varepsilon \neq 0$ , there is one further puzzle piece required. A universe can contain multiple component energy densities which will each contribute a unique pressure. The relation between the total energy density

and pressure is given by the equation of state:

$$P = \sum_w w \epsilon_w, \quad (1.6)$$

where  $w$  is a parameter specific to each component.

The total energy density is equal to the sum of the component densities,  $\epsilon_w$ . These are often normalized to the critical density,  $\epsilon_c = \frac{3c^2}{8\pi G} H(t)^2$  and expressed as density parameters,  $\Omega_w = \epsilon_w / \epsilon_c$ . The components of interest in this universe are radiation (which includes relativistic matter), non-relativistic matter, and a contribution from the cosmological constant,  $\Lambda$  (also referred to as dark energy), for which  $w = 1/3, 0, -1$  respectively. Radiation and matter both act to slow down the expansion rate of the universe, while  $\Lambda$  acts to accelerate it. This can be seen more clearly by examining the scale factor in the case of a universe with a single component energy density. The time dependences of the scale factor for single component universes are shown in Table 1.1.

Single Energy Component	$a(t)$
Negative Curvature	$t/t_0$
Matter	$(\frac{t}{t_0})^{2/3}$
Radiation	$(\frac{t}{t_0})^{1/2}$
$\Lambda$	$e^{H_0(t-t_0)}$

Table 1.1: Here is shown the time dependence of the scale factor,  $a$ , in various single energy component universes.

Matter, radiation, and  $\Lambda$  themselves have different dependences on  $a(t)$ . Matter density is related to the number density of particles, so as  $a(t)$  increases,  $\epsilon_{matter}$  will decrease like  $1/a(t)^3$ . In addition to its dependence upon number density,  $\epsilon_{radiation}$  also has a dependence upon the frequency of the radiation. Since an increasing  $a(t)$  stretches the radiation's wavelength, thereby decreasing its frequency,  $\epsilon_{radiation}$  will gain an additional factor of  $1/a(t)$  in its time dependence, so  $\epsilon_{radiation}$  will decrease proportional to  $1/a(t)^4$ [56].

The most widely accepted and best supported model for the current universe has no curvature, is old enough that the radiation component has become negligible, and contains a comparable density of matter and  $\Lambda$ . This model is referred to as the  $\Lambda$ -CDM model.

## 1.2 The Cosmic Microwave Background

The various parameters for the  $\Lambda$ -CDM model are best constrained by measurements of the cosmic microwave background by the Planck experiment, which constrains  $\Omega_{matter}$  to  $0.3089 \pm 0.0062$  and  $\Omega_\Lambda$  to  $0.6911 \pm 0.0062$ [3]. The Planck experiment, along with its predecessors, aimed to create a detailed map of the cosmic microwave background. This background is a snapshot of the universe from only 350,000 years after the big bang.[56] Before that time, the universe was hot enough that electrons could not bind to protons to form atoms, and the scattering rate of photons off of this plasma was high enough for them to thermalize into a blackbody spectrum. Once the scattering rate of high energy photons dropped below the expansion rate of the universe, electrons and protons began forming atoms, which in turn lowered the scattering rate even more. This caused the blackbody photons to rapidly become decoupled from the matter, thus preserving their blackbody spectrum. These photons are what today form the cosmic microwave background (CMB).

Due to random fluctuations, there were anisotropies in the primordial plasma, which tended to fall toward areas with higher densities. This caused the over-densities to become amplified until eventually the increased radiation pressure would overtake the force of gravity, causing the plasma to rebound and expand until the now falling pressure was overtaken the gravitational pull of the over-density. This process led to a “ringing” in the primordial plasma, which is referred to as baryon acoustic oscillations (BAO). BAO began at the end of the inflationary period and ended after the epoch of recombination, when photons decoupled from protons and electrons.

BAO can be seen today as ripples in the CMB. These ripples can be most clearly seen in the angular correlation power spectrum of the CMB shown in Figure 1.1. The highest peak at  $l \approx 200$ , corresponds to about  $1^\circ$ , the angular scale at which the plasma had time to fall into its first compression before photon-decoupling. The second peak corresponds to the scale at which plasma had time to compress and rebound to its first rarefaction. The higher- $l$  peaks show this processes repeating itself, with odd numbered peaks corresponding to compressions and even numbered peaks corresponding to rarefactions.

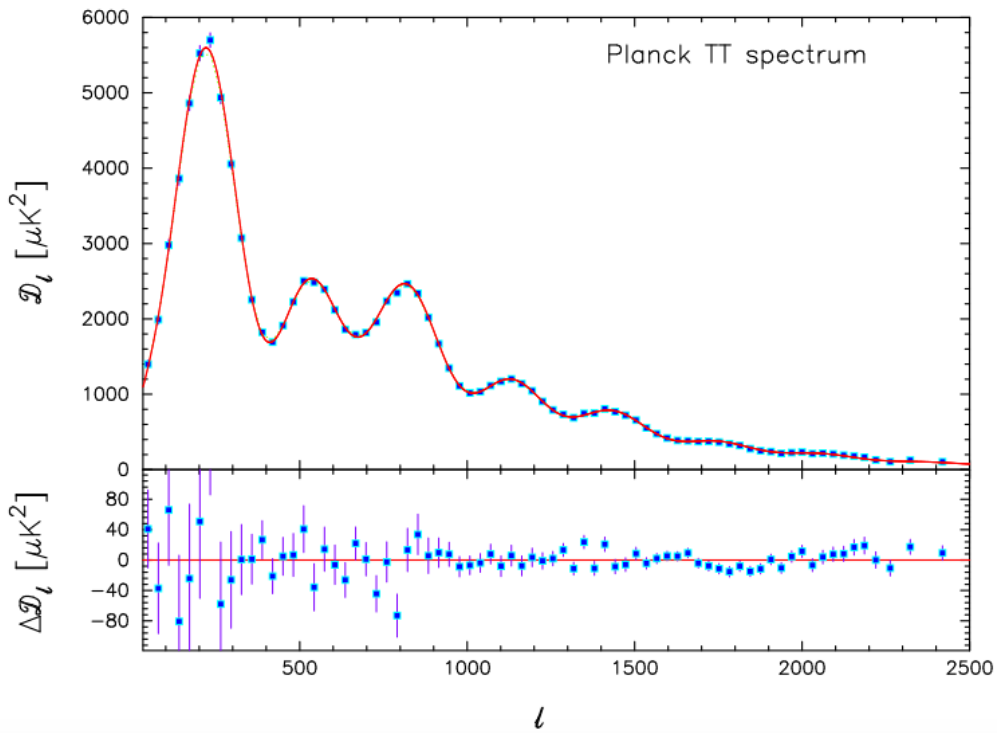


Figure 1.1: Angular correlation power spectrum of the CMB as measured by the Planck experiment. The red line shows the best fit spectrum assuming the  $\Lambda$ -CDM model. [3]

### 1.3 Dark Matter

There is one piece of the  $\Lambda$ -CDM puzzle that is conspicuous in its absence from the description so far. Cold Dark Matter (“CDM” in “ $\Lambda$ -CDM”) is one of the key elements

of the model. Without a driving force external to the photon-baryon plasma, the baryon acoustic oscillations would decay exponentially. The prominence of the third peak relative to the first and second points to the need for an additional form of matter. This matter would be out of equilibrium with the plasma, and so would collapse into the primordial over-densities, but not experience a restorative pressure. As the baryons oscillate, this “dark matter” would continue to accumulate, strengthening the gravitational well. This matter would necessarily couple strongly to neither itself, nor the photons or baryons in the plasma.

### 1.3.1 Galaxy Clusters

The evidence for dark matter from the CMB is relatively recent. Astronomers have been chasing the missing matter problem for almost a century. The first conclusive evidence for what is now known as dark matter came from Fritz Zwicky’s observations of the velocity distribution of galaxies in the Coma Cluster in 1933[67], although calculations by Jan Oort of stellar velocities in the Sombrero galaxy hinted that something was amiss a year earlier in 1932[52]. Assuming that the galactic velocities in the Coma cluster are in a stationary state, the virial theorem can be applied:

$$\bar{V} = -2\bar{K}, \quad (1.7)$$

where  $\bar{V}$  is the average total potential energy of the system, and  $\bar{K}$  is the average total kinetic energy of the system. Assuming a spherically symmetric system governed by Newtonian gravity, Zwicky then made the following approximations for his calculations:

$$V \approx \frac{-3GM}{5R} \quad (1.8)$$

$$K \approx \frac{1}{2} M \bar{v}^2, \quad (1.9)$$

where  $M$  is the total mass of the cluster, and  $\bar{v}$  is the velocity of galaxies in the cluster, averaged over time and mass. Using observations of the doppler shift of the light coming from galaxies within the cluster, Zwicky was able to measure the component of the velocities along the line of sight. He then made the assumption that the velocities are isotropic in order to extrapolate to the overall distribution,  $\bar{v} = \bar{v}_{LS}$ .

Using this method, Zwicky placed a conservative limit of  $M > 4.5 \cdot 10^{13} \odot$  on the mass of the Coma cluster. Comparing this result to the amount of light coming from the cluster, he found that the mass-to-light ratio was more than 100 times larger than typical values for local stellar systems. This was the first indication that a large percentage of matter in the universe is not luminous[67].

### 1.3.2 Galactic Rotation Curves

Continuing from the early measurements of the spiral galaxies by Jan Oort, it was further observed that the other galaxy types also display strong evidence of containing dark matter[57]. A spiral galaxy is well approximated by a flat disk. This makes it possible to measure its galactic rotation curve, or the orbital velocity as a function of radius. Measurements of galactic rotation curves provide some of the most clear and compelling evidence for both the existence and behavior of dark matter on galactic scales.

Measurement's of the luminosity of galaxies show that the density of visible matter tends to decrease exponentially with radius from the galactic center:

$$I(R) = I_0 e^{-R/R_s}, \quad (1.10)$$

where  $R$  is the radius from the galactic center, and  $R_S$  is the a length scale specific to each galaxy. For the Milky Way  $R_S$  is about 4 kpc[56]. This exponential drop would lead rotation curves proportional to  $1/\sqrt{R}$ . In contradiction to this, spectroscopic measurements of stars near the galactic center and the H $\alpha$  line outside of the optical radius, show that the rotation curves of spiral galaxies tend to become flat at large radii[55, 57]. Beginning with Vera Rubin in 1980 [55] and continuing with Massimo Persic and Paolo Salucci [57] among others, researchers went on to characterize the rotational velocities of spiral galaxies by a “universal rotation curve” (URC).

The URC has two components, one from the luminous, exponentially decreasing disk and the other from a “dark halo” which surrounds the galaxy. This dark halo can be thought of as a gas which permeates and surrounds the disk. As a function of  $R/R_{opt}$ , the mass and velocity contributions from this component are:

$$V_d^2 = V^2(R_{opt})(1 - \beta)(1 + a^2) \frac{x^2}{x^2 + a^2}, \quad (1.11)$$

$$M_h(x) = G^{-1}V^2(1)R_{opt}(1 - \beta)(1 + a^2) \frac{x^3}{x^2 + a^2}. \quad (1.12)$$

Both  $\beta$ , the fraction of disk mass inside of the optical radius, and  $a$ , the radius of the halo core are completely determined by the luminosity in this model. The URC fits the observed data very well (on average fitting errors are within 1%).

More recently, models based on n-body simulations of cold dark matter have become more popular. The most well known of these is the Navarro-Frenk-White (NFW) model. These models produce good fits to high-luminosity galaxies such as the Milky Way, but tend to produce cusps at the galactic center and have trouble replicating the flat cores observed in dwarf galaxies. It is possible that this tension could be resolved by gravitational fluctuations

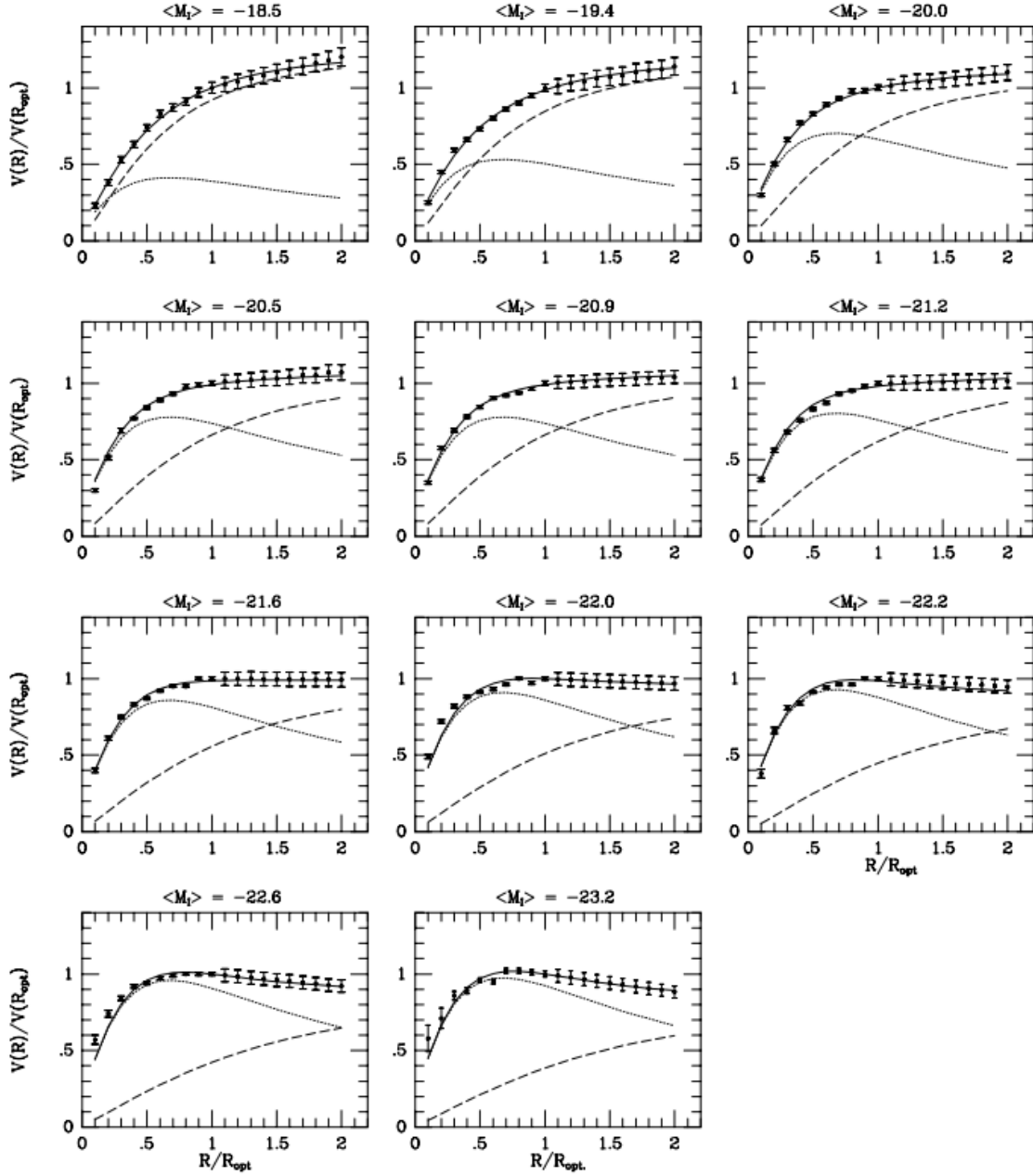


Figure 1.2: URC (solid lines) fit to average rotation curves surveyed spiral galaxies. The subfigures show bins in luminosity each of which contain about 50 individual rotation curves. Also shown are the contributions from the luminous disk (dotted line) and dark halo (dashed line)[57].

or by substructure within the halo at the center of these dwarf galaxies, but the “Cusp-Core” problem remains an active area of study[51, 64].

### 1.3.3 Modified Newtonian Dynamics

The agreement between observation of galactic rotation curves and cluster dynamics is quite remarkable, however there is an alternate hypothesis to dark matter that fits the data equally well in many of these cases. Modified Newtonian Dynamics (MOND) postulates that the force of gravity as described by Newton and Einstein is incomplete. In 1983, Milgrom showed that an interpolating function,  $\mu$ , could be added to Newton’s second law to describe the dynamics of galaxies and clusters without the need for dark matter.

$$m_g \mu(a/a_0) \vec{a} = \vec{F} \quad (1.13)$$

This interpolating function would be  $\approx 1$  at large accelerations,  $a \gg a_0$ , reproducing the classical equation of motion, but would approach  $\mu x = x$  when  $a \ll a_0$ , where  $a_0 = 2 \times 10^{-8} \text{ cm} \cdot \text{s}^{-2}$  is a fundamental constant[11, 49].

Following their initial paper in 1983, M. Milgrom and J. Bekenstein reformulated MOND as a classical, lagrangian based field theory, known as AQUAL. In 2004 Bekenstein again reformulated MOND in the context of general relativity. This new tensor-vector-scalar covariant theory is referred to as TeVeS[11]. Both of these theories can produce good fits to galactic rotation data in many cases, but among other problems, neither can fully describe cluster dynamics without the addition of some dark matter[11, 19].

### 1.3.4 Gravitational Lensing

One of the single most compelling pieces of evidence for dark matter, especially in relation to MOND theories, comes from gravitational lensing data of galactic cluster 1E

0657-56, more commonly known as the bullet cluster. This cluster consists of two sub-clusters that recently collided and passed through each other. One of these subclusters displays a distinct bow shock that enabled researchers to make a precise measurement of its Mach number, thereby also measuring its velocity. The measured Mach number,  $3.2^{+0.8}_{-0.6}$  corresponds to a velocity of  $4500^{+1100}_{-800} \text{ km/s}$ [45].

During the collision, the gas from the two subclusters would be expected to experience much stronger drag than the stellar matter. This expectation was confirmed by x-ray imaging data from Chandra, which showed that the gas was lagging behind the stars. Further comparison to a mass mapping using gravitational lensing reveals additional matter populations centered near the stellar matter, which are taken to be the dark matter halos of the two subclusters. Fitting a King mass profile ( $\rho = \rho_0(1 + r^2/r_c^2)^{-3/2}$ ) to the lensing data, Markevitch et. al. calculated the density of the dark matter, and limited the self interaction cross section to  $\sigma/m < 1 \text{ cm}^2 \text{ g}^{-1}$ [45].

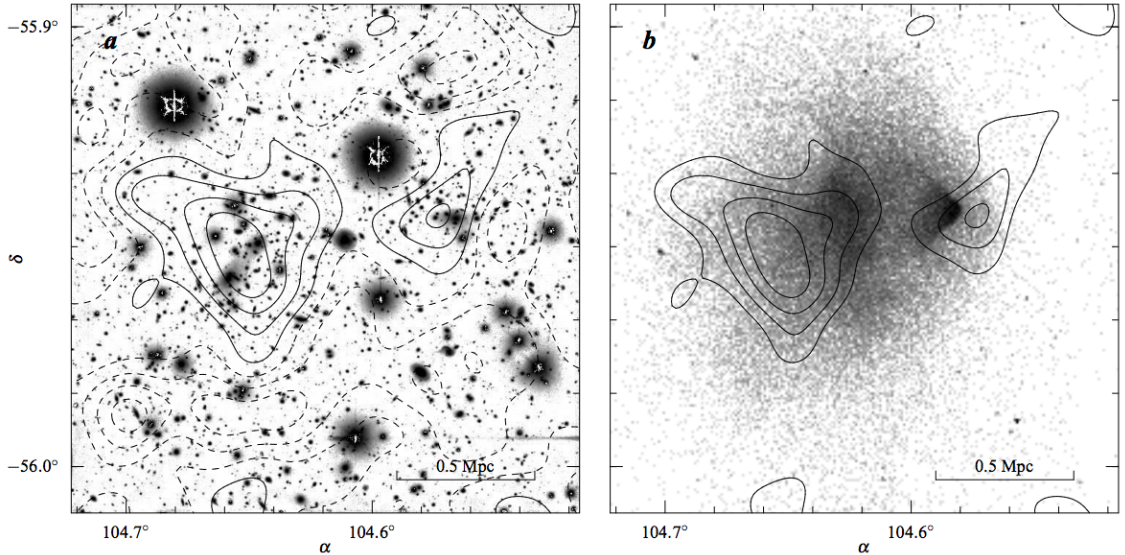


Figure 1.3: Comparison of the location of dark matter, stellar matter, and x-ray gas in the bullet cluster. The mass density from lensing data, indicated by the solid black lines is imposed over optical (left) and x-ray (right) maps[45].

## 1.4 Dark Matter Candidates

### 1.4.1 Baryonic Dark Matter

Now that the existence of cold dark matter has been well motivated, the next step is to investigate what it might be. A reasonable starting point is to look at types of matter that are already known to exist, and ask whether they could exist in high enough abundances to explain the observations of galaxy and cluster dynamics as well as angular correlations in the CMB.

Within the standard model, the first place to look for dark matter is baryonic matter. It is possible, for instance, that the dark halo is, at least partially, composed of large structures of baryonic material such as brown dwarfs or planets. These massive compact halo objects (MaCHO's) should be observable through gravitational lensing. As a MaCHO passes between an observer on Earth and a background star, the light from that galaxy will be temporarily distorted through gravitational lensing. The EROS-2 experiment conducted a survey of the large Magellanic clouds and found insufficient lensing events to allow MaCHO's as a primary constituent of the Milky Way's dark halo[61].

A more general constraint on baryonic dark matter comes from measurements of big bang nucleosynthesis (BBN). BBN refers to the epoch at which the temperature of the universe dropped below the binding energy of deuterium (2.22 MeV). This happened when the universe was about 5 minutes old. During this epoch, the primordial abundances of light nuclei are set as the protons and neutrons are allowed to combine into energetically favored states. The ratios of these abundances are highly dependent on  $\eta$ , the baryon-photon ratio, so the measurement of them, combined with constraints on the photon density from CMB measurements would give a precise value for the baryon density[56]. Current measurements of D/H place the baryon density at  $\Omega_b h^2 = 0.02202 \pm 0.00046$  [21].

This result is within  $1\sigma$  of the measurement from the Planck experiment, and taking the reduced Hubble constant to be  $h = 0.678$ , it indicates that baryons make up only 4.8% of the energy-density of the universe[3].

### 1.4.2 Neutrinos

The remaining candidate for standard model dark matter is the neutrino. Before the CMB decoupled, neutrinos went through a similar process which left the universe filled with neutrinos that had been in thermal equilibrium with the extremely hot and dense early universe. From the annihilation cross-section, the number density of the cosmic neutrino background (CNB) can be calculated to be 3/11 that of CMB photons[56],

$$n_\nu = 3.36 \times 10^8 \text{ m}^{-3}. \quad (1.14)$$

In order for the CNB to fit the mass density requirement for dark matter, the mass of neutrinos would have to be about 4 eV.[56] Current constraints from Planck show that the combined mass of neutrinos is  $< 0.23 \text{ eV}$ [3], so neutrinos are not heavy enough to explain the majority of observed dark matter.

### 1.4.3 Axions

Currently, the two most popular CDM candidates are Axions and WIMPs. Axions are particularly interesting because they were first theorized as part of a solution to the strong CP problem, and so could simultaneously solve two unsolved problems in physics. Charge-parity (CP) is only conserved by QCD if the vacuum angle,  $\theta$ , is 0. However,  $\theta$  should be able to take any value, so CP is not predicted to be conserved. Experimental measurements of the neutron electric dipole moment (nEDM) show that CP is, in fact, a good symmetry of QCD. The current limit on nEDM is about  $2 \times 10^{-26} \text{ e} \cdot \text{cm}$ , which in turn limits  $\theta$  to

$\leq 10^{-9}$ [10, 25]. This unexpectedly small value of  $\theta$  points to a tension within QCD. To relieve this tension, R. Peccei and H. Quinn proposed a new spontaneously broken global symmetry,  $U_{PQ}(1)$ , and showed that if the Higgs potential for at least one quark is invariant under  $U_{PQ}(1)$ , then  $\theta$  is guaranteed to relax to 0. The pseudo-Nambu-Goldstone boson that is associated with the spontaneous breaking of  $U_{PQ}(1)$  is known as the axion [25, 53].

The axion as a candidate for CDM is compelling in that it interacts only very weakly with standard model particles. Axions are expected to have mass, but be light enough that those produced thermally in the big bang would be too hot to fill the role of CDM. However, populations of axions can be formed non-relativistically in the early universe through vacuum realignment and topological effects in string theory. Axion dark matter created through realignment would be expected to have a mass  $m_a > 6 \mu eV$ , assuming the initial value of  $\theta$  was of order unity. If the initial value of  $\theta$  was much smaller than 1, the axion mass could be less than  $6 \mu eV$ [25].

Axion searches focus primarily on the tree-level axion-photon coupling, which has the Lagrangian term  $\mathcal{L}_{a\gamma\gamma} = g_{a\gamma\gamma} \mathbf{E} \cdot \mathbf{B}$ . In the core of a star, the conversion of photons to axions can compete with the production of photons and stream energy away from the core. This would reduce the pressure and causing the star to compress and heat up, and in so doing, shorten the life of the star. Observations of horizontal branch stars limit the coupling constant for this process to  $g_{a\gamma\gamma} < 10^{-10} GeV^{-1}$ , and excludes axion mass in the range  $10^{-3} eV < m_a < 2 eV$  [25, 30].

In the laboratory, the conversion of axions to photons, and vice versa can be induced in a cavity containing a strong magnetic field. The CAST experiment at CERN used such a cavity to search for axions streaming from the sun. By adding a precisely tuned pressure of helium gas to the cavity, they maximized their sensitivity, and placed a limit of  $g_{a\gamma\gamma} < 2.2 \times 10^{-10} GeV^{-1}$  for axions with mass  $m_a < 0.4 eV$ [25, 30].

The previously cited limits are on axions that were formed in the cores of stars. These

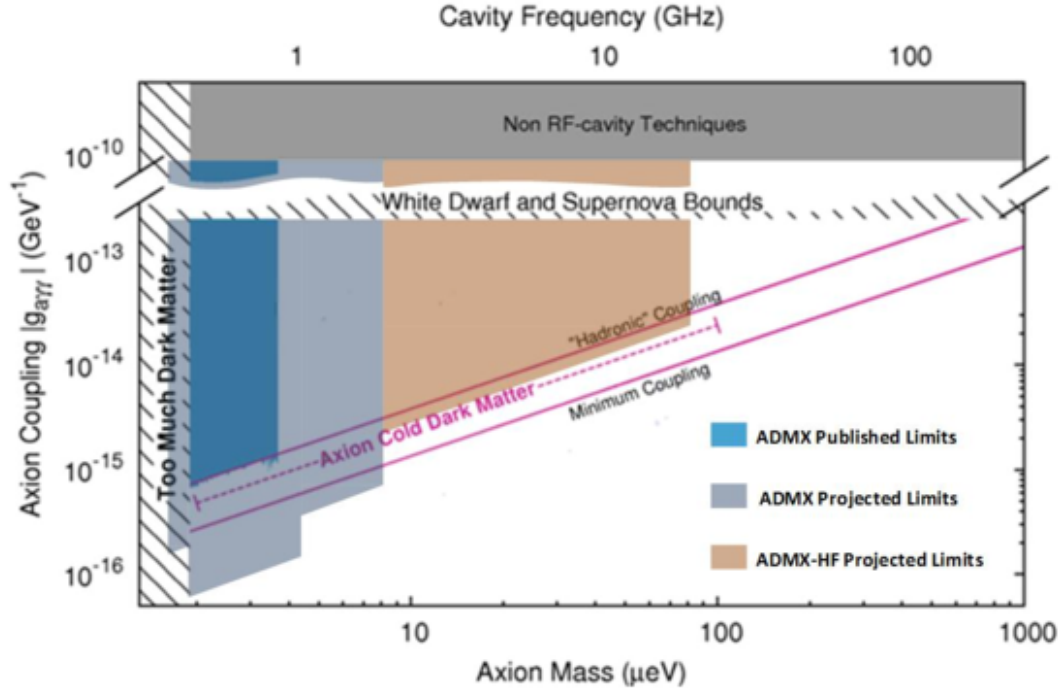


Figure 1.4: Long term projected limits of the ADMX and ADMX-HF experiments. [60]

axions, if they existed, would not be able to fill the CDM role. Currently, the only experiment that would be sensitive to dark matter axions is the Axion Dark Matter Experiment (ADMX). This experiment aims to convert axions from the local dark halo into photons using a microwave resonant cavity permeated with a strong magnetic field. In this scenario, a DM axion would interact with a virtual photon from the magnetic field to convert into a real RF photon which can be detected. ADMX and it's sister experiment ADMX-HF are looking for axion dark matter in the mass range  $2\mu eV$  to  $100\mu eV$  and are expected to be able to probe most of the allowable axion CDM phase space[25, 60].

#### 1.4.4 WIMPs

The other leading candidate for CDM is what is referred to as the Weakly Interacting Massive Particle, or WIMP. “WIMP” is a somewhat generic term for a massive particle that couples to standard model particles only through the weak nuclear force. This generic WIMP particle is usually denoted as  $\chi$ . Many extensions to the standard model, in particular supersymmetric models, include at least one flavor of WIMP. In the very early universe WIMPs will be in equilibrium with the primordial plasma. Just as with CMB photons and CNB neutrinos, once the temperature drops and the universe expands the number and temperature of WIMPs will fall out of equilibrium and the particles remaining will persist as a cosmic relic[28, 35].

When the temperature of the universe is higher than the WIMP mass,  $m_\chi$  (roughly 10 GeV to 1 TeV) both the WIMP number density,  $n_\chi$ , and temperature will be in thermal equilibrium. Once the temperature drops below the WIMP mass, the number density will fall out of equilibrium and will pick up a Boltzmann suppression factor of  $e^{-m_\chi/T}$ . Once the scattering rate of cosmic WIMPs drops below expansion rate of the universe,  $\chi$  particles will no longer be able to find each other to annihilate, and  $n_\chi$  will freeze out, becoming the relic density that exists today[28].

This relic density is determined by the mass of  $\chi$ , as well as its self-annihilation cross section,  $\sigma_A$ , but is much more strongly dependent upon the cross section.[28, 35] If  $\sigma_A$  is on the scale of the weak force, the density parameter for relic WIMPs will be on the order of what is required for  $\Omega_{CDM}$ . This is considered one of the most compelling reasons to consider WIMPs as CDM candidates, and has been referred to as the “WIMP miracle”[13, 28, 35].

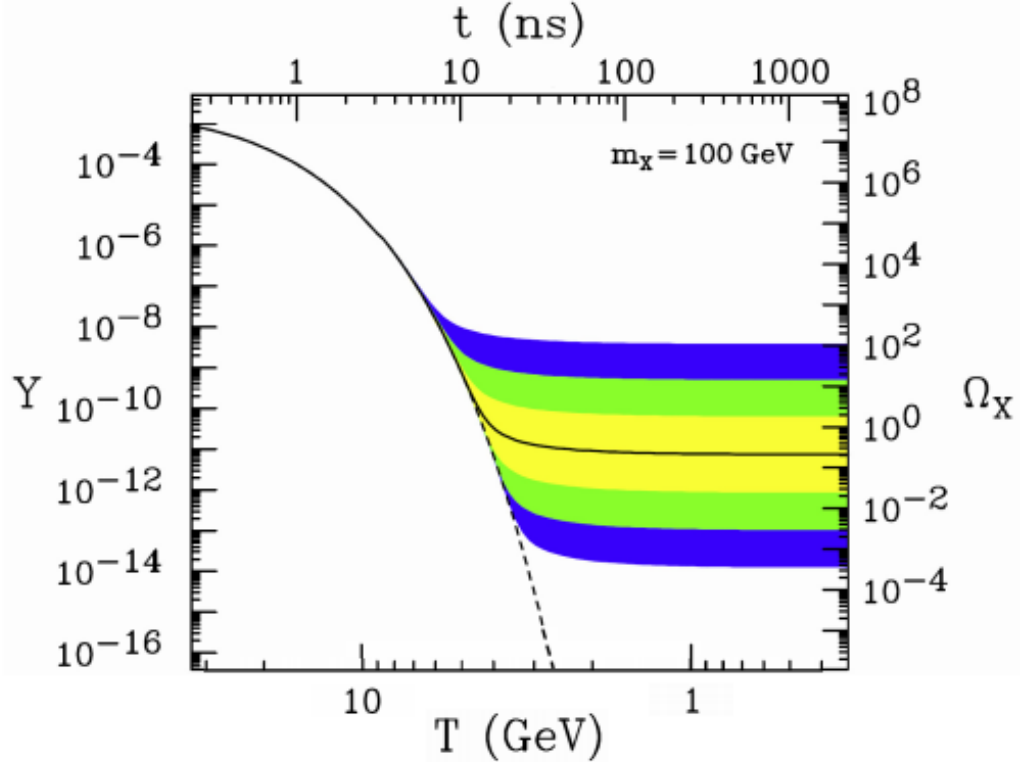


Figure 1.5: WIMP number density in the early universe. The solid line corresponds to the cross section required to account for 100% of CDM. The colored bands indicate variations by factors of 10, 100 and 1,000[28].

The creation of the relic density is described by the Boltzmann equation:

$$\frac{dn_\chi}{dt} = -3Hn_\chi - \langle \sigma_A v \rangle (n_\chi^2 - n_{eq}^2). \quad (1.15)$$

In equation 1.15, the first term on the right hand side is from the expansion of the universe, the  $n_\chi^2$  term is from self annihilation, and the  $n_{eq}^2$  is the creation of WIMPs from standard model particles.[28, 35] The value of  $n_{eq}$  is what the number density of WIMPs would be in thermal equilibrium in a static universe. Equation 1.15 has no closed form solution and is solved numerically. There is, however, some insight that can be drawn from some rough analysis[13, 28].

The equilibrium number density for non-relativistic dark matter is given by a simple Boltzmann distribution,  $n_\chi = g_\chi \frac{m_\chi T}{2\pi} e^{-m_\chi/T}$ . [13] Freeze out will occur when the expansion rate of the universe,  $H$ , exceeds the annihilation rate of WIMPs,  $\Gamma = n_\chi \langle \sigma_A v \rangle$ . In rough terms, the freeze out temperature can be defined as the temperature at which  $H$  and  $\Gamma$  are equal.[13, 28] In the early universe, it is appropriate to make the approximation  $H \approx 1.66g_*^{1/2}T^2$ [35]. In this case the equation  $H = \Gamma$  can be rewritten to give the WIMP density at freezeout:

$$n_{\chi,f} \approx g_\chi \frac{m_\chi T_f}{2\pi} e^{-m_\chi/T_f} \approx \frac{1.66g_*^{1/2}T_f^2}{\langle \sigma_A v \rangle} \quad (1.16)$$

The ratio of  $x_f \equiv m_\chi/T_f$  remains roughly constant between different WIMP models and has a value of about 1/20. After freeze out, the ratio of  $n_\chi$  to entropy density,  $s$ , is constant. In the early universe,  $s \approx 0.4g_*T^3$ . Holding  $(n_\chi/s)$  constant from freeze out to the present day yields the following expression for the current energy density,  $n_{\chi,0}$ :

$$n_{\chi,0} \approx \frac{1.66g_*^{1/2}T_f^2}{\langle \sigma_A v \rangle} \cdot \frac{s_0}{0.4g_*T_f^3} \quad (1.17)$$

Taking the current entropy density to be  $s_0 = 4000 \text{ cm}^{-3}$  yields the following energy density for relic WIMPs:

$$\Omega_\chi h^2 \approx \frac{3 \cdot 10^{-27} \text{ GeV cm}^3}{\langle \sigma_A v \rangle} \quad (1.18)$$

Plugging in a typical weak annihilation cross section of about  $10^{-25} \text{ cm}^3 \text{ s}^{-1}$  for  $\langle \sigma_A v \rangle$  gives  $\Omega_\chi h^2 \approx 0.03 \text{ GeV s}$  which is close enough to the expected value CDM,  $\Omega_{CDM} h^2 = 0.1188 \text{ GeV s}$ [3] to make WIMPs an extremely exciting candidate to explain much, if not all, of the non-baryonic dark matter in the universe[28, 35].

## 1.5 WIMP Direct Detection

The relic density of WIMPs is determined by the cross-section for annihilation into standard model particles, a process which might be observed today by looking for high energy particles coming from high density regions of space such as galactic nuclei. The hypothetical interaction between WIMPs and standard model particles can also be run in two other directions. Production of WIMP dark matter from standard model particles can be searched for using modern particle colliders such as the LHC at CERN, and the scattering of relic dark matter can be probed for using large, low-background detectors. These three methods of detection are referred to as “indirect detection”, “production”, and “direct detection” respectively. Direct detection is of particular interest because it probes the existing relic dark matter background that is postulated by the  $\Lambda$ -CDM model.

### 1.5.1 Cross Section

The first ingredient needed to calculate the expected interaction rate in a given experiment is the scattering cross section. The WIMP-nucleus scattering cross section will have some dependence on the momentum transfer,  $q$ , and can be written[58]:

$$\sigma(q) = \sigma_0 F^2(q), \quad (1.19)$$

where  $\sigma_0$  is the energy independent, 0-momentum limit of the cross section, and  $F(q)$  is an energy dependent form factor. The 0-momentum cross section can be broken into a spin dependent (SD) part and a spin independent (SI) part[39, 58]:

$$\begin{aligned} \sigma_{0,SI} &= \frac{4\mu_A^2}{\pi} [Zf_p + (A-Z)f_n]^2 \\ \sigma_{0,SD} &= \frac{32G_F^2\mu_A^2(J+1)}{\pi J} [a_p\langle S_p \rangle + a_n\langle S_n \rangle]^2 \end{aligned} \quad (1.20)$$

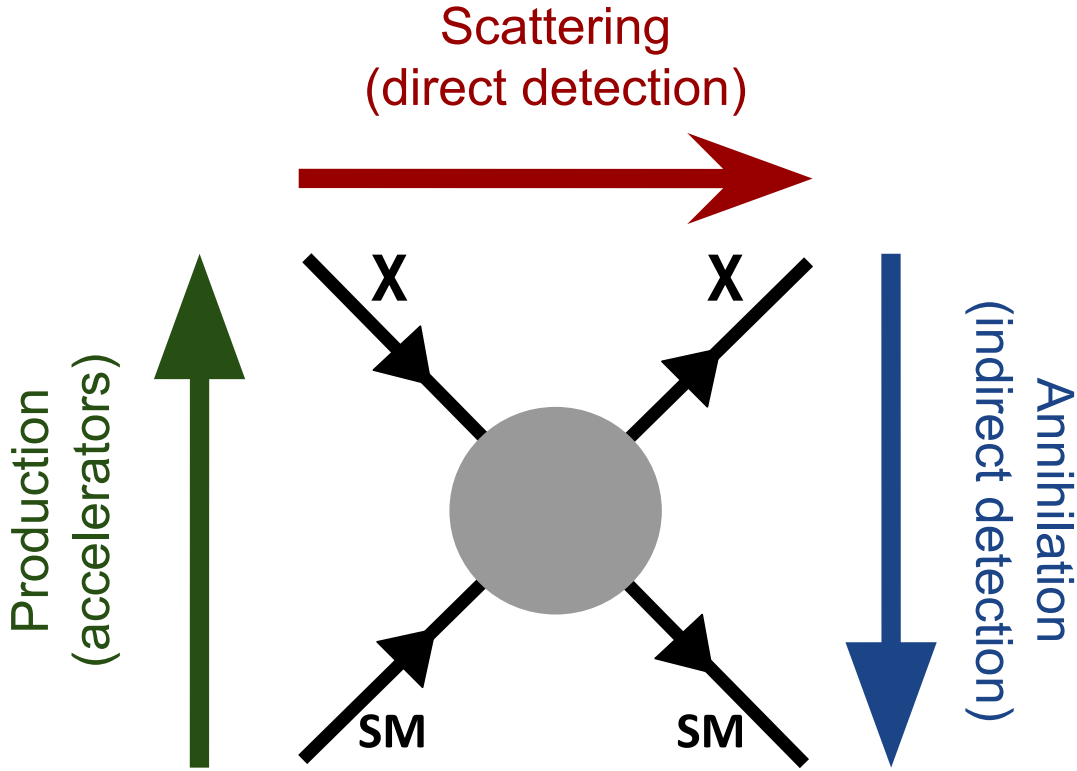


Figure 1.6: Cartoon of the WIMP-standard model interaction. The green, red, and blue arrows indicate in which direction time is being run for production, scattering, and annihilation, respectively.

Here,  $f_{p,n}$  and  $a_{p,n}$  are the SI and SD coupling constants of WIMPs to protons and neutrons,  $\mu_A$  is the reduced mass of the interaction,  $Z$  is the atomic number,  $A$  is the atomic mass,  $J$  is the nuclear spin, and  $\langle S_{p,n} \rangle$  is the average spin of protons or neutrons in the nucleus. It is typically assumed that  $f_p \approx f_n$ , so the SI cross section reduces to:

$$\sigma_{0,SI} = \frac{4\mu_A^2}{\pi} f_n^2 A^2. \quad (1.21)$$

The  $\mu_A^2 A^2$  dependence in equation 1.21 is a result of the non-relativistic nature of the interaction leading the incident WIMP to scatter coherently off of the nucleus as a whole as opposed to the individual nucleons. This is an important result because it indicates a large

benefit to using heavy nuclei as experimental target media. For instance, a detector which uses xenon as its target medium ( $A \approx 131$ ) will be over 10 times more sensitive to a 100 GeV WIMP than an argon based detector ( $A \approx 40$ ) with the same mass of target material.

Another important result is that the SD cross section does not have the same  $\mu_A^2 A^2$  dependence, and in many nuclei the nucleon spins cancel entirely leaving that isotope insensitive to WIMP interactions. In the case of xenon, the only isotopes that have non-zero spin and a non-negligible natural abundance are  $^{131}\text{Xe}$  ( $J=3/2$ ) and  $^{129}\text{Xe}$  ( $J=1/2$ ), which together make up just under half of the natural xenon abundance. Since for xenon has an even number of protons,  $\langle S_p \rangle$  is very close to zero (-0.009 for  $^{131}\text{Xe}$  and 0.028 for  $^{129}\text{Xe}$ ). The neutron part of the SD cross section in  $^{129}\text{Xe}$  and  $^{131}\text{Xe}$  is about 2,000 and 400 times that of a single-neutron, respectively. We can compare this to the SI cross section of xenon, which is  $> 5 \times 10^7$  times larger than the single-nucleon cross section. This suppression of the SD cross section in comparison with the SI cross section has led to much less stringent limits on spin independent interactions than on spin dependent interactions as can be seen in the results from the LUX detector in figure 1.7.

### 1.5.2 Recoil spectrum

The WIMP halo is expected to have only a small amount of bulk rotation; that is it is expected to be more akin to a gravitationally bound ideal gas than an accretion disk. The velocities of WIMPs in such a halo roughly modelled by a Maxwellian distribution[58]:

$$f(\vec{v}_{halo}) = e^{-v_{halo}^2/v_0^2}/k, \quad (1.22)$$

with  $v_0 = 220 \pm 20$  km/s being the local circular velocity around the galactic center and  $k$  being a normalization constant. In the lab frame the observed velocity of an incident WIMP will be  $\vec{v}_i = \vec{v}_E + \vec{v}_{halo}$ . Here,  $\vec{v}_E$  is the velocity of the earth with respect to the galaxy which

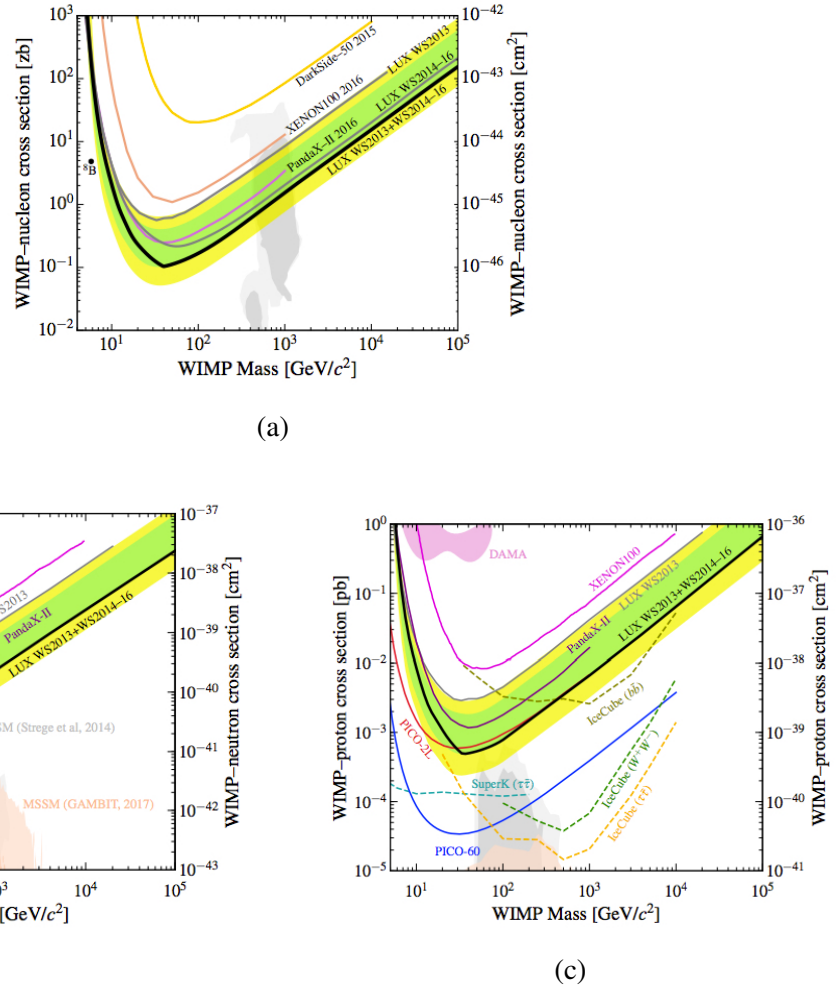


Figure 1.7: Limits on the SI single-nucleon (a), SD single neutron (b), and SD single proton (c) cross sections. These limits were taken from the LUX experiment's full exposure (332 days). The SI limit is roughly 5 orders of magnitude better than the SD neutron limit, which itself is about 2 orders of magnitude better than the SD proton limit. The solid black lines show the experimentally measured limits, and the green and yellow regions show the 1- and 2- $\sigma$  expectations. Figures were taken from [4] and [44].

is the sum of  $\vec{v}_0$ , the sun's peculiar velocity,  $\vec{v}_s$ , and the orbital velocity of the earth around the sun,  $\vec{u}_E(t)$ [47, 58]:

$$\vec{v}_E(t) = \vec{v}_0 + \vec{v}_{sun} + \vec{u}_E(t). \quad (1.23)$$

The contribution to  $\vec{v}_E(t)$  from the velocity of the sun with respect to the galactic center ( $|\vec{v}_0 + \vec{v}_{sun}|$ ) is about 232 km/s, and  $\vec{u}_E(t)$  acts to add a 6% annual modulation. This modulation would presumably introduce a detectable effect in the scattering rate of WIMPs. The DAMA/LIBRA NaI scintillation detector[14] has observed with  $9.3\sigma$  confidence annual modulation in their 2-6 keV, single-scatter event rate. This result, however, is in significant tension with other experimental limits (see for instance figure 1.7c).

We can use this velocity distribution to write the scattering rate as a function incident velocity,  $v_i$ . This will give the total number of WIMP-nucleus scattering events per unit time per gram of material with atomic weight,  $A$ :

$$dR(v_i) = \frac{N_A}{A} n_\chi f(\vec{v}_i - \vec{v}_E) \sigma v_i d^3 \vec{v}_i, \quad (1.24)$$

with  $N_A$  being Avagadro's number and  $n_\chi$  being the local number density of WIMPs.

The velocity of a WIMP in the lab frame is highly non-relativistic. This being the case, collisions between WIMPs and the target nuclei of earth-bound detectors can be well modeled by classical elastic scattering. The recoil energy,  $E_R$ , for elastic scattering of a non-relativistic WIMP of mass  $M_\chi$  off of a nucleus of mass  $M_A$  is given by[58]:

$$E_R = \frac{E_i r}{2} [1 - \cos(\theta)], \quad (1.25)$$

where  $E_i = \frac{1}{2} M_\chi v_i^2$  is the energy of the incident WIMP,  $\theta$  is the recoil angle, and  $r = 4M_\chi M_A / (M_\chi + M_A)^2$  is a kinematic factor.

For a WIMP with a given  $v_i$ , the nuclear recoil energy will be even distributed between

0 and  $E_i r$ . These uniform distributions can then be weighted by  $dR(v_i)$  and then integrated over  $v_i$  to give the total differential scattering rate:

$$\frac{dR}{dE_r} = \int_{E_{min}}^{E_{max}} dR(v_i)/E_i r \quad (1.26)$$

For the limits of integration we could take into account the escape velocity of the galaxy, but setting  $E_{max} = \infty$  yields a good approximation and makes evaluation of the integral simpler. Only WIMPs with incident energy equal to or greater than  $E_R/r$  will contribute to the scattering rate at  $E_R$ , so we will set  $E_{min} = E_R/r$ . Under this approximation, the normalization constant in equation 1.22 becomes  $k = (\pi v_0^2)^{3/2}$ . If we make the further assumption that  $\vec{v}_E = 0$ , we can write:

$$\begin{aligned} dR(v_i) &= \frac{R_0}{2\pi v_0^4} e^{-v_i^2/v_0^2} v_i (4\pi v_i^2 dv_i) \\ &= \frac{2R_0}{v_0^4} e^{-v_i^2/v_0^2} v_i^3 dv_i \end{aligned} \quad (1.27)$$

where,

$$R_0 = \frac{2N_A}{\sqrt{\pi}A} n_\chi \sigma_0 v_0, \quad (1.28)$$

for constant cross section. Equation 1.26 then becomes:

$$\frac{dR}{dE_r} = \frac{R_0}{E_0 r} \frac{2}{v_0^2} \int_{E_R/r}^{\infty} e^{-v_i^2/v_0^2} v_i dv_i. \quad (1.29)$$

If we make a change of variables to energy space, this integral becomes:

$$\frac{dR}{dE_r} = \frac{R_0}{E_0 r} \int_{E_R/r}^{\infty} e^{-E_i/E_0} dE_i, \quad (1.30)$$

which easily evaluates to:

$$\frac{dR}{dE_r} = \frac{R_0}{E_0 r} e^{-E_r/E_0 r} \quad (1.31)$$

Here we see that  $R_0$  will give the total scattering rate.

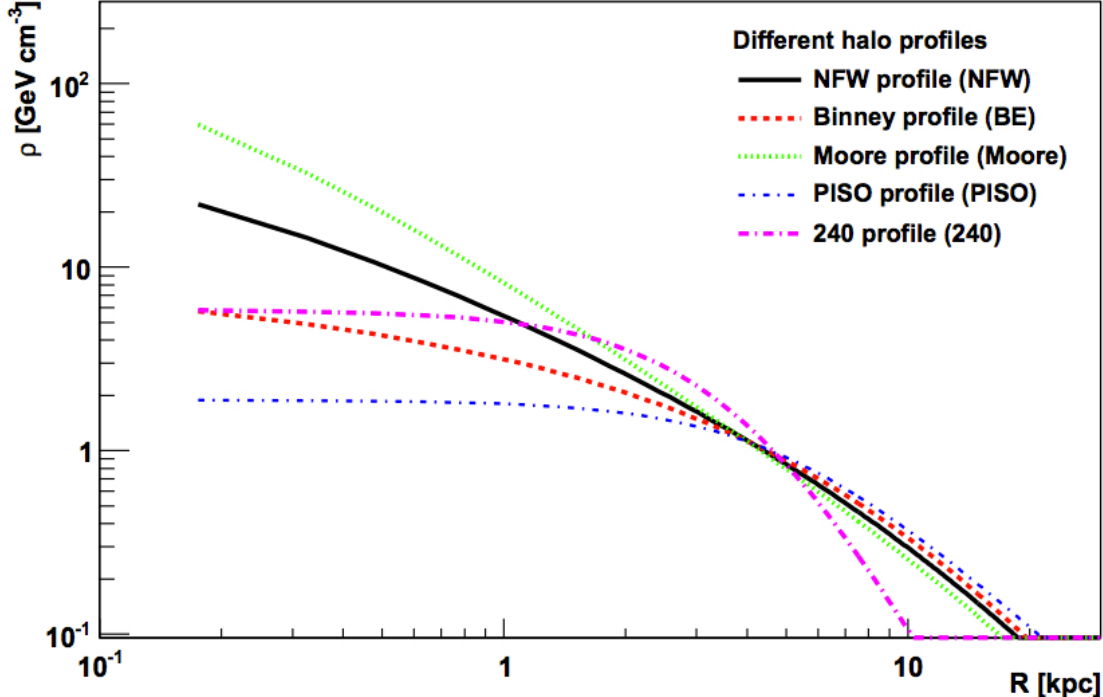


Figure 1.8: Various theoretical halo profiles. The sun is at about 8 kpc. The significant variance of  $\rho_\chi$  for the different models limits the accuracy of scattering rate estimates for direct detection experiments. Figure from [64].

From measurements of the galactic rotation curve, the local dark matter density is expected to be approximately  $0.2\text{-}0.4 \text{ GeV cm}^{-3}$ . This value is highly dependent on theoretical profile model and could be as high as  $0.7 \text{ GeV cm}^{-3}$  given a nonuniform halo density[64]. Here we assume a middling value of  $0.4 \text{ GeV cm}^{-3}$ . If we take  $M_\chi = 100 \text{ GeV}/c^2$ , and  $M_A = 122 \text{ GeV}/c^2$  (xenon atomic mass), we have  $r = 0.99$  and  $E_0 = 27 \text{ keV}$ . In

this case the total scattering rate in counts· day<sup>-1</sup>·kg<sup>-1</sup> will be:

$$R_0 = \frac{2}{\sqrt{\pi}} \frac{(1000 \text{ g/kg}) \times (6.022 \times 10^{23} \text{ atoms/mole})}{131 \text{ g/mole}} \frac{0.4 \text{ GeV/cc}}{100 \text{ GeV}/c^2} \sigma_0 (7.34 \times 10^{-4} c) \\ \approx \left( \frac{131}{A} \right) \left( \frac{\sigma_0}{1 \text{ pb}} \right) (0.4 \text{ counts/kg/day}). \quad (1.32)$$

So for a xenon detector and a WIMP-nucleus cross section of 1 picobarn, there would be about one event every 25 days per kilogram of detector material.

The effect of the finite galactic escape velocity,  $V_{esc} = 540 \text{ km/s}$ , can be approximated by introducing a cutoff to equation 1.31. Very nearly all of the WIMPs with velocity greater than  $V_{esc}$  should have left the halo, so maximum recoil energy will be  $E_{max} = \frac{r}{2} M_\chi v_{esc}^2$ . For xenon detectors:

$$E_{max} = \frac{1}{(1 + M_A/M_\chi)^2} (790 \text{ keV}). \quad (1.33)$$

Detectors which have energy thresholds greater than  $E_{max}$  will be completely insensitive to WIMPs of that mass. In addition to the hard cut off at  $E_{esc}r$ , the exponential nature of equation 1.31 means that detectors will be significantly less sensitive to WIMPs for  $E_0r < E_{threshold}$ . For xenon:

$$E_0r = \frac{1}{(1 + M_A/M_\chi)^2} (131 \text{ keV}). \quad (1.34)$$

This means that a xenon detector with a 20 keV threshold will begin to lose sensitivity for  $M_\chi < 20 \text{ GeV}/c^2$ , and will be completely insensitive to WIMPs with  $M_\chi < 3 \text{ GeV}/c^2$ . This places a large incentive for direct detection experiments to have a very low threshold.

In the derivation of equation 1.31, we assumed a constant scattering cross section. This, however, neglects the nuclear form factor,  $F(q)$ , which was introduced in equation 1.19. This form factor takes into account the nuclear wave-function, which becomes important

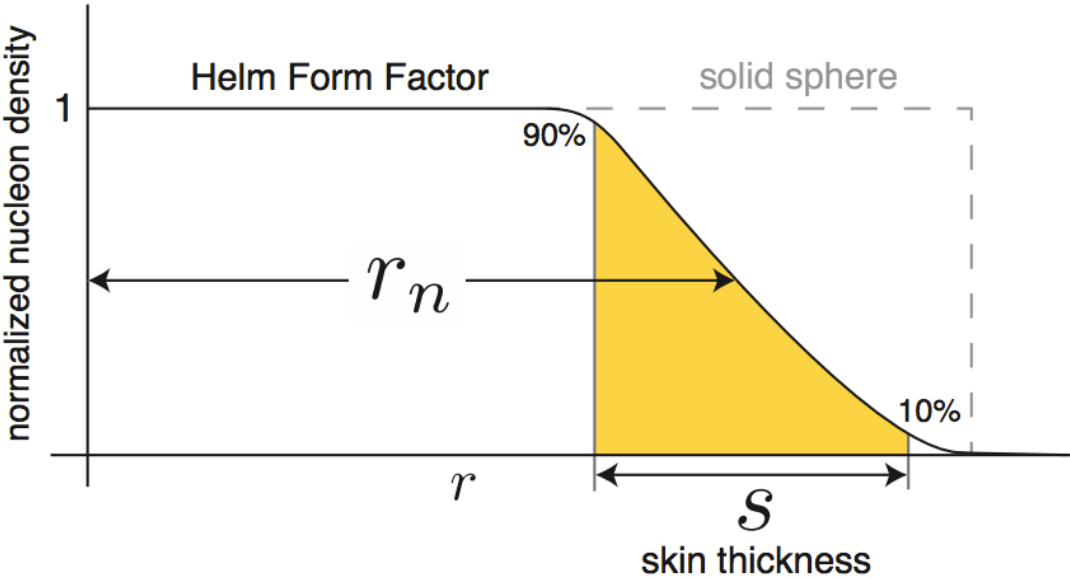


Figure 1.9: Helm approximation of the nucleon density. This approximation has the form of a solid sphere with a Gaussian falloff of thickness,  $S$ . Figure from [27].

at higher momentum transfers where coherent scattering begins to break down. Under the Born approximation and for spherically symmetric nucleon density,  $\rho r$ , the form factor is:

$$F(q) = \frac{4\pi}{q} \int \rho(r) \sin(qr) r dr. \quad (1.35)$$

The most common approximation for the nucleon distribution the Helm approximation-a solid sphere which convolved with gaussian to create a smooth fall off at the edge[34]. Plugging this into equation 1.35 yields:

$$F(q) = \frac{3[\sin(qr_n) - qr_n \cos(qr_n)]}{(qr_n)^3} e^{-(qs)^2/2}, \quad (1.36)$$

where  $r_n$  is the nuclear radius and the skin width,  $s$ , is the width of the Gaussian fall off in the Helm approximation. The skin width is usually taken to be  $s = 0.9$  fm[43], and the nuclear radius can be approximated  $r_n \approx 1.14A^{1/3}$ .

When the de Broglie wavelength,  $h/q$ , becomes comparable to the nuclear radius,  $r_n$ , coherent scattering will break down. This causes a drastic fall in the scattering rate. Xenon, for instance, will lose coherence at about 100 keV, while smaller elements will maintain the benefit of coherent scattering to significantly higher energies. This effect will compete against benefit from the  $A^2$  dependence of  $\sigma_{0,SI}$ . Ultimately the low-momentum benefit of xenon as a target medium, together with self-shielding effects which will be described later, makes xenon the most popular and promising target material for direct detection experiments.

## 1.6 Thesis Outline

In this chapter, we discussed the evidence for particulate cold dark matter in general. We then discussed the motivation and proposed detection techniques for Weakly interacting massive particles (WIMPS). In the next chapter, we will continue to narrow our focus to liquid xenon time projection chambers as WIMP detectors. This will include a discussion of the microphysics behind energy deposits in liquid xenon, as well as the design, construction, and operation of the LUX and LZ dark matter detectors.

In chapter 3 we will discuss a technique for monitoring the purity of liquid xenon. We have improved on an existing technique using novel methods of optimization. We detail the empirical studies that went into this optimization, as well as the theoretical motivation behind them.

Chapter 4 will describe the LUX post-run04 calibration campaign. There are several internal sources novel to the LUX detector which were injected during this timeframe. We will catalog these sources, and present signal corrections derived from them. We will also describe a systematic pathology in the charge signals, as well as our attempt to account for it.

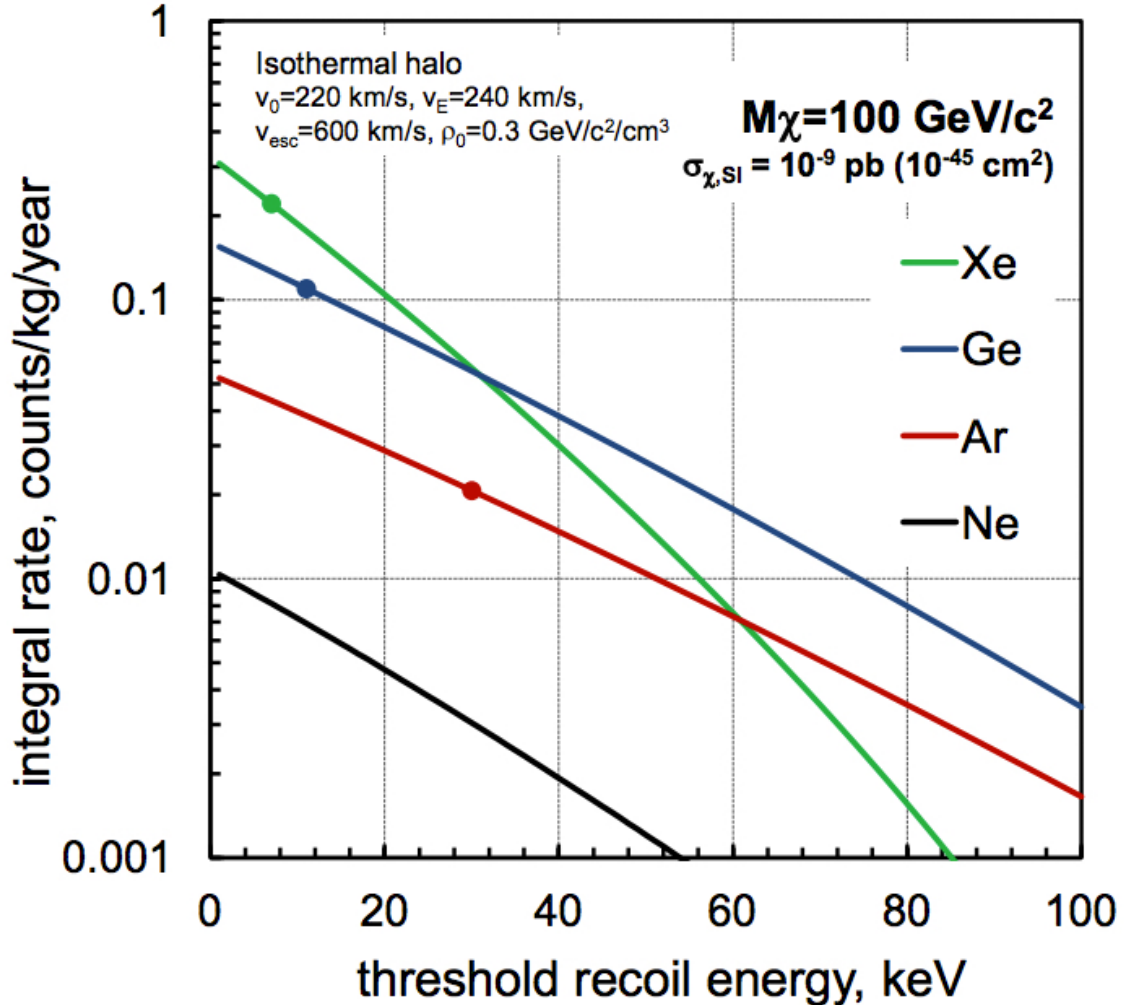


Figure 1.10: WIMP scattering rate as a function of energy taking into account the nuclear form factor. Xenon's large size is a double edge sword. At low energy, the  $A^2$  dependence of  $\sigma_{0,SI}$  wins out and xenon has a significant advantage over competing media. At large momentum transfers, however, decoherence dominates, forcing xenon to fall much more quickly than argon, neon, or germanium. Figure from [20].

Finally, chapter 5 will describe in detail the results from the novel  $^{14}\text{C}$  injection that occurred during the post run04 injection campaign. We will derive charge and light yields, as well as recombination fluctuations from energies ranging from 5-140 keV. We will also present a comparison to the theoretical spectrum.

## Chapter 2: Liquid Xenon Dark Matter Experiments

### 2.1 Liquid Xenon Microphysics

#### 2.1.1 Combined Energy Scale

#### 2.1.2 The NEST Model

### 2.2 The LUX and LZ experiments

Currently the most stringent limits on WIMP mass and cross section are set by the Large Underground Xenon (LUX) detector. The LUX-ZEPLIN (LZ) detector will be the successor to LUX and will have roughly 200 times greater sensitivity than LUX. LUX and LZ are two-phase xenon time-projection chambers (TPC's) designed to detect relic WIMPs in the local galactic halo scattering off of the target xenon nuclei.

If a WIMP interacts with one of the target atoms, it will deposit energy in the form of freed electrons, light, and heat. Two arrays of photo-multiplier tubes (PMT's) at the top and bottom of the detector detect the light emitted from this interaction as primary scintillation (S1). The electrons are drifted through an electric field to the top of the liquid where they are extracted and cause secondary scintillation light (S2) which is also detected by the PMT's. The x-y position of this event can be reconstructed mapping the relative signals from the S2 in the top PMT array. The depth of the event is given by the time separation between the S1 and S2. The relative size of the S1 and S2 will be different

depending on whether the interaction was with the xenon nucleus or an orbital electron. A WIMP will interact coherently with the nucleus, so it is 132 times more likely to interact with a xenon nucleus than with an electron. Since most of the background events in LUX are from gammas and betas, which interact with the orbital electrons, the ratio of S2 to S1 can be used to efficiently discriminate between background and signal.

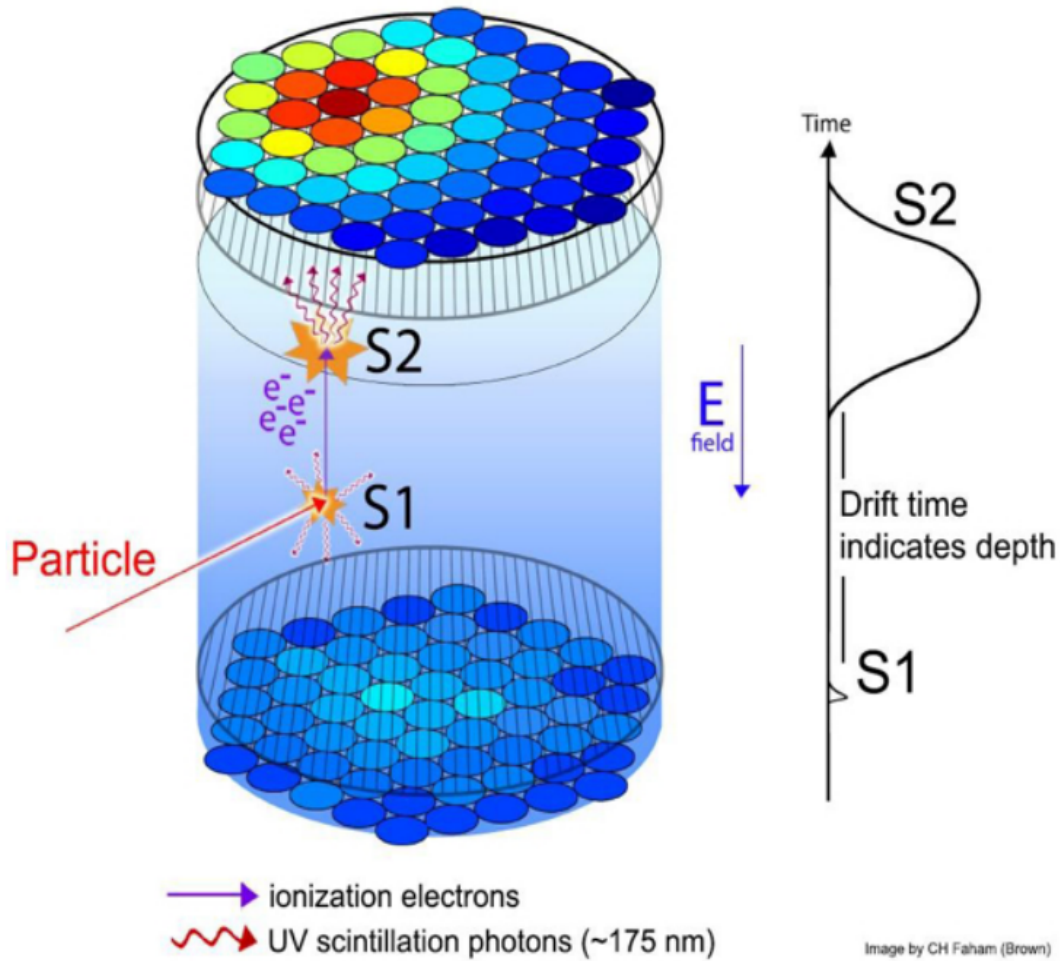


Figure 2.1: Schematic drawing of an event in the LUX detector.[5]

LUX is currently located at the Sanford Underground Research Facility in Lead South Dakota. It is 4850 feet underground (4300 m w.e.). The detector itself is immersed in a large water tank to shield it from neutrons and gammas. LUX contains about 370 kg

of xenon, and uses a fiducial volume containing about 118 kg as its WIMP target. The remaining xenon acts as a shield from external gammas and betas.

### 2.2.1 Electric Field Model

[8]

### 2.2.2 Efficiency Corrections

In run 4, the position-dependent efficiency corrections for the LUX S1 and S2 signals were obtained from a combination of tritium and  $^{83m}\text{Kr}$  calibration data using a procedure referred to as KrypCal[38].

### 2.2.3 Electron Trains in LUX Run04

## Chapter 3: Building, Optimizing, and Maintaining a Xenon Cold-Trap Sampling System

### 3.1 Technical Overview

A cold trap sampling system is designed to flow a sample of xenon with trace amounts of impurities through a section of liquid nitrogen cooled plumbing, to a mass-spectrometer for purity analysis. This document will deal particularly with krypton, but the method described also works for most simple impurities such as helium, argon, nitrogen, oxygen, methane, etc.. Less volatile impurities such as water and large hydrocarbons tend to freeze along with the xenon, so are not detected.

The operating principle is similar the that of freeze distillation. The bulk xenon is frozen to the cold plumbing leaving only the xenon ice vapor pressure at the output of the cold-trap. The flow of krypton is left largely unaffected. The resulting mixture which exits the cold-trap can be up to  $10^9$  times enriched in krypton. A cold-trap used in conjunction with a residual gas analyzer (RGA) whose sensitivity is about one part in  $10^6$ , is able to measure concentrations of krypton in a xenon sample down to the order of one part in  $10^{15}$ .

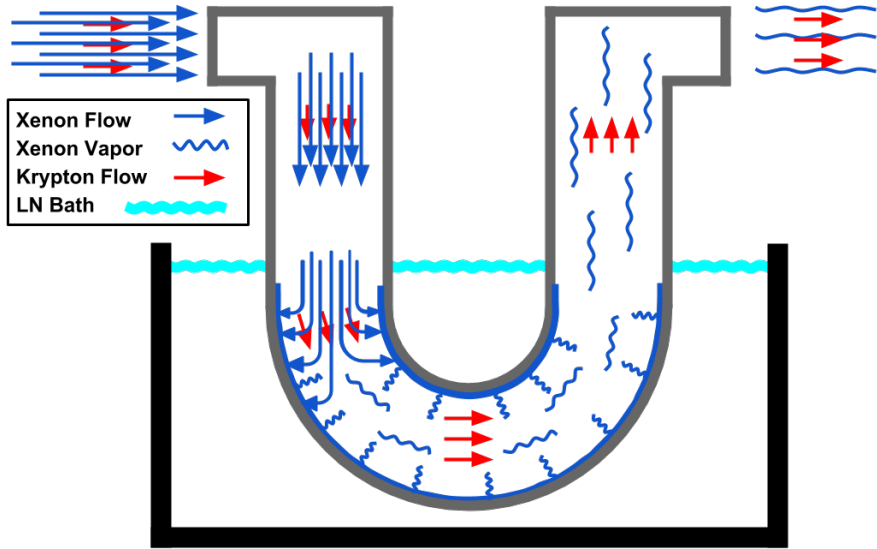


Figure 3.1: Cartoon version of what happens during a cold trap analysis.

### 3.1.1 System Construction

A cold trap sampling system should be laid out as described by figure 3.26. There will likely be additional transfer lines needed for collecting samples, recovering xenon, etc., but figure 3.26 fully describes the plumbing necessary to analyze a sample of xenon.

The system should have 100% metal-seals such as VCR or CF. Elastomer internals have the potential to become contaminated with krypton and destroy the sensitivity of the system and so should be limited. Traditionally, hardware used for this type of system is as follows:

- The plumbing should be entirely composed of UHP stainless steel.
- The sample bottle, SB, is a 1 gallon Swagelok DOT compliant sample cylinder.
- The valves, V1 through V7 are some type of high purity shutoff valve. For automated systems, the Swagelok DF series diaphragm valves with pneumatic actuators are

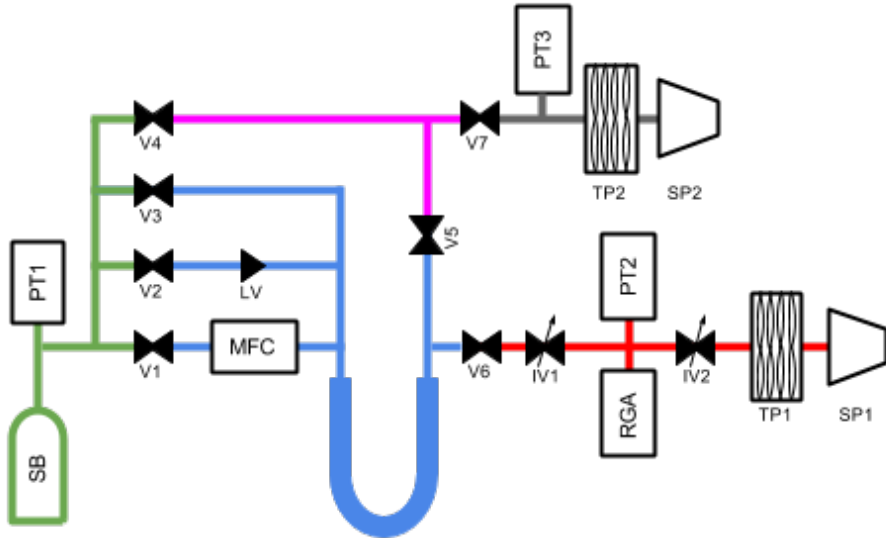


Figure 3.2: Plumbing diagram of a general purpose cold-trap sampling system. The green section is referred to as the sample volume, the blue section is the cold trap volume, and the red section is the RGA volume. These are the sections used during analysis of a xenon sample. The pink section is the bypass line which serves two purposes. It is used to relieve pressure in the cold trap while the system is warming and acts as the access line to the pump-out turbo pump, TP2.

used. When possible, it is better to use the Swagelok B series bellows valves with the spherical copper stem tip option, since the DF series has a polymer seat, however these are more difficult to automate.

- The sample pressure transducer is a capacitance manometer such as the MKS Baratron with a full scale of at least 3,000 Torr.
- The leak valve, LV, is a metering valve.
- The mass flow controller, MFC, should be metal sealed, and have a full range of about 10 SLM. The Celerity UNIT1660 is a good example. Although no longer in production, they are fairly easy to find used.

- The cold trap itself is some UHP stainless steel plumbing that is bent or welded into a shape that allows it to be submerged in a liquid nitrogen bath. Currently, the optimal cold-trap geometry is a 1/2 inch “stocking” trap, as described in section 3.3.1.
- Traditionally IV1 has been a Swagelok B series bellows valves with the spherical copper stem tip option, however it’s likely that the regulating stem tip would be better suited to the task.
- PT2 and PT3 are any cold cathode or inverted magnetron gauge that have an operating range of at least  $10^{-8}$  to  $10^{-4}$  Torr.
- The residual gas analyzer, RGA, is the SRS RGA200.
- IV2 needs to have a significantly lower impedance than IV1, so some type of 2.75” CF sealed all-metal vacuum valve should be used. A Varian UHV right angle valve, part No. 9515027 has been used in the past with good results.
- TP1 and TP2 are turbo-molecular pumps with pumping speed of at least 70 liters per second. The Varian V70, V81, and V84 have all been used with good results.
- SP1 and SP2 are the backing pumps for TP1 and TP2. They should be at least equivalent to the Agilent model SH110 scroll pump.

### 3.1.2 Operational Outline

The exact steps required for a particular analysis can be quite complex, and some detailed example procedures can be found in appendix ???. A general outline of the operation of a cold trap sampling system is as follows:

1. A xenon sample is collected and stored in the sample volume until the beginning of analysis.

2. The system begins with all the valves closed.
3. The cold trap is immersed in a liquid nitrogen bath, and base layer of xenon ice is formed.
4. Baseline pressures are measured by the RGA by opening V6, exposing the RGA volume the the xenon ice vapor pressure present in the cold trap volume. Usually these baselines are established over a period of ten or more minutes.
5. Leaving V6 open, V1 or V2 is opened, allowing the xenon sample to freeze into the cold trap at a controlled flow rate. This will usually takes several minutes.

As described in figure 3.1, the xenon pressure at the RGA will remain constant during this step, but there will be a flow of krypton at the output of the cold-trap which will cause a rise in the krypton partial pressure in the RGA volume. It is this partial pressure pressure rise that will be analyzed to give the concentration of krypton in the xenon sample.

6. After the sample volume has been exhausted, V1(2) will be closed, and the krypton partial pressure is allowed fall back to its prior value.

At this point, the purity analysis of the xenon sample has been completed, but the system is not in a safe state. Only a microscopic amount of xenon has been pumped out through TP1, so the full mass of the xenon sample is frozen in the cold trap. If this is allowed to vaporize without proper precautions, the RGA and TP1 could be damaged by over-pressure. It is therefore extremely important to isolate the RGA volume from the cold-trap volume before allowing the cold-trap to rise above liquid-nitrogen.

7. Close V6.

If the sample mass was large enough, there could be enough xenon ice in the cold trap to damage the system instrumentation or even cause the plumbing system to rupture once it

warms to the gas phase. This is why it is important to have rupture disks installed on the cold trap. To avoid damage to the system, the cold trap volume should be vented to the sample volume. Valve V3 provides a path from the input of the cold trap to the sample volume without the added impedance of the MFC or LV.

#### 8. Open V3.

This is where the bypass line comes in. With a cold-trap made from 1/2" plumbing, it is likely that an ice blockage will form once the xenon flow has stopped. This ice blockage could cause a dangerous pressure differential between the input and output of the trap. By opening the bypass line, the output of the cold trap has a second path to the sample volume.

#### 9. Open V4 and V5.

The system is now in a safe state and the cold trap can be allowed to warm back to room temperature. The remaining xenon can then be recovered or discarded as desired, after which the system should be pumped to vacuum before collecting the next sample. It is important to note that this pump-out should be done using TP2, since the RGA volume should be kept at vacuum except for maintenance. The bypass line, as configured, allows the cold-trap volume and sample volume to be pumped out independent of one another.

### 3.2 Idealized Cold Trap Response

In order to optimize the sensitivity of the cold-trap system, it is good to have an understanding of the basics of vacuum physics. A vacuum system can be analogized to an electrical circuit, with pressure taking the place of voltage, flow rate ( $Q$ ) taking the place of current, and impedance ( $Z$ ) taking the place of resistance. This analogy gives us with the equation:

$$\Delta P = Q \cdot Z \quad (3.1)$$

An important note here: in this document we use the generic  $P$  to denote a pressure at any specific point in the system, but reserve  $PP_s$  to represent the partial pressure of some species,  $s$ , as measured by the RGA. For instance,  $PP_{Kr}$  will refer to partial pressure of  $^{84}Kr$  as it is measured by the RGA, whereas  $P_{Kr,CT}$  will be used to represent the krypton pressure present in the cold trap.

Returning to the vacuum equations, it is now useful to define a new quantity,  $S$ , which is called the “volumetric flow rate” or “pumping speed”.  $S$  is defined:

$$S \equiv Av = \frac{dV}{dt} = Q/P, \quad (3.2)$$

where  $A$  is the cross-sectional area of the pipe, and  $v$  is the flow velocity, and  $dV$  is the volume of gas which passes a point in the system in time  $dt$ . An effective pumping speed can be calculated for any point in the vacuum system through the equation:

$$1/S_{eff} = 1/S_p + Z_{total}, \quad (3.3)$$

where  $S_p$  is the speed of the pump which is acting on the system, and  $Z_{total}$  is the total impedance between the pump and the specified point in the system. We can then calculate the steady-state pressure at any point in the system[46]:

$$P = Q/S_{eff}. \quad (3.4)$$

### 3.2.1 Vacuum Impedances

The calculation of system impedances depends on which flow regime a gas resides. The flow regime is determined by whether a given gas molecule interacts primarily with other molecules, or with the walls of the vacuum chamber. The flow regime can be characterized

by the Knudsen number,  $K \equiv \lambda/d$ , where  $\lambda$  is the mean free path, and  $d$  is the inner diameter of the vacuum chamber. For  $K \gg 1$ , a gas molecule is very likely to encounter the wall of the system before encountering another gas molecule; this is the molecular flow regime. When  $K \ll 1$ , the system is in the viscous flow regime where a gas molecule will be interacting predominantly with other gas molecules. If  $K$  is  $O(1)$ , the system is in what is referred to as the intermediate regime.[46]

In the molecular flow regime the impedance of a system element will depend on the geometry of the element, and on the molecular weight and temperature of the gas in question, but it will not depend on the pressure of that gas. For instance, the impedance of an aperture with area  $A$  will be given by:[46]

$$Z = \sqrt{\frac{2\pi M}{8kTA^2}}. \quad (3.5)$$

In the intermediate regime, the impedance picks up a complicated pressure dependence that can not be exactly calculated. Xenon gas inside the cold trap is at  $1.8 \times 10^{-3}$  Torr and 77 Kelvin.[29] In a 0.5" diameter cold trap the xenon has a Knudsen number of 0.6. This puts this section of plumbing in the intermediate gas flow regime rather than the molecular flow regime, and limits the accuracy of any results calculated using the molecular flow approximation. The role of vacuum equations in this document is to provide qualitative predictions on how the krypton pressure at the RGA will behave in response to changes in system parameters. The exact response of the system is always characterized empirically, as will be described in section ???. For this purpose, the molecular flow approximation will suffice to motivate and direct our empirical investigations.[46]

The particular impedances of interest here are impedance between the cold-trap and the RGA ( $Z_1$ ) and the impedance between the RGA and TP1 ( $Z_2$ ). IV1 and IV2 are in place so that  $Z_1$  and  $Z_2$  can be fine tuned to an optimal arrangement. This optimization will be

described further in section ??, but first there is a hard constraint that must be placed on the relative values of  $Z_1$  and  $Z_2$ .

The RGA has a maximum operating pressure of  $1 \times 10^{-6}$  Torr, although we have found that operating at about  $1 \times 10^{-5}$  Torr is possible with minimal degradation of the CDEM. When analyzing xenon samples with a concentration of about one part per million or less, the xenon partial pressure,  $PP_{Xe}$ , will dominate the absolute pressure at the RGA.  $PP_{Xe}$  is sourced by the vapor of the xenon ice in the cold trap, which is  $P_{ICE} = 1.8 \times 10^{-3}$  Torr, and so needs to be reduced by a factor of about 100 or more between the cold-trap and the RGA[29].

There are several compounding factors that come into play when deciding exactly what  $PP_{Xe}$  should be. These will be discussed in later sections, so we will take it as given here that the sensitivity is optimized between  $PP_{Xe} = 5 \times 10^{-6}$  Torr, and  $PP_{Xe} = 2 \times 10^{-5}$  Torr, and is largely unaffected by deviations within this range. For the sake of simplicity, we will usually demand that  $PP_{Xe}$  to be the default pressure that the system plumbing gives when IV1 and IV2 are maximized. For the system described above, the this pressure will be about  $1 \times 10^{-5}$  Torr.

To avoid saturation and mass-dependent effects of the RGA, we often use the doubly-ionized peak of the xenon-124 isotope as our measure  $PP_{Xe}$ . This peak appears at 62 amu, and so will be referred to as  $PP_{Xe62}$ . When the system is properly adjusted,  $PP_{Xe62}$  should be around 1,000 pTorr, or  $1 \times 10^{-9}$  Torr.

Returning to the vacuum equations we will see that although we have artificially defined  $PP_{Xe}$ ,  $Z_1$  and  $Z_2$  are not fully determined by this choice. By using equations 3.1 and 3.4, and the requirement that  $PP_{Xe} = 1 \times 10^{-5}$  Torr, we place a constraint on the impedances:

$$Q_{Xe,RGA} = PP_{Xe} S_{RGA} = \frac{P_{ICE} - PP_{Xe}}{Z_1} \approx \frac{P_{ICE}}{Z_1}, \quad (3.6)$$

where  $1/S_{RGA} = 1/S_{TP1} + Z_2$ . This gives,

$$S_{RGA} \cdot Z_1 = \frac{P_{ICE}}{PP_{Xe}} = 180. \quad (3.7)$$

$S_{RGA}$  is usually dominated by  $Z_2$ . Depending on the model of pump used, the speed of the turbo pump for xenon is around 50 liters per second. The impedance of cylindrical plumbing with a diameter of 1.5 inches is about  $\frac{1}{320}s/L$  per centimeter of plumbing.[46] In a typical system there will be the equivalent of about 5 feet of plumbing between the RGA and TP1, so the nominal value of  $Z_2$  will be roughly 0.48 seconds per liters for xenon, indicating a maximum  $S_{RGA}$  of 2.1 liters per second.[46] This means the fully-open value of  $Z_1$  should be about 85 seconds per liter for xenon. The exact numerical value of  $S_{RGA}$  and  $Z_1$  are largely unimportant, and when optimizing the system impedances as described in section ??, we will work in units relative to the fully open state, rather than liters per second.

### 3.2.2 Setting System Impedance

The sensitivity of a cold trap sampling system depends upon  $Z_1$  and  $S_{RGA}$ . We can adjust IV1 and IV2 to change  $Z_1$  and  $S_{RGA}$ , but wish to do so in a reproducible way. To this end, we look to the left hand side of equation 3.7 and see that  $PP_{Xe}$  is proportional to  $1/S_{RGA}Z_1$ . If we adjust IV1 while holding IV2 constant, we can use  $PP_{Xe}$  as a measurement of  $Z_1$  relative to its fully open state. Once  $Z_1$  has been adjusted to a desired set-point, we can use IV2 to adjust  $S_{RGA}$  until  $PP_{Xe}$  is restored to its pre-adjustment value.

For example, take the RGA trace shown in figure 3.3. In this case,  $PP_{Xe62} = 710 \pm 30$  pTorr when IV1 and IV2 are both fully open (region *I* in the figure). This state will be referred to as the 1x impedance state. In region *II* of figure 3.3 IV1 is partially closed until  $Z_1$  has increased by a factor of  $19 \pm 2$ . This has the effect of decreasing  $PP_{Xe62}$  from

$710 \pm 30$  pTorr in region *I* to  $38 \pm 5$  pTorr in region *III*. In Region *IV*,  $S_{RGA}$  is incrementally reduced by adjusting IV2 until  $PP_{Xe62}$  returns to  $710 \pm 40$  pTorr. This final state (region *V*) will be referred to as the 19x impedance state.

Equation 3.5 shows that  $Z_1$  will have a dependence on the molecular mass of the gas in question. The  $\sqrt{M}$  dependence means that the impedance for  $^{84}\text{Kr}$  ( $Z_{1,Kr}$ ) will be about 18% lower than the impedance for  $^{124}\text{Xe}$ . This is another reason to work in units of relative impedance rather than absolute impedance. A factor of 19 increase in impedance to xenon will mean that the impedance for krypton will also have increased by a factor of 19.

### 3.2.3 Generalized Cold Trap System Response

The operating principle of cold-trap sampling is that while the xenon gets frozen into the cold-trap, the trace gasses, such as krypton pass through. Another way to put this is that at the output of the cold trap the xenon is frozen to a constant pressure, while krypton mass flow is conserved. In practice, the conservation is not perfect, so we add a throughput constant,  $\alpha \equiv Q_{Kr,RGA}/Q_{Kr,CT}$ , where  $Q_{Kr,CT}$  is the flow rate into the cold trap, and  $Q_{Kr,RGA}$  is the equilibrium flow rate of krypton out of the trap, and the flow rate of xenon into the cold-trap ( $Q_{Xe,CT}$ ) is constant.  $Q_{Kr,CT}$  is equal to  $Q_{Xe,CT}$  times the concentration of krypton in the xenon sample,  $\Phi_{Kr}$ . These relations put together, give us the following equation:

$$Q_{Kr,RGA} = \alpha Q_{Xe,CT} \Phi_{Kr}. \quad (3.8)$$

Plugging this into the vacuum equations, we can find the relationship between the parameter of interest,  $\Phi_{Kr}$ , and the measurable quantities,  $Q_{Xe_0}$  and  $PP_{Kr,eq}$ :

$$PP_{Kr,eq} = \frac{\alpha}{S_{RGA}} Q_{Xe,CT} \Phi_{Kr}. \quad (3.9)$$

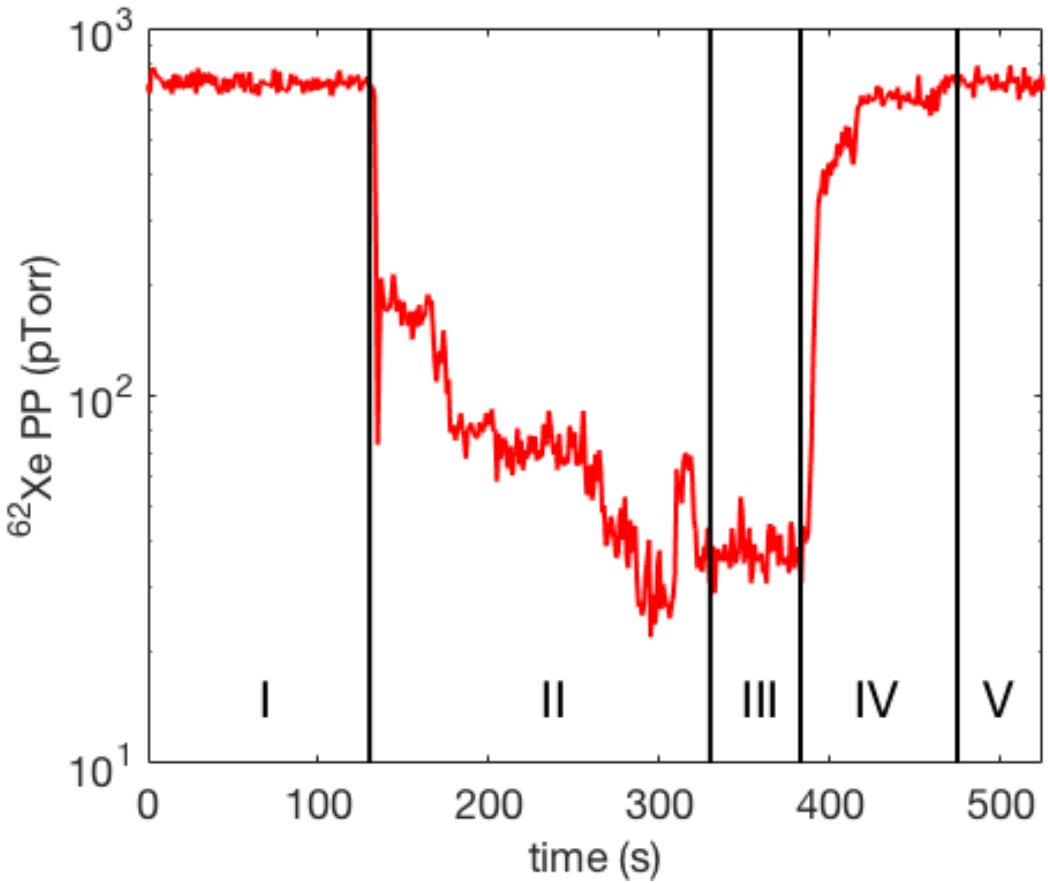


Figure 3.3: Adjustment of impedance to 19x state. Region *I* shows the fully-open, 1x impedance state of the system. In region *II*,  $Z_1$  is manually reduced using IV1, until region *III*, where  $PP_{Xe62}$  has dropped to 1/19<sup>th</sup> of its value in the 1x impedance state. In region *IV*,  $PP_{Xe62}$  is carefully increased back to its initial value by slowing down the effective pumping speed,  $S_{RGA}$ . In region *V*,  $PP_{Xe62}$  has returned to its initial value, and the system is in the 19x impedance state.

This relation shows the proportionality between partial pressure, and flow-rate times concentration that was found experimentally in [42] and [24]. By imposing the constraint from equation 3.7 we can see how altering the system impedance is expected to affect  $PP_{Kr,eq}$ , the equilibrium pressure of krypton at the RGA:

$$PP_{Kr,eq} = \frac{\alpha}{180} Z_1 Q_{Xe,CT} \Phi_{Kr}. \quad (3.10)$$

From the vacuum equations, we can also find the expected response of the system to an impulse of krypton. To do so, we would like to make the assumption that the RGA volume and the cold trap volume have a vanishingly small internal impedance, which means that the pressure at the input is equal to the pressure at the output. This is reasonable for the RGA volume which is constructed of 1.5 inch plumbing. However, we find that the bends in the cold trap plumbing cause this approximation to break down in when the xenon ice extends past the first leg of the trap. The effects of this breakdown will be discussed in a later section, but for now we will remain in the limit of small xenon flow rate and small xenon sample size where the approximation does provide largely valid predictions.

In a volume with no internal impedance, the amount of krypton contained by that volume is defined as  $P_{Kr}V$ . If the volume is being evacuated at a constant volumetric rate,  $S$ , while at the same time being sourced by some time-dependent flow rate,  $Q(t)$  the amount of krypton will change according to the equation:

$$V \frac{dP_{Kr}}{dt} = Q(t) - SP_{Kr}. \quad (3.11)$$

The response of  $P_{Kr}(t)$  to an impulse of flow,  $Q(t) = P_0 V \delta(t)$  is then:

$$P_{Kr}(t > 0) = P_0 e^{-t/\tau}, \quad (3.12)$$

where  $\tau = V/S$ . The time dependent  $P_{Kr}(t)$  can then be found by convolving  $Q(t)$  with this impulse response.

Applying this impulse response to the RGA volume ( $V_{RGA}$ ) and cold trap volume ( $V_{CT}$ ), we can find an expected time dependence of the krypton RGA pressure,  $PP_{Kr}(t)$ . The flow rate into the RGA volume is equal to the flow rate out of the cold trap volume, so it is given

by:

$$Q_{Kr,RGA}(t) = \frac{P_{Kr,CT}(t)}{Z_1 + 1/S_{RGA}} \approx P_{Kr,CT}(t)/Z_1, \quad (3.13)$$

where  $P_{Kr,CT}(t)$  is the time-dependent pressure of krypton in the cold trap volume. So to calculate the expected  $PP_{Kr}(t)$ , we must first calculate  $P_{Kr,CT}(t)$ . This can be done by convolving the known flow of krypton into the trap,  $Q_{Kr,CT} = \Phi Q_{Xe,CT}(t)$ , with the impulse response of the cold trap volume. We can then convolve the resulting  $Q_{Kr,RGA}(t)$  with the response of the RGA volume to predict the overall response of the system to the input flow rate.

The response time for the cold trap volume will be given by:

$$\tau_{CT} = V_{CT} \frac{1}{Z_1 + 1/S_{RGA}} \approx V_{CT} Z_1, \quad (3.14)$$

and the response time for the RGA volume will be given by:

$$\tau_{RGA} = V_{RGA}/S_{RGA}. \quad (3.15)$$

The condition  $Z_1 S_{RGA} = 180$  from equation 3.7, combined with the fact that in a typical system,  $V_{RGA} \approx V_{CT}$ , means that the RGA volume is expected to respond much more quickly than the cold trap volume. Therefore the overall response of the system will be dominated by the response of the cold trap, and the shape of  $PP_{Kr}$  will be well approximated by the shape of  $P_{Kr,CT}$ .

In this document we use flow rate profiles for xenon of the form:

$$Q_{Xe,CT}(t) = \begin{cases} Q_0 & \text{for } t \leq T \\ 0 & \text{otherwise} \end{cases} \quad (3.16)$$

If  $Q_{Xe,CT}(t)$  is given by equation 3.16, the instantaneous krypton pressure in the cold trap will be given by:

$$\frac{P_{Kr,CT}(t)}{\Phi Q_0 Z_1} = \begin{cases} 0 & \text{for } t < 0 \\ 1 - e^{-\frac{t}{\tau_{CT}}} & \text{for } 0 \leq t \leq T \\ (1 - e^{-\frac{T}{\tau_{CT}}})e^{-\frac{t-T}{\tau_{CT}}} & \text{for } t > T \end{cases} \quad (3.17)$$

Applying the response of the RGA volume gives the result:

$$\frac{PP_{Kr}(t)}{\Phi Q_0 / S_{RGA}} = \begin{cases} 0 & \text{for } t < 0 \\ 1 - e^{-\frac{t}{\tau_{RGA}}} - \frac{e^{-\frac{t}{\tau_{CT}}} - e^{-\frac{t}{\tau_{RGA}}}}{1 - \tau_{RGA}/\tau_{CT}} & \text{for } 0 \leq t \leq T \\ e^{-\frac{t-T}{\tau_{RGA}}} (1 - e^{-\frac{T}{\tau_{RGA}}} - \frac{e^{-\frac{T}{\tau_{CT}}} - e^{-\frac{T}{\tau_{RGA}}}}{1 - \tau_{RGA}/\tau_{CT}}) \dots \\ + \frac{e^{\frac{T}{\tau_{CT}}} - 1}{1 - \tau_{RGA}/\tau_{CT}} (e^{-\frac{t}{\tau_{CT}}} - e^{-\frac{t}{\tau_{RGA}} + T(1/\tau_{RGA} - 1/\tau_{CT})}) & \text{for } t > T \end{cases} \quad (3.18)$$

When  $\tau_{RGA} \ll \tau_{CT}$ , the right side of equation 3.18 reduces to the right side of equation 3.17. Combining this with the constraint from equation 3.7 yields:

$$PP_{Kr}(t) = \frac{Z_1 Q_0}{180} \Phi \begin{cases} 0 & \text{for } t < 0 \\ 1 - e^{-\frac{t}{\tau_{CT}}} & \text{for } 0 \leq t \leq T \\ (1 - e^{-\frac{T}{\tau_{CT}}})e^{-\frac{t-T}{\tau_{CT}}} & \text{for } t > T \end{cases} \quad (3.19)$$

Equation 3.19 does a good job in predicting the shape of  $PP_{Kr}$  when  $Q_0$  and  $Z_1$  are small as seen in figure 3.4. A fit to equation 3.19 produces a best fit time constant of 12.2 seconds. We measure the volumes spaces in our system by volume sharing with a known volume. The volume of the cold trap used in this trace was 183.8 cc, which would point to  $Z_1 = 66.7$  seconds per liter and  $S_{RGA} = 2.70$  liters per second.

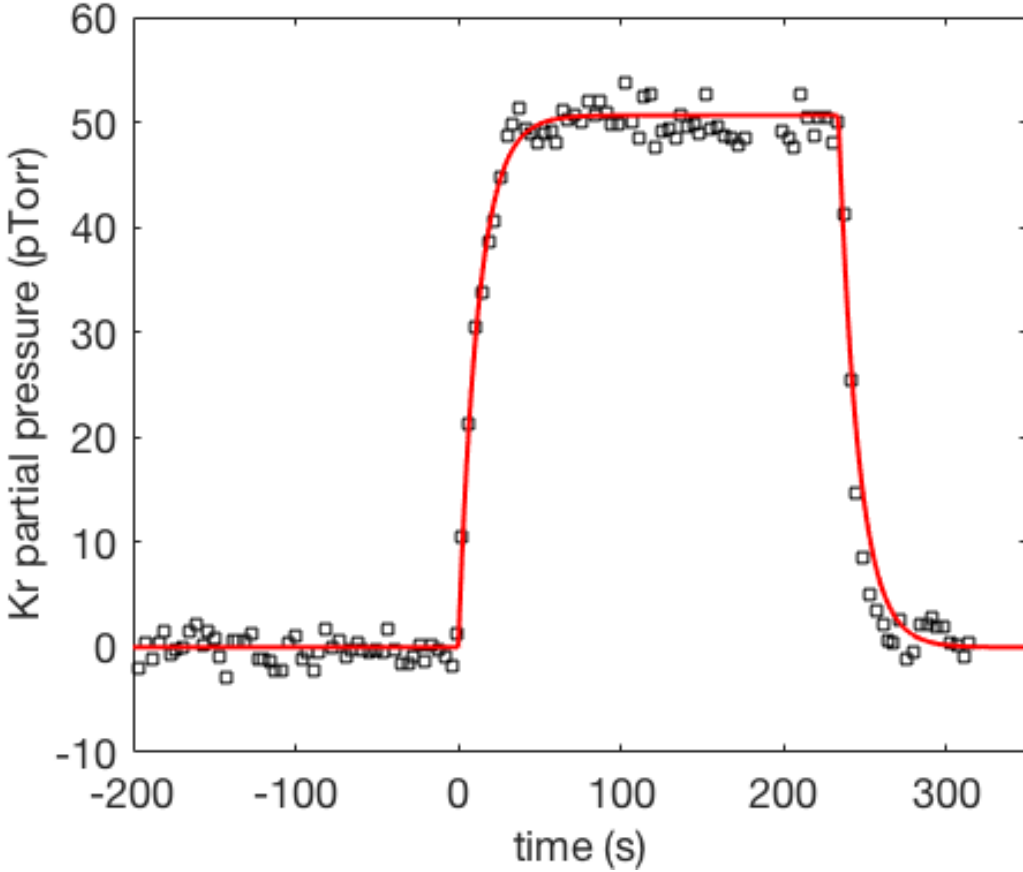


Figure 3.4: RGA trace with nominal impedance settings. Corrected for RGA gain, the equilibrium pressure of this trace is  $50.8 \pm 0.4$  pTorr.  $\Phi$  was known to be  $750 \pm 75$  parts per trillion (ppt) in liters of krypton per liter of xenon. The xenon flow rate used was 0.36 standard liters per minute (SLM).

### 3.3 Actual Behavior of a Cold Trap System

Equation 3.19 will prove itself powerful in characterizing  $PP_{Kr}(t)$ , as well as in providing motivation for the direction of our attempts at optimizing the cold trap system for the measurement of trace krypton contamination. It is, however an idealized equation that relies on some tenuous assumptions.

The vacuum approximation is not perfect, and there are large deviations from the molecular flow model presented in the previous section. We postulate that these deviations arise

from interactions between the flow of krypton and the formation of the xenon ice. The input of the trap has viscous xenon flow where the krypton is interacting primarily gaseous xenon atoms, while at the output of the trap, the xenon is closer to the molecular flow regime where the krypton atoms will be interacting more often with the stainless steel plumbing. More importantly, there is a transition region where the xenon is actively being frozen. This rapid phase transition of the xenon has complicated effects on the flow of krypton through the trap which result in krypton getting trapped inside the ice.

This trapped krypton is the physical basis for the throughput parameter,  $\alpha$ , presented in section 3.2.3. We consider two possible mechanisms for this entrapment; diffusion and entrainment. We take diffusion to be the passive absorption of krypton by already-formed xenon ice. This process will be governed by Fick’s laws, and so will be proportional to the krypton pressure at the surface of the ice, as well as the surface area of the ice present. We use the term entrainment somewhat loosely as a catch-all term for any effect that causes krypton to be encased in newly formed xenon ice as it is frozen. The major observable distinction between these two mechanisms is that entrainment will only occur when the xenon is actively being flowed into the trap, while diffusion can occur even over static ice. In this section we will present marginal evidence for both of these mechanisms and will characterize how the entrapment of krypton depends on xenon flow rate, system impedance, and the geometry of the cold trap.

### 3.3.1 Cold Trap Geometry

Before we analyze the performance of a cold trap sampling system, we must first select a geometry of cold trap to characterize. Historically we have used a 1.5 inch “U trap” (#6 in figure 3.5), but we have found that other geometries may serve us better. In general, we are looking for a trap that has a large capacity for xenon and a high krypton throughput.

We started by making variations of the our then-standard 1.5 inch U trap. We made a two additional U traps; one using 3/8 inch diameter plumbing and one using 0.5 inch plumbing. We measure the throughput parameter,  $\alpha$ , using the “left-over” method, which will be described in a later section. Our flow rate for these tests was controlled using a variable leak valve, through which a 500cc sample bottle was being exhausted. This does not give produce a constant flow rate, but does keep it to  $< 0.3$  SLM, putting these trials in the low flow regime where the throughput does not have a dependence on xenon flow rate. This will again be shown in a later section. The throughput appears to be larger for smaller diameter traps. The 1.5 in diameter trap was measured to have a throughput of  $(86.5 \pm 3.5)\%$ , which is in good agreement with our experience with 1.5 inch U traps. The 0.5 in trap had a significantly higher throughput of  $(92.5 \pm 2.5)\%$ , and the 3/8 inch trap throughput being about  $(90 \pm 5)\%$ . The other modification we made to the 1.5 inch U trap was to weld three of them in parallel, similar to trap #1 from figure 3.5, except with the bottle portion made using 1.5 inch tubing. The throughput of the 1.5 in triple trap was  $(70 \pm 6)\%$ , a significant reduction from the single U trap.

Moving on from the 1.5 inch U trap modifications, we decided to use 0.5 in plumbing in the construction of our traps. It sees about half of the krypton entrapment as the 1.5 inch trap and does not clog after  $< 10g$  of flow, as we found with the 3/8 inch trap. We did have some trouble with warm xenon gas breaking through to the output of the cold trap at higher flow rates. We welded a series of five traps with adding bends in the plumbing in order to increase the length of plumbing immersed in the LN. These traps are shown in 3.5. We measure  $\alpha$  for each of these cold traps, this time regulating the xenon flow with an MFC set to 3.3 SLM. 3.3 SLM is in the high-flow regime, so  $\alpha$  will be decreased from the low-flow values. These measured values of  $\alpha$  are shown in table ???. Refer to figure 3.5 for the description of the numbered cold traps. The results show that, while the additional bends do add more capacity to the trap, they can also reduce the krypton throughput.



Figure 3.5: Various cold trap geometries considered. We will refer to these geometries as follows: 1- Triple trap (0.5 inch). 2- Stocking trap. 3- Coil trap. 4- U trap (0.5 inch). 5- Boot trap. 6- U trap (1.5 inch). Not shown: 3/8 inch U trap. 1.5 inch triple trap.

Trap #	1	2	3	4	5
$\alpha$	0.70	0.76	0.38	0.84	0.38

Table 3.1: Throughput parameters measured for various cold trap geometries.

Table ?? indicates that trap #2 has the best throughput apart from the U trap (trap 4#). We have dubbed this the “stocking trap” because of its resemblance to a stocking, as well as because we first installed it on the system on Christmas, 2015. The stocking trap is capable of freezing about 120 grams of xenon before break-through, and only retains about 50% more krypton than the 0.5 inch U trap. For the rest of this document, when we refer to “the 0.5 inch diameter cold trap”, we will in fact be referencing the stocking trap, whereas when we refer to “the 1.5 inch diameter cold trap”, we will be referring to the 1.5 inch U trap.

### 3.3.2 Formation of Xenon Ice

The xenon ice forms in a short segment of plumbing relative to the approximately one foot length of the cold trap. The enthalpy of sublimation for xenon is about 15.95 kJ/mol at 77 kelvin.[29]. There is an additional 2.73 kJ/mol required to bring the xenon gas temperature down from 295 to 77 kelvin. A 0.36 SLM flow rate is equal to 0.267 mmol/sec of xenon, which requires 5.0 Watts to freeze. If we take the thermal conductance of stainless steel to be 10 W/m K, the maximum cooling power of a 12.7 mm diameter, 1.24 mm thick cold trap will be 70 W/mm.

We must also consider the heat transfer from the LN to the stainless steel trap. The heat transfer rate from LN to a stainless steel surface is highly dependent upon the temperature difference between the bulk LN and the surface. This temperature dependance has a maximum, referred to as the critical heat flux, where the LN changes from “nucleate boiling” to “film boiling”. Film boiling takes place when the LN boils rapidly enough to create an insulating layer, or “film”, of nitrogen gas between the LN bath and the stainless steel surface. The critical heat flux of Stainless steel to LN is on the order of  $10 \text{ W/cm}^2$ , putting the maximum heat transfer to our 12.7 mm (0.5 inch) diameter cold trap at about 4 W/mm, making it the limiting factor in the heat transfer to the plumbing.[54] Similarly, a 1.5 inch diameter trap would have a heat transfer of about 12 W/mm, and a 0.25 inch trap would have a heat transfer of about 2 W/mm.

The above estimates of the heat transfer indicate that at flow rates  $< 1 \text{ SLM}$ , all of the xenon should be frozen within the first centimeter or so of cold plumbing. We can approximately measure the length of the ice-forming region in two ways. First, the length of this region is inferred by observing the bubble formation within the liquid nitrogen bath. As the xenon flow is frozen inside of the trap the heat is transferred to the LN bath, and the liquid nitrogen that is in contact with the ice forming region boils. In order to visually

inspect the formation of xenon ice, we also installed a quartz window on the input and output of a cold trap. At low flow rates (< 1 SLM), both of these methods indicate that the ice formation region is less than about 1 cm in length. When viewing the ice formation through a window, there is a clear collar of xenon ice that forms in the input side of the trap at the level of the LN bath, and there is no visible ice formation anywhere else. When observing the outside of the trap, the LN appears to boil where the plumbing enters the bath but nowhere else. In this low-flow regime, the ice collar will expand in depth as more xenon is added until it fully clogs the trap. Flowing at about 0.3 SLM, a 1.5 inch trap will clog after about 400g of xenon has been frozen, while a 0.5 inch trap will clog after only about 70g at 2 SLM.



(a) Ice collar forming.



(b) Fully clogged trap

Figure 3.6: Two images of how ice is formed in a cold trap. The left image shows a thick collar of ice beginning to form. This collar contains > 100 grams of xenon ice. The right shows the collar after it has fully clogged the 1.5 inch diameter cold trap. This plug has roughly 400 grams of xenon is.

At higher flow rates (> 1 SLM), the ice no longer forms a collar, but rather a sleeve along the inside of the trap. This is likely due to the xenon ice forming an insulating layer over the stainless steel, thereby reducing the cooling power of that segment of plumbing

to the point where it is no longer able to freeze the xenon. In the high flow regime, the LN will still only boil along a short segment of plumbing, but this segment can be seen to migrate along the trap from input to output. Eventually, enough of the trap surface is covered that the trap is no longer able to maintain a constant xenon temperature at the output and the xenon pressure at the RGA rises. We call this effect xenon break-through, and is avoided whenever possible. The xenon pressure is already set to be higher than the operational pressure of the RGA, so any significant increase above this set-point could cause damage to the RGA. Additionally, either from physical effects inside the cold trap or from electronics effects of the RGA becoming over-pressured,  $PP_{Kr}$  tends to drop in the xenon break-through region limiting the usefulness of any data taken in the region.

In addition to the considerations from actively forming xenon ice, there are also issues and dependencies that arise from ice that was formed in the cold trap prior to beginning flow. In the high-pressure in which we operate the RGA, the RGA electronic baseline offset is highly dependent on the pressure of xenon. This means we need the xenon pressure to be extremely stable over the course of the xenon flow, otherwise we may see a false krypton signal caused by a rising electronic offset. To this end, we must form a small kernel of ice prior to an analysis run so that once xenon flow starts the electronic baseline at a xenon ice pressure will already have been established.

To see the possible effects of failing to maintain a stable xenon pressure we look to figure 3.8. In looking for a genuine krypton signal, we can check that the mass abundances are correct. The 84 amu line should be roughly 3 times more prominent than the 83 amu line. Additionally, there should be no pressure at 87 amu, so this line will be a good tracer for the baseline offset. For the purposes of this plot, we do a standard normalization ( $P_{norm} = \frac{P - \mu}{\sigma}$ ) on all four pressure traces in order to put them on the same scale. The xenon pressure was not well controlled for this run and rose by roughly  $2\sigma$  when the flow was started. We also saw a corresponding  $2\sigma$  rise in both of the krypton traces as well as the 87

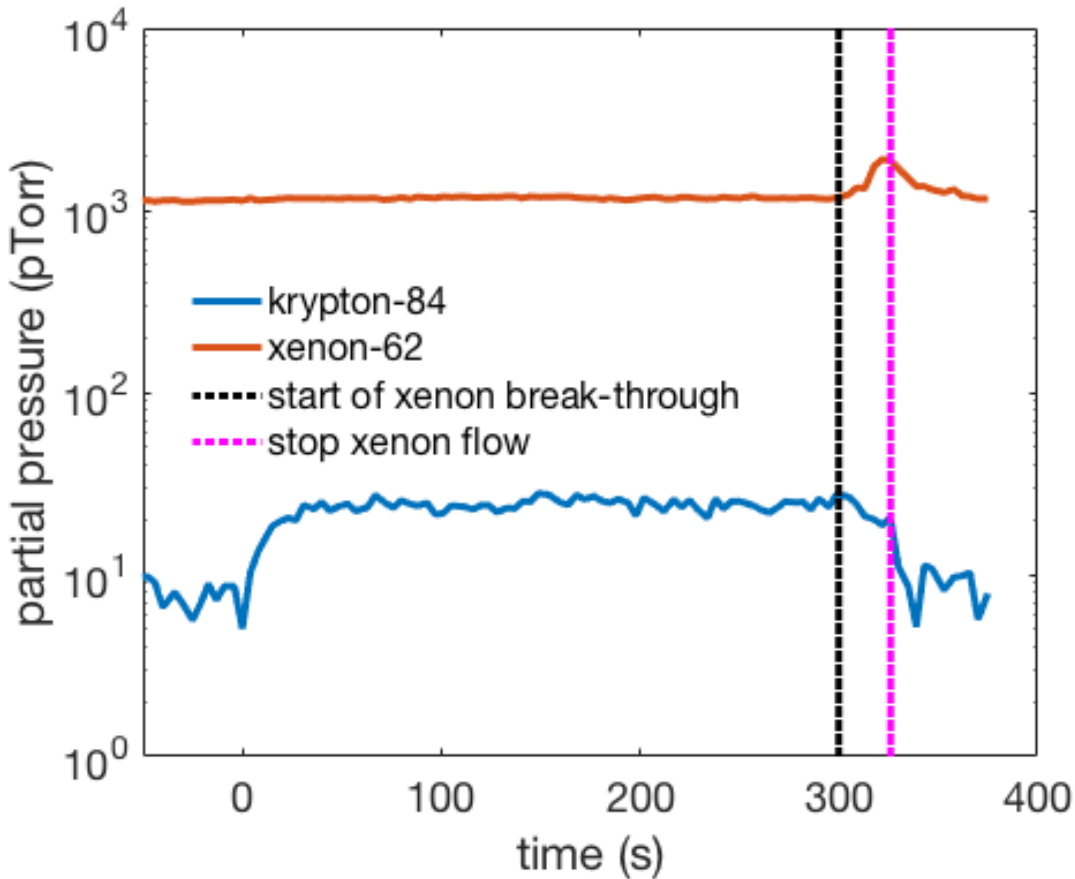


Figure 3.7: Break-through of xenon to the RGA, through a 0.5 inch trap. 4 SLM xenon flow was started at  $t=0$  seconds, and xenon breakthrough occurred  $300 \pm 5$  seconds later. This means that about 120 grams of xenon ice formed before flow was shut off; approximately double the amount in an ice plug formed in the low flow regime.

amu baseline-tracker line. The rise in the krypton lines are clearly not genuine, but rather an artifact of a shifting electronic baseline offset. These false signals are extremely dangerous in that they can mimic a genuine signal in excess of 10 times our limit of sensitivity. To insulate ourselves against this possibility, we always track multiple krypton masses, and use their signal ratios as a quality check. We also track a baseline tracer such as 87 amu and xenon pressure. If either of these has a statistically significant rise during the analysis run we mark the measurement as untrustworthy.

We maintain xenon pressure during an analysis run by forming an initial kernel of ice,

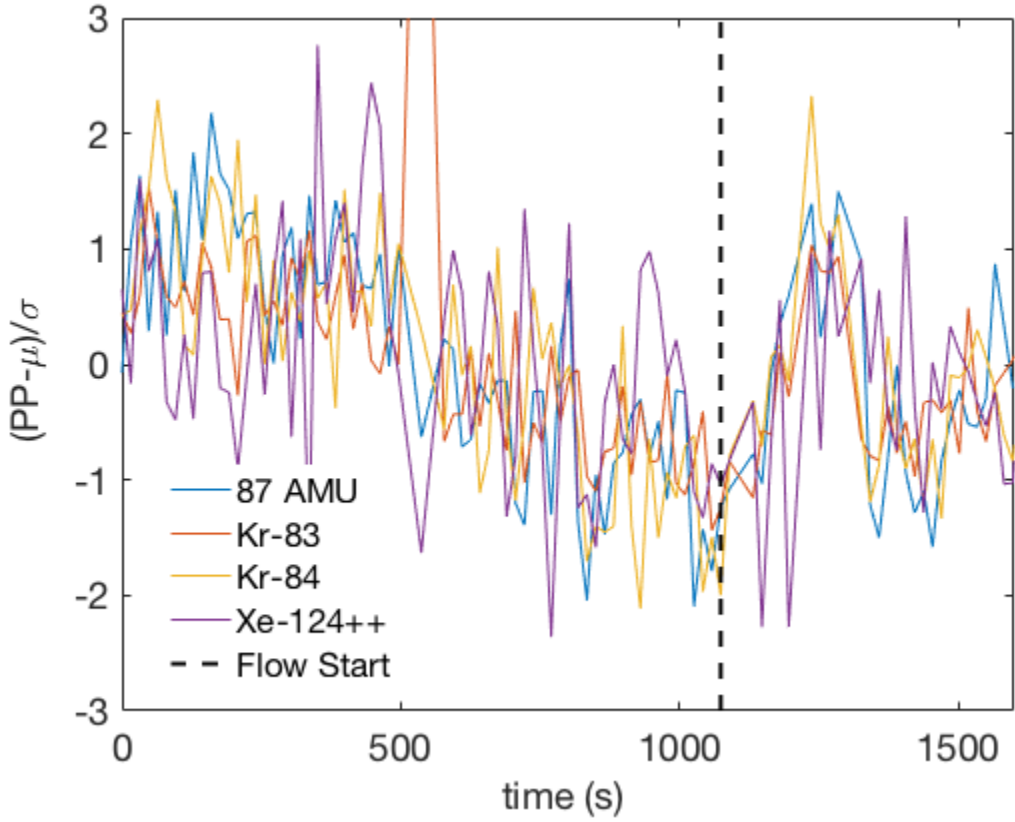


Figure 3.8: Data from an analysis run with poorly controlled xenon pressure. The krypton-83 and -84 lines, as well as a baseline tracer at 87 amu all tracked the drifting xenon pressure exactly.

onto which the rest of the xenon will be frozen. The way this kernel is distributed through the trap has some effects on the response of the trap. We examine three methods of forming the ice kernel, along with their impacts of the ultimate sensitivity of the system.

We begin with the simplest method of forming an ice kernel. We inject roughly 10 standard cc's of xenon into the input of the trap in order to form the base of the ice collar. This procedure does not, however, adequately maintain xenon pressure during xenon flow. When we flow xenon at a rate of 2.5 SLM, we see a rise in both the electronic baseline and the xenon partial pressure of, on average,  $4.2\sigma$ . By dumping xenon into the ice collar, we are increasing the temperature of the collar, and therefore are increasing the vapor pressure above it. We might expect that this high-vapor pressure xenon will be frozen at some point

further along the trap, thereby maintaining the pressure at the output. However, this xenon elevated xenon pressure seems to be low enough that it will not readily freeze to the cold stainless steel of the trap, and will maintain its elevated pressure all the way through the trap.

To prevent the xenon vapor pressure from rising, we modify our kernel formation technique in order to provide nucleation points for sublimation in the middle and output of the cold trap. We do this by filling the warm cold trap with the full sample pressure of xenon, usually about 2,000 Torr. We then isolate the trap and immerse it in the LN bath allowing this 2,000 Torr of xenon to freeze along the full length of the immersed plumbing. We then add an output kernel by injecting about 10 standard cc into the output of the trap, through V5. Using this method of kernel formation prior to flowing at 2.5 SLM, the change in xenon pressure and baseline offset are reduced to an average of  $-0.85 - \sigma$ .

Although this method appears to be successful in eliminating, it brings with it two problems. The first problem is that as the LN bath evaporates, the height of the bath may lower below the output kernel. If this happens, the xenon partial pressure at the RGA will rise, leading to a rising baseline. To counter, this we form the kernel with the trap not yet fully submerged in the bath. Once the kernel has been formed, we immerse the trap the rest of the way.

The second problem with this modified technique is that the ice sleeve can interfere with the krypton throughput, thereby reducing  $PP_{Kr}$ . This seems to only occur if a large enough amount of xenon ( 500 standard cc) is used in the formation of the kernel. If we use only about 50 standard cc of xenon, this effect seems to go away without loss in baseline stability.

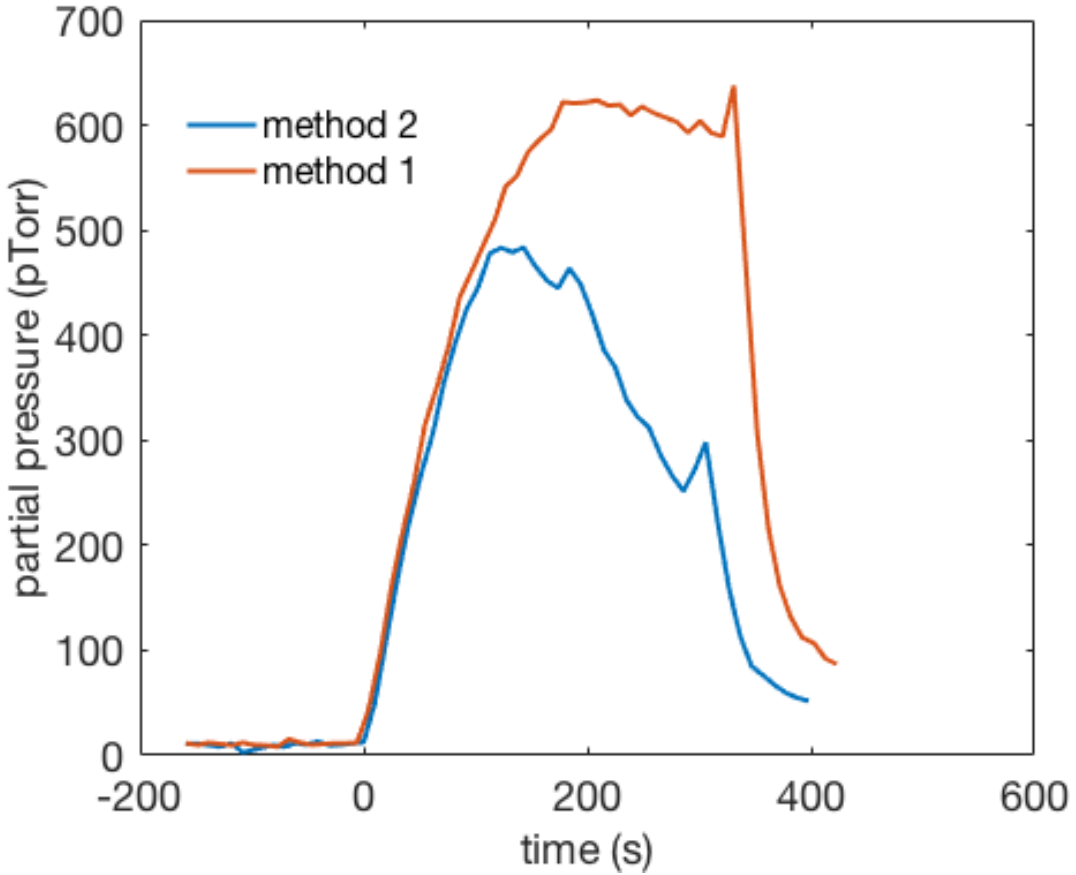


Figure 3.9: Krypton trace using the initial and modified method's prior to 2.5 SLM xenon flow, and a 90x impedance setting. For the method 2 trace we used 2500 Torr (600 standard cc) to for the kernel. This trace begins on the trend as method 1, but sees a sharp turn over and maxes out at only 63% of the method 1 peak.

### 3.3.3 Flow Rate Dependance

As mentioned previously, there are two distinct regimes of xenon flow in a cold trap sampling system: the low flow regime in which all of the xenon ice is formed within millimeters of the LN surface level, and the high flow regime in which the xenon ice forms a sleeve, which eventually can reach the output side of the trap and cause the RGA xenon pressure to rise. In the low flow regime, the response of the sold trap system to flow rate is extremely linear. In the high flow regime this linearity breaks down. As the ice

sleeve rounds bends in the trap the interaction between the krypton flow and the xenon ice formation changes. These changes work to lower the krypton pressure at the RGA from the exponential response predicted in equation 3.19, as can be seen in figure 3.10.

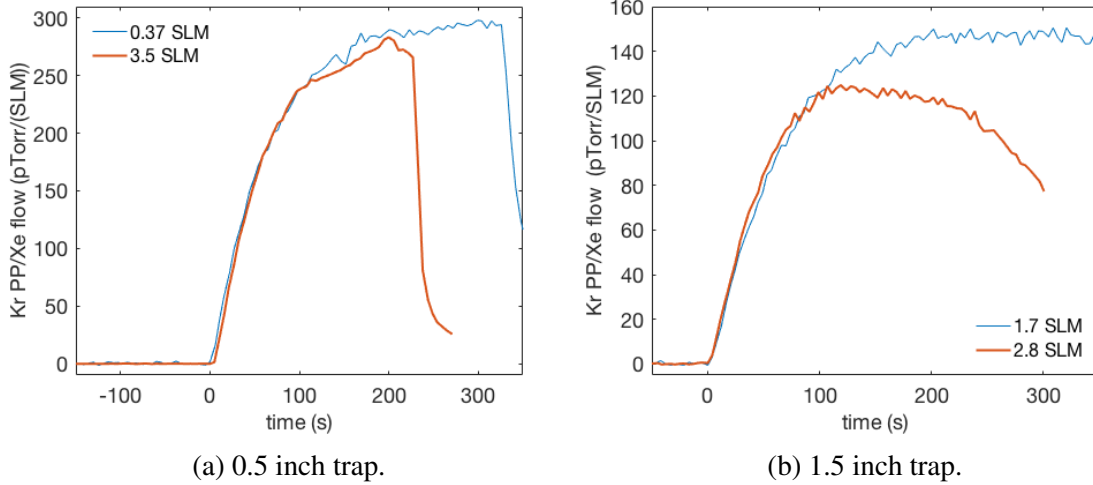


Figure 3.10: Krypton pressure traces resulting from high and low xenon flow regimes. Note the two sharp kinks in the 0.5 inch trend. These correspond to sharp 90-degree bends in the tubing of the trap which were formed using a standard tube-bender. The rounded turns in the 1.5 inch trend correspond to the more gentle bends in the 1.5 inch tubing. These bends are built by welding two elbow pieces together. These measurements were taken in the 15x impedance state.

We do not have a satisfactory explanation as to the physical basis of this drop in krypton pressure at the RGA. Speculations could be made, but in the end we are only interested in how this phenomenon will affect our sensitivity to krypton. To characterize the impacts that flow rate has on the krypton response, we run tests at various flow rates and track the maximum pressure the krypton trace reaches at each setting. We also repeated this flow-rate scan for several impedance states. Above about 2 SLM, the turn-over effect shown in figure 3.10 begins competing with the idealized response described in equation 3.19. This effect is more pronounced at higher impedance settings, but can be clearly seen even in the 1x impedance scan above about 6 SLM.

The turn-over effect is so dominant in the flow rate dependence of  $\alpha$ , that it obscures other possible effects. The usual method of calculating the equilibrium krypton pressure,

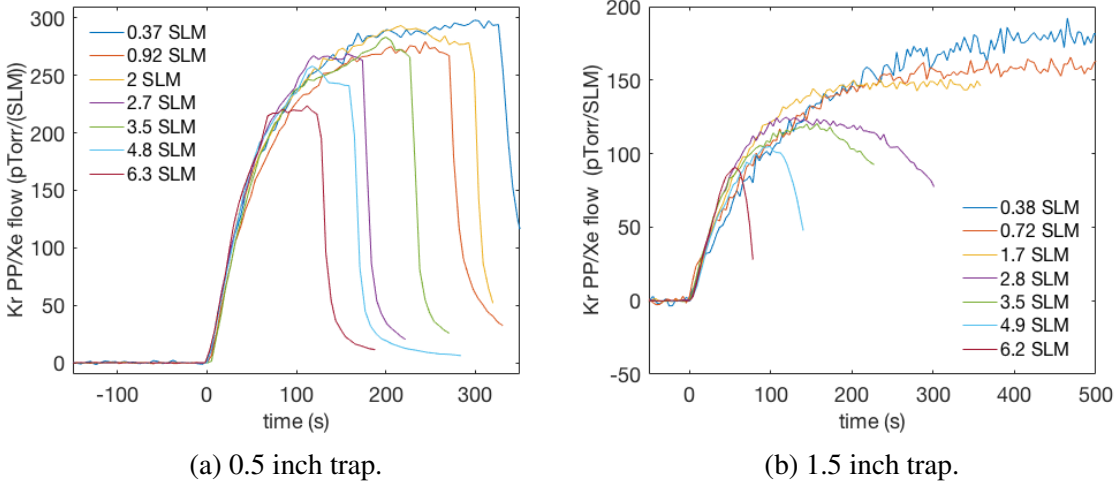


Figure 3.11: Krypton RGA traces normalized to xenon flow rate at various flow rate settings. These traces are all measurements of identical xenon, with an impedance setting of 15x. The response of the system to flow rate appears to be largely linear until about 2 SLM. After this point the Kr trace falls increasingly down from the low-flow traces.

$PP_{Kr,eq}$  is to flow xenon until  $PP_{Kr}(t)$  levels off to a constant value. The data in this constant region is then averaged to find  $PP_{Kr,eq}$ . However, the turn-over effect can create a false plateau in the  $PP_{Kr}(t)$  data which invalidates this flat-top averaging method. To account for this effect we can look only at the portion of  $PP_{Kr}(t)$  before the first turn-over. This will be data from the time when ice is forming only in the first segment of the cold trap, before the ice sleeve grows around the first bend. If we fit the exponential response from equation 3.19 to this first segment of  $PP_{Kr}(t)$ , we can estimate what  $PP_{Kr,eq}$  would be without the turnover effect.

At low flow rates, the extrapolated values of  $PP_{Kr,eq}$  are equal to the flat-top averages. This is expected, since the xenon flow is in the regime where all of the ice is formed in the first leg of the trap, and the turn-over effect does not come into play. At higher flow rates, when the turn-over effect begins to turn on, the two  $PP_{Kr,eq}$  values begin to diverge. The exponential fit values continue on a linear trend, while the flat top averages fall off of this linear trend. Returning to equation 3.10 we see that  $PP_{Kr,eq}$  can only remain linear with

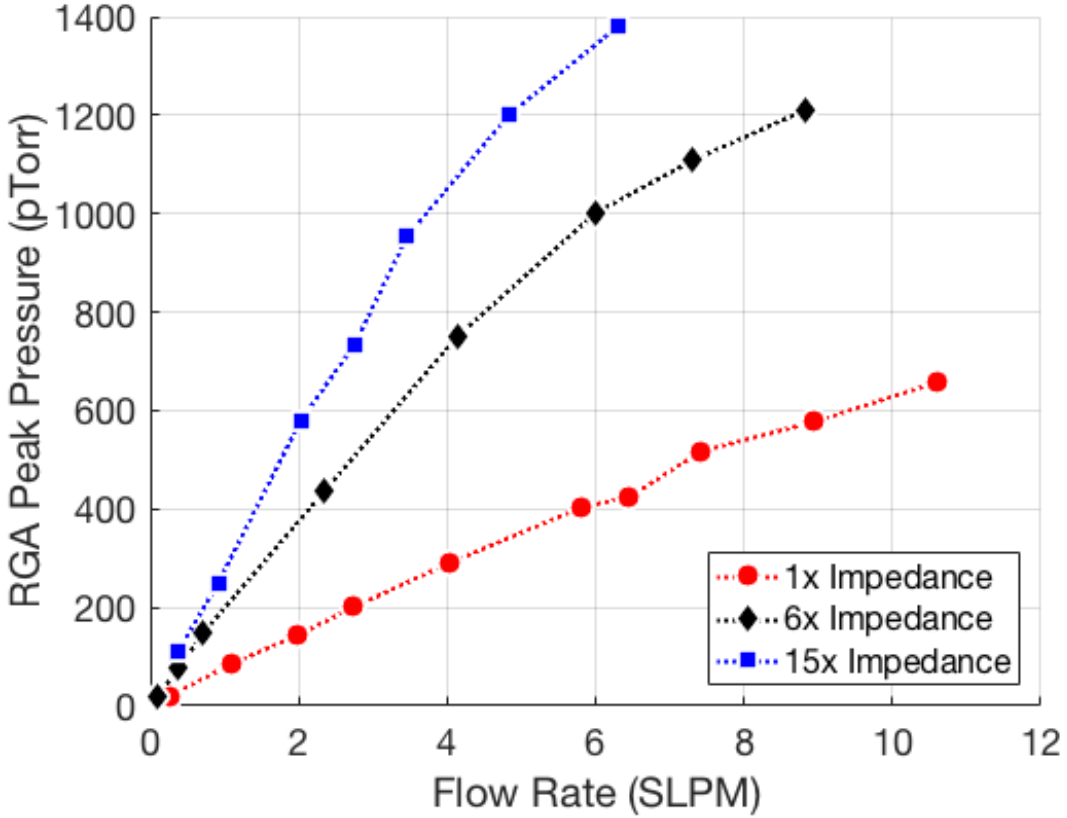


Figure 3.12: Peak krypton RGA pressure as a function of flow rate, and at varying impedance settings. The data for this plot was taken with a 0.5 inch diameter cold trap.

flow rate if  $\alpha$  has no flow rate dependence. From the fact that the exponential fit values do remain linear, we conclude that  $\alpha$  is not inherently affected by xenon flow rate, but rather picks up an effective flow rate dependence because of the turn-over effect.

### 3.3.4 Impedance Dependence

The predictions of equation 3.19 also break down at high system impedances, although perhaps in a more well-behaved way than in the case of high xenon flow rates. Just as with increased xenon flow rate, the  $\alpha$  parameter will increase at higher impedance settings. However, as opposed to its turn-over induced, effective dependence on flow rate,  $\alpha$  appears

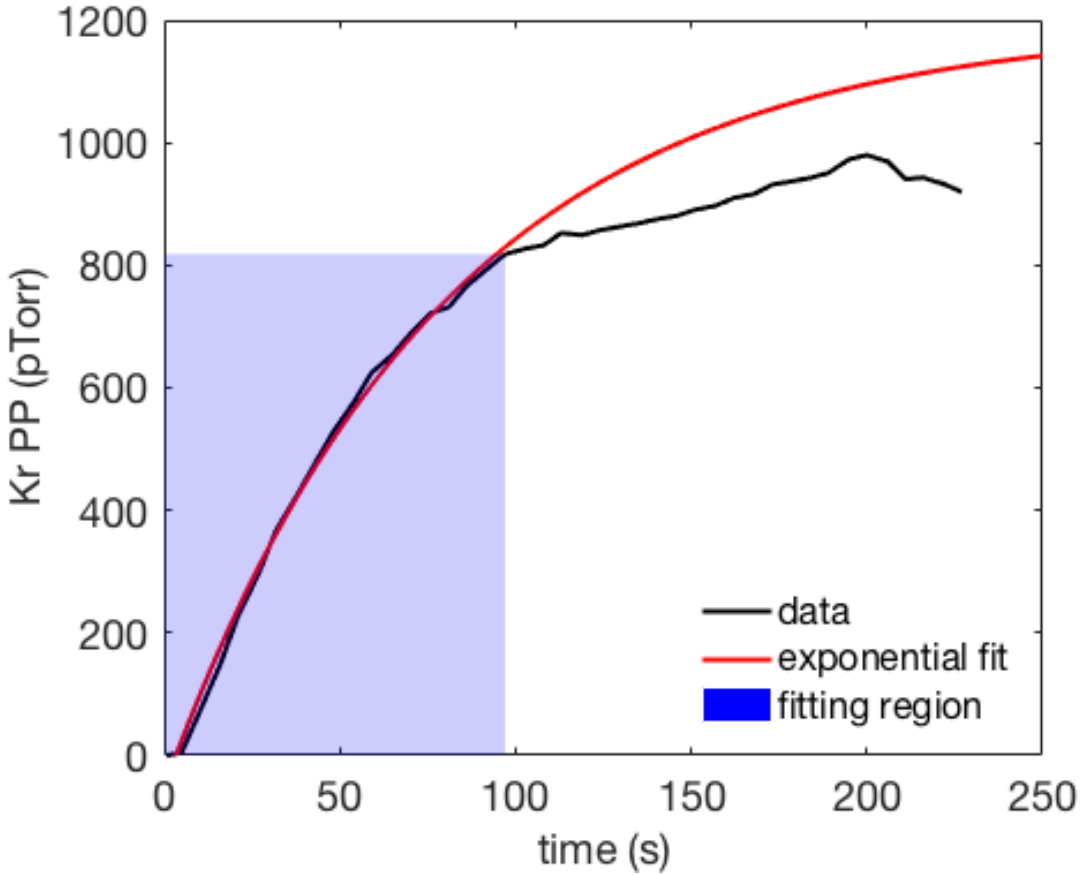


Figure 3.13: An example of fitting an exponential response to the first part of  $PP_{Kr}(t)$ . This is the same data plotted in figure 3.10a

to have a more fundamental relation to impedance that can be used to characterize the physical basis of the entrapment of krypton in the cold trap.

Consider the pressure trace shown in figure 3.15; the xenon flow rate,  $Q_0$  and krypton concentration,  $\Phi$  were identical to the krypton trace in figure 3.4, and the impedance,  $Z_1$  was set to be 45 time higher. This trace deviates significantly from what would be expected by increasing  $Z_1$  in equation ???. Both the system response time and equilibrium pressure are expected to increase proportional to  $Z_1$  from equations 3.14 and 3.10, but had a significantly smaller increase.  $PP_{Kr,eq}$  increased from  $50.8 \pm 0.4$  to  $399.9 \pm 1.7$  pTorr; a factor of 7.9. The overall response time,  $\tau$ , increased from  $12.7 \pm 0.7$  to  $93.4 \pm 1.8$  seconds; a factor

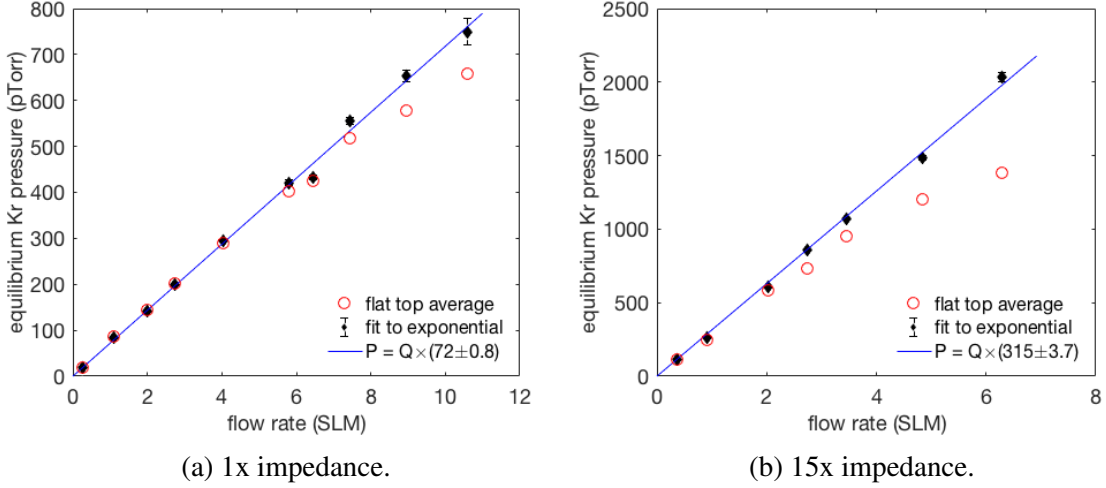


Figure 3.14: Comparison of the flat-top averaged  $PP_{Kr,eq}$  the extrapolated equilibrium value calculated from a fit to an exponential response.

of 7.4.

It is an interesting point of fact that the discrepancy in both  $PP_{Kr,eq}$  and  $\tau$  from the predicted results are approximately the same. In fact, although  $PP_{Kr,eq}$  and  $\tau$  do not remain proportional to  $Z_1$ , they do remain proportional to each other. One explanation for this would be that our measurements of  $Z_1$  and  $S_{RGA}$  are incorrect, and the impedances are not being increased as much as we have calculated. However, this would only satisfy the proportionality of  $PP_{Kr,eq}$  and  $\tau$  if the throughput parameter,  $\alpha$  is constant with impedance.

In order to measure  $\alpha$ , we can measure the concentration of krypton in xenon which is left over from an analysis. After flowing a sample into the cold trap for analysis, the sample bottle will be left empty, and all of the xenon (minus a microscopic amount that gets pumped out past the RGA) will be frozen in the cold trap. Along with this frozen xenon will be the krypton that was trapped. We can then transfer this new mixture back into the sample bottle and run a second pass analysis. The ratio of  $PP_{Kr,eq}$  from the second pass to the first pass will be equal to the fraction of krypton which gets trapped in the cold

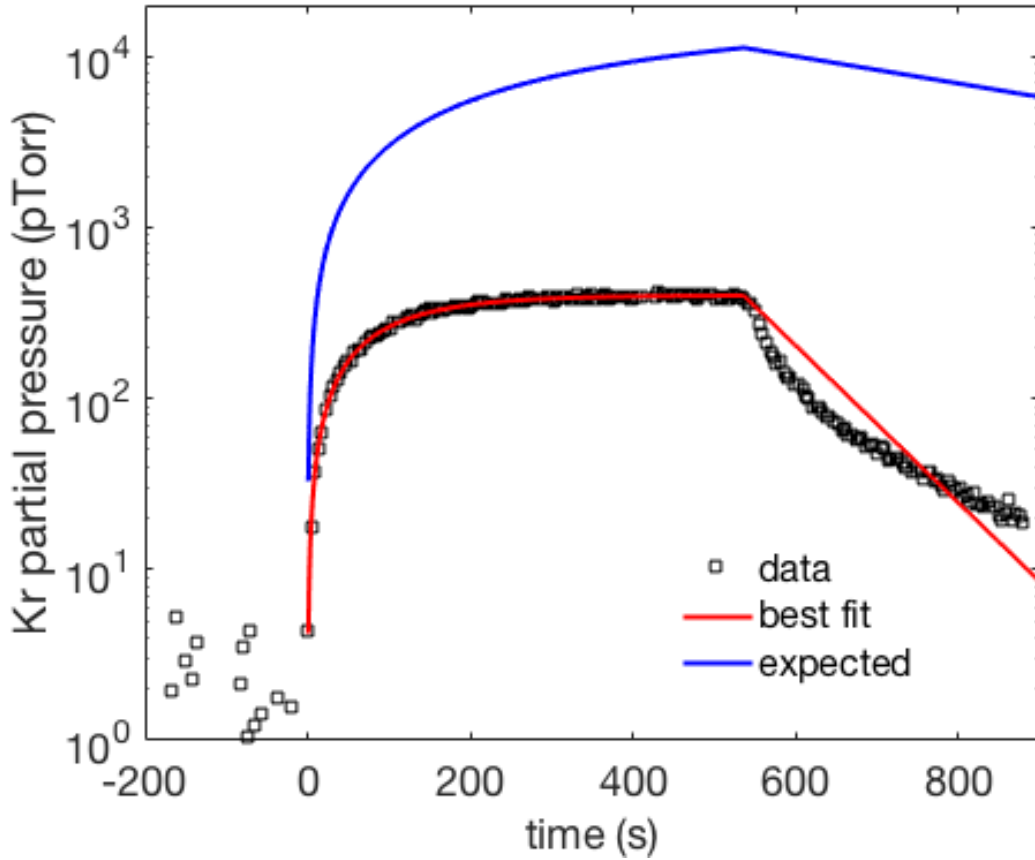


Figure 3.15: RGA trace with 45x impedance settings.

trap. This ratio will also be equal to  $1-\bar{\alpha}$ . It may be that the throughput parameter during the transient rising section of  $PP_{Kr}(t)$  will be different from the equilibrium value. In this case, the averaged  $\bar{\alpha}$  will differ from the equilibrium value of  $\alpha$  which is presented in section 3.2.3.

Measurements of  $\bar{\alpha}$  over a series of impedance settings show that the throughput is decreasing at higher impedances. This means that the fact that  $PP_{Kr,eq}$  is not linear in  $Z_1$ , as is predicted by equation 3.19, cannot be fully explained by faulty impedances measurements.

Now that we have established that the krypton throughput is reduced at higher impedances,

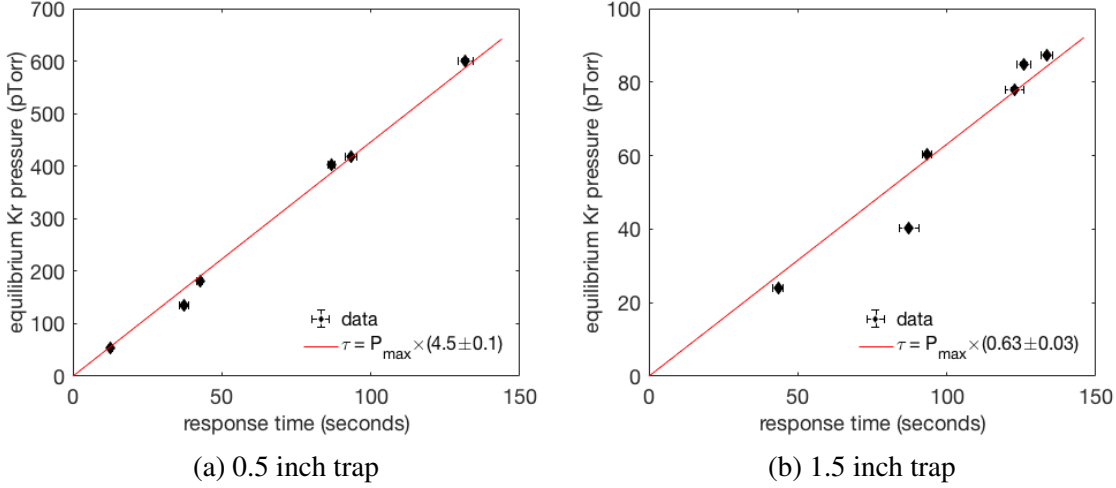


Figure 3.16: Linearity of the characteristic response time,  $\tau$ , and the equilibrium krypton pressure,  $PP_{Kr,eq}$ .

we return to our idealized model from section 3.2.3 and attempt to incorporate a finite throughput into our equations. For simplicity, we will make the assumption that the pressure in the RGA volume responds instantaneously to the pressure in the cold trap volume ( $P_{Kr,CT}$ ), so at any moment,  $t$ ,  $PP_{Kr}(t) = P_{Kr,CT}(t)/180$ . We start by rebuilding the differential equation for  $P_{Kr,CT}(t)$  this time adding a term for entrainment:

$$V \frac{dP_{Kr,CT}}{dt} = \Phi Q_{Xe,CT}(t) - P_{Kr,CT}(t)/Z_1 - Q_{trap}(t), \quad (3.20)$$

where  $Q_{trap}(t)$  represents the rate at which krypton is becoming trapped in the xenon ice at a given time. In the constant flow, equilibrium limit we can write  $Q_{trap}$  in terms of  $\alpha$ :

$$P_{Kr,CT}/Z_1 = \Phi Q_{Xe,CT} - Q_{trap} = \alpha \Phi Q_{Xe,CT}, \quad (3.21)$$

which can be rewritten:

$$Q_{trap} = (1 - \alpha) \Phi Q_{Xe,CT} = \left(\frac{1}{\alpha} - 1\right) P_{Kr,CT}/Z_1. \quad (3.22)$$

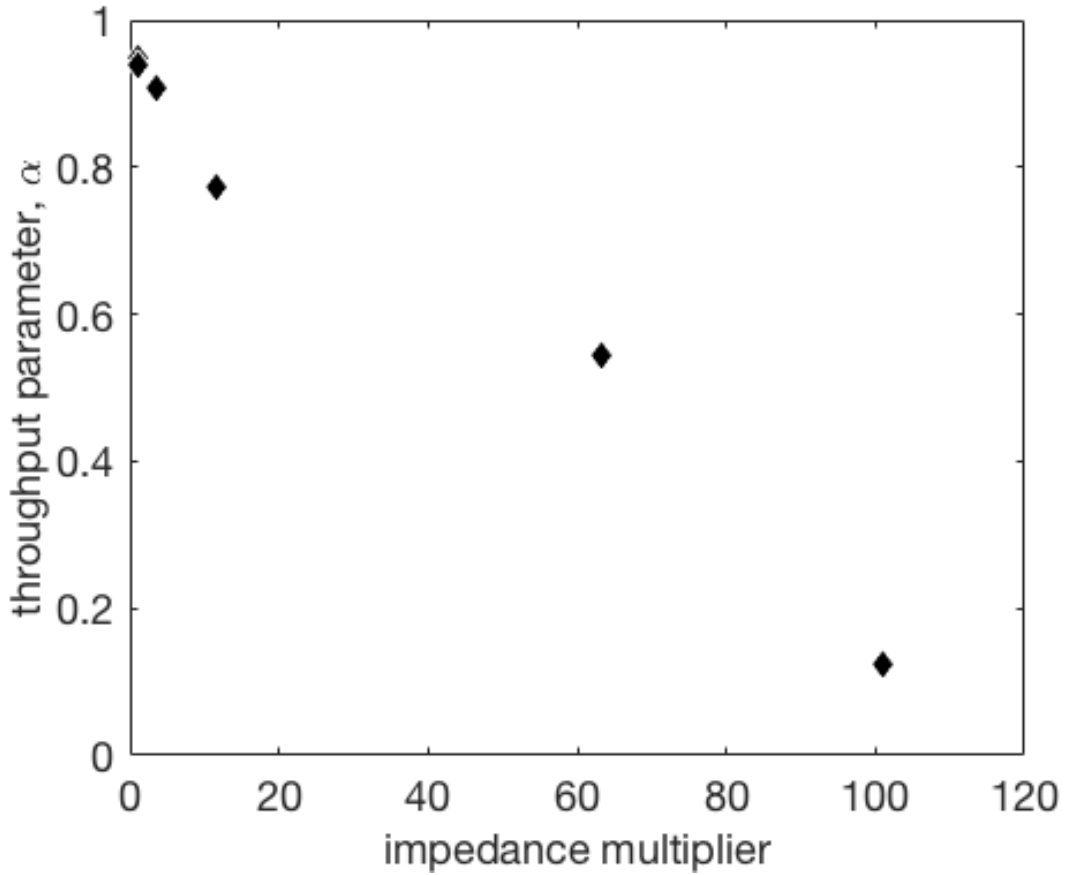


Figure 3.17: Left-over method of calculating  $\bar{\alpha}$ . The decreasing trend in the throughput indicates that error in the impedance measurements cannot fully explain the observed deviation from equation 3.19.

We do not know a priori how  $\alpha$  and  $Q_{trap}$  will behave in the non-equilibrium case. The simplest assumption to make is that  $\alpha$  remains constant over the full time range in which xenon is flowing. In this case the entrapment rate, entrapment rate takes the form of a virtual leak with constant volumetric pumping rate:

$$Q_{trap}(t) = S_{trap}P_{Kr,CT}(t), \quad (3.23)$$

where,

$$S_{trap} = \frac{1}{Z_1} \left( \frac{1}{\alpha} - 1 \right). \quad (3.24)$$

Rewriting equation 3.20 with this assumption we get a new exponential response equation for  $P_{Kr,CT}(t)$ :

$$V \frac{dP_{Kr,CT}}{dt} = \Phi Q_{Xe,CT}(t) - \left( \frac{1}{Z_1} + \frac{1}{Z_1} \left( \frac{1}{\alpha} - 1 \right) \right) P_{Kr,CT}(t) \quad (3.25)$$

$$= \Phi Q_{Xe,CT}(t) - \frac{1}{\alpha Z_1} P_{Kr,CT}(t) \quad (3.26)$$

After accounting for a constant throughput parameter, the overall response time constant of the cold trap will have a linear dependence on the throughput parameter:

$$\tau = \alpha Z_1 V. \quad (3.27)$$

This agrees with the linearity between  $\tau$  and  $PP_{Kr,eq}$  shown in figure 3.16. To make this explicit, we can use equation 3.27 to rewrite equation 3.10:

$$PP_{Kr,eq} = \frac{\tau}{180V} Q_{Xe,CT} \Phi_{Kr}. \quad (3.28)$$

A further assumption we could make is that  $S_{trap}$  does not have a dependence on  $Z_1$ . Under this assumption, we can begin to make predictions about how  $\alpha$  will behave as a function of impedance. Writing equation 3.25 in terms of  $S_{trap}$  gives:

$$V \frac{dP_{Kr,CT}}{dt} = \Phi Q_{Xe,CT}(t) - \left( \frac{1}{Z_1} + S_{trap} \right) P_{Kr,CT}(t), \quad (3.29)$$

which means:

$$\frac{1}{\tau} = \frac{1}{Z_1 V} + \frac{S_{trap}}{V} \quad (3.30)$$

$$\tau = V \frac{Z_1}{1 + Z_1 S_{trap}} \quad (3.31)$$

Another way to put this is that the overall response time is the inverse sum of the idealized output time constant, and the entrapment time constant:

$$\frac{1}{\tau} = \frac{1}{\tau_{out}} + \frac{1}{\tau_{trap}}, \quad (3.32)$$

where  $\tau_{out} = Z_1 V$  and  $\tau_{trap} = V / S_{trap}$ . Equation 3.32 indicates that when  $\tau_{out} \ll \tau_{trap}$  the cold trap response will have the idealized linear dependence on  $Z_1$ . However, in the limit  $\tau_{out} \gg \tau_{trap}$ , the response will approach a constant in  $Z_1$ .

Substituting equation 3.30 into equation 3.28, we get:

$$PP_{Kr,eq} = \frac{1}{180} Q_{Xe,CT} \Phi_{Kr} \frac{Z_1}{1 + S_{trap} Z_1}. \quad (3.33)$$

We fit this equation to the  $PP_{Kr,eq}$  data taken at various impedance settings. We approximate the corresponding  $Z_1$  values in the following way. We calculate  $Z_1$  at the 1x impedance setting using equation 3.27, where  $\tau$  is the best fit value to  $PP_{Kr}(t)$ , and  $\alpha$  is measured using the left-over method. The rest of the  $Z_1$  values are calculated by multiplying the 1x impedance value by the scaling factor measured in the adjustment of the xenon pressure described in section 3.2.2. For the 0.5 inch trap, we take  $V = 183.8$  cc. For the 1.5 inch trap, we did not measure the volume, so assume that  $Z_1$  at 1x impedance is the same for both traps.

The data for  $Z_1$  versus  $PP_{Kr,eq}$  fits reasonably well to equation 3.33. For the 0.5 inch

trap, the best fit  $S_{trap} = 0.89 \pm 0.12$  cc/s and  $\tau_{trap} = 207 \pm 30$  s. For the 1.5 inch trap,  $S_{trap} = 2.6 \pm 0.5$  cc/s and  $\tau_{trap} = 180 \pm 30$  s.

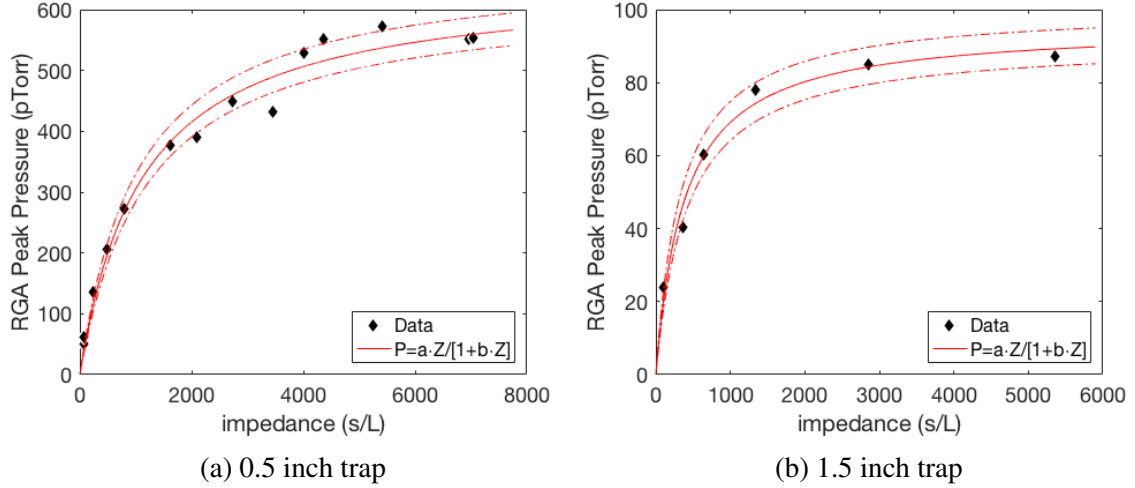


Figure 3.18: Equilibrium krypton pressure as a function of impedance. This fitting model is derived from the assumption that  $S_{trap}$  is independent of impedance. The data fits this model reasonably well.

### 3.3.5 Post Flow Behavior

To this point we have largely ignored the behavior of  $PP_{Kr}(t)$  after the xenon flow has been stopped, but this data contains interesting features that are worth investigating. The most obvious feature is the departure from the exponential decay expected from equation 3.19. In figure 3.15 we see that after the flow is turned off, the krypton pressure begins to drop much faster than the trend expected from the fit to the rising portion ( $\tau_{rise}$ ) but turns over and eventually levels off to an exponential trend with a significantly longer time constant than expected.

Our best explanation for the quickly falling transient behavior is that the volume of the cold trap becoming effectively larger when the flow is turned off. While a macroscopic amount of xenon is being flowed into the cold trap, the input side of the cold trap will not be in equilibrium with the output side. As mentioned previously, the input side of the cold

trap will be in viscous flow, while the output will be near vacuum. In this arrangement, the krypton pressure in the vacuum state ( $P_{Kr,CT}$ ) will be physically restricted from expanding past the ice-forming region, effectively reducing the volume of the cold trap. Once flow has stopped, this molecular-flow krypton will be allowed to expand into the full cold-trap volume, and in so doing, will lower  $P_{Kr,CT}$ . To confirm this effect, we conduct two trials with identical impedance, flow rate, and sample mass. In the first trial we use a 502cc, 0.5 inch diameter cold trap. In the second test, we add a 500cc stainless steel sample bottle to the output of the trap. Since the sample bottle is already in the vacuum state before the xenon flow is turned off, the volume difference should be much smaller, and therefore the transient drop should be much smaller.

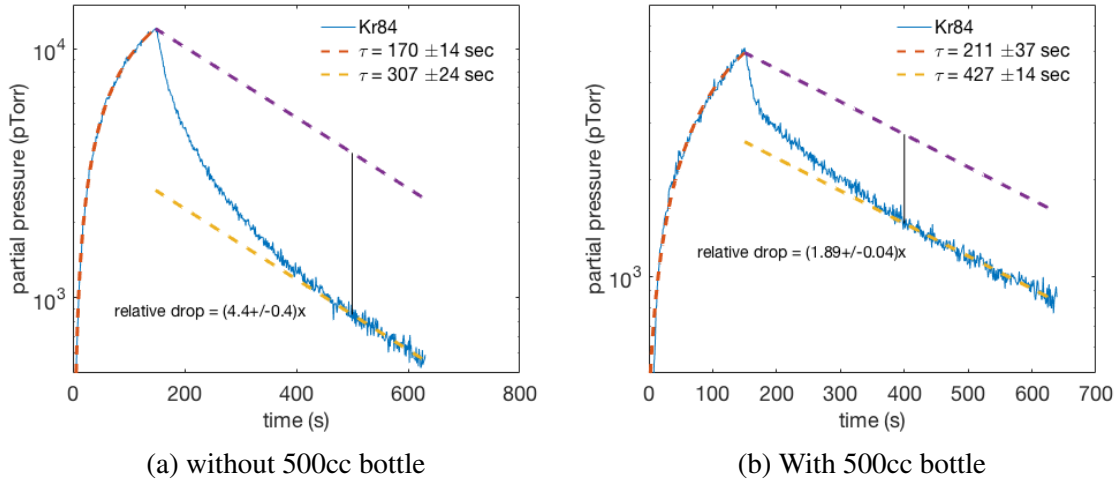


Figure 3.19: Trials with and without a 500cc sample bottle connected to the output of the cold trap. These runs were both done at 3SLM, and at 19x impedance.

After running these trials at 3SLM and 19x impedance, we find that when the 500cc bottle is attached,  $P_{Kr,CT}$  drops by  $(47 \pm 1)\%$  in the transient region. When the bottle is not connected, this drop is  $(77 \pm 2)\%$ . We calculate these drops by fitting an exponential decay to the region of  $P_{Kr,CT}(t)$  after it has leveled off from the transient region. We then take the difference between this trend and a trend with the same time constant which passes through

the last point of  $P_{Kr,CT}$  before the xenon flow was stopped. It should also be noted here that the rise time and fall time are both longer in the trial with the bottle attached, but not as much as might be expected from doubling the cold trap volume. In fact, the rise times are only about 1 standard deviation apart. It may be that the added impedance of the valve used to connect the bottle to the cold trap limits communication between the two volumes. Also, we ran these trials in the high xenon flow regime in which the ice formation region will move along the length of the cold trap over the course of the run. This should make the effective volume increase more pronounced but may obscure tests pertaining to the rise and fall time constants.

We also used the post flow region of the data to test whether or not there was diffusion occurring in the cold trap. We ran several tests in which we would close V6 in order to shut off the  $P/Z_1$  term in equation 3.25. In this way we hoped to measure the rate at which  $P_{Kr,CT}$  is reduced purely by diffusion into static xenon ice.

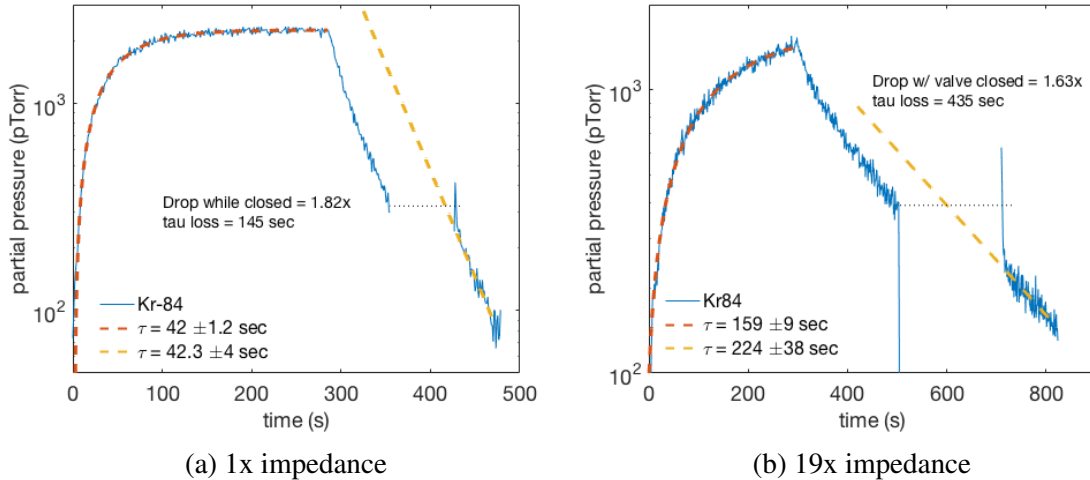


Figure 3.20: Trials at 1x and 19x impedance, each at 0.3 SLM. Each trial has a period of time during post-flow in which V6 was closed; a 70 second period in the 1x case and a 210 second period in the 19x case. In both trials, the fractional drop in pressure while V6 was closed was roughly the same. The post-flow transient drop was calculated to be  $(26 \pm 10)\%$  for the 1x impedance run and  $(34 \pm 8)\%$  for the 19x impedance run. The “tau loss” indicated on the plots are extrapolated time constants assuming the pressure drop with V6 closed is due to some exponential decay.

The results were somewhat ambiguous; we did find that the krypton pressure dropped while V6 was closed, but the fractional drop was on the order of about  $(1.7 \pm 0.2)$  regardless of the amount of time V6 was left closed ( $\Delta t$ ). This is more indicative of a separate issue having to do with the process of closing and reopening V6 than it is of diffusion. We would expect that more krypton would diffuse into the ice the longer it was left in this static state. We chose longer  $\Delta t$ 's to correspond to higher impedances. It is possible that there was an impedance-dependent diffusion which our choice of  $\Delta t$  happened to cancel out, however an impedance-dependent diffusion would disagree with the results from the previous section.

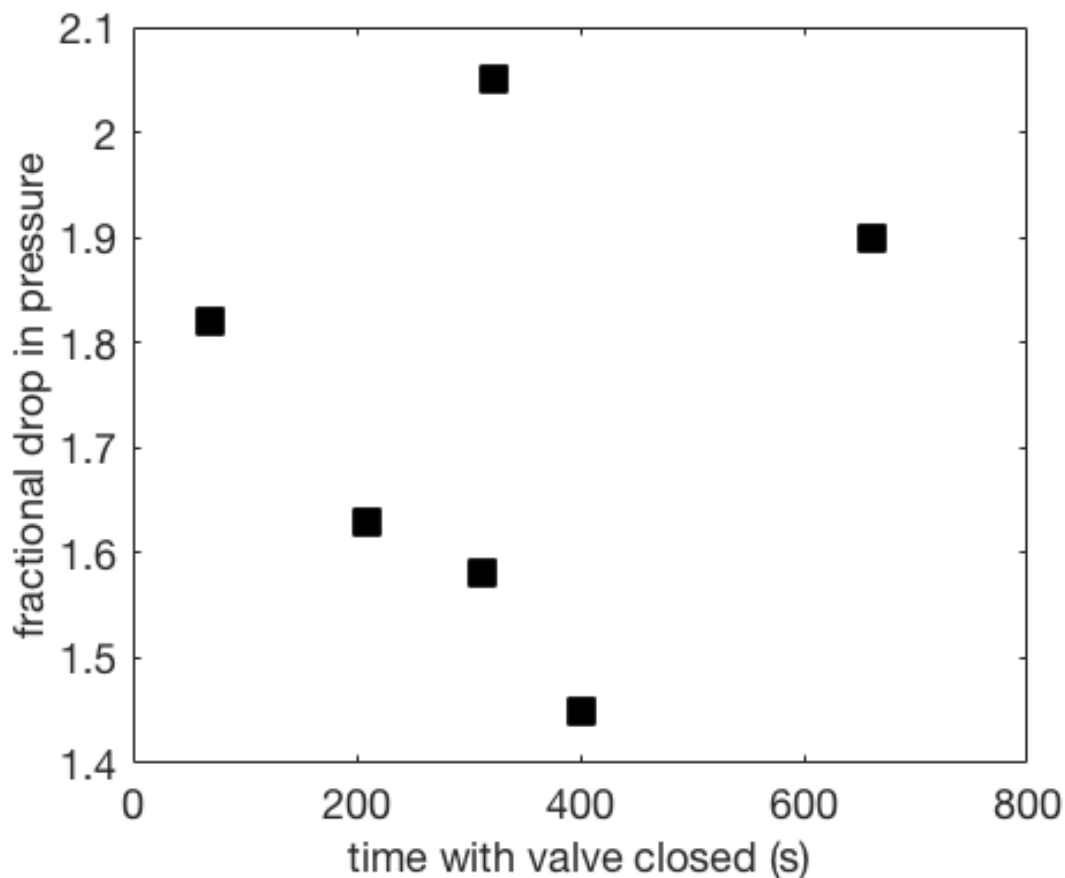


Figure 3.21: Lost krypton pressure as a function of the length of time with V6 closed. There does not seem to be a clear trend.

The question remains as to why the long term post-flow decay rate of  $P_{K,CT}(t)$  is so

much lower than the best-fit rate of the rising data. The obvious answer would be in  $\tau$ 's proportionality to the volume of the cold trap. If  $V$  sees an effective increase after the xenon flow is turned off, then  $\tau$  would see an increase of the same relative size. This matches the data from figure 3.20b in which the fractional increase in  $\tau$  is  $1.4 \pm 0.3$ , and the fractional increase in volume calculated from the post-flow transient drop in pressure is  $1.5 \pm 0.2$ .

There is still some tension with the data. First, we don't see a post-flow change in  $\tau$  in the 1x impedance plot (figure 3.20a) like we see in the 19x impedance plot. Also, we see no clear evidence of krypton entrapment occurring when the xenon flow has been turned off, leaving only entrainment-like effects. These should turn off in the post flow region, allowing  $\tau$  to approach its predicted value. In the case of figure 3.20b, the expected value is approximately  $1.4 \times 19 \times 42 \text{ sec} = 1120 \text{ sec}$  after accounting for the impedance factor and effective volume increase. Instead, we see no evidence of this turn-off at all.

### 3.3.6 Diffusion and Entrainment

In the previous sections we constructed a model where the krypton entrapment rate behaves in the manner of a constant volumetric pumping speed. This model provides a decent representation of the data, but we are left to ask what this model can tell us about the physical source of the entrapment. We have two postulations as to the source of krypton entrapment; diffusion and entrainment.

Diffusion is governed by two equations- Fick's two laws of diffusion. In one dimension, these are:

$$J = -\frac{d\phi}{dx} \quad (3.34)$$

$$\frac{\partial\phi}{\partial t} = D \frac{\partial^2\phi}{\partial x^2} \quad (3.35)$$

Here  $J$  is the amount of substance per unit area per unit time,  $D$  is the diffusion coefficient, and  $\phi$  is the concentration of krypton at a certain depth,  $x$ , and certain time,  $t$ . The boundary concentration at  $x = 0$  will be given by the pressure of krypton above the ice and the solubility constant,  $K$ :

$$\phi(0, t) = P_{Kr,CT}(t)K \quad (3.36)$$

We can then use equation 3.34 to write the entrapment rate of krypton due to diffusion:

$$Q_{diffusion}(t) = -AD\frac{d\phi}{dx}(x = 0, t), \quad (3.37)$$

where  $A$  is the surface are of xenon ice.

To get an idea for the time dependence of the diffusion rate, we'll consider the simplified case of a constant  $P_{Kr,CT}$  above a static sheet of unchanging thickness,  $L$ , and surface area,  $A$ . Diffusion in this scenario could fall into two regimes. for large values of  $D$ , the krypton will penetrate quickly, the ice will approach saturation, and the boundary conditions will be  $\phi(x > 0, t = 0) = 0$ ,  $\phi(x = 0, t) = P_{Kr,CT}K$ , and  $\frac{\partial\phi}{\partial x}(x = L, t) = 0$ . In this regime, equation 3.35 can be solved using a Fourier series of a rectangular wave with wavelength of  $4L$ , height of  $-P_{Kr,CT}K$ , and DC offset of  $P_{Kr,CT}K$ :

$$\phi(x, t = 0) = P_{Kr,CT}K[1 - \frac{4}{\pi} \sum_{n_{odd}} \frac{\sin(\frac{n\pi x}{2L})}{n}]. \quad (3.38)$$

After we feed this series through equation 3.35, we see that each term in the series will pick up a time dependence of  $e^{-(\frac{n\pi}{2L})^2 Dt}$ . This means that the higher order terms will quickly fall away leaving only the first order term remaining:

$$\phi(x, t \rightarrow \infty) = P_{Kr,CT}K[1 - \frac{4}{\pi} \sin(\frac{\pi x}{2L}) e^{-(\frac{\pi}{2L})^2 Dt}]. \quad (3.39)$$

In this limit, the krypton entrapment rate will be:

$$Q_{diffusion}(t) = P_{Kr,CT}K \frac{2AD}{L} e^{-(\frac{\pi}{2L})^2 Dt}. \quad (3.40)$$

The second regime of diffusion is if  $D$  is very small, and the krypton does not penetrate a significant distance into the ice. In this regime, the ice can be considered a semi-infinite line with boundary conditions,  $\phi(x = 0, t) = P_{Kr,CT}K$ ,  $\phi(x > 0, t = 0) = 0$ , and  $\phi(x \rightarrow \infty, t) = 0$ . This problem can be solved using Laplace transformation:[18]

$$\mathcal{L}\{f(x, t)\} \equiv \hat{f}(x, p) = \int_0^\infty e^{-pt} f(x, t) dt. \quad (3.41)$$

The transformation has the nice feature of leaving spacial derivatives unchanged, while transforming away time derivatives:

$$\mathcal{L}\left\{\frac{\partial f(x, t)}{\partial t}\right\} = \int_0^\infty e^{-pt} \frac{\partial f(x, t)}{\partial t} dt = p\hat{f}(x, p) - f(x, t = 0) \quad (3.42)$$

For the boundary conditions above, the transformation of equation 3.35 is:

$$p\hat{\phi} = D \frac{\partial^2 \hat{\phi}}{\partial x^2}, \quad (3.43)$$

the solution to which is:

$$\hat{\phi}(x, t) = c_1 e^{-x\sqrt{p/D}} + c_2 e^{x\sqrt{p/D}}. \quad (3.44)$$

In order to satisfy the boundary condition at infinity,  $c_2$  must be 0, and in order to satisfy

the boundary condition at  $x = 0$ , we know  $c_1 = P_{Kr,CT}K/p$ . This leaves:

$$\hat{\phi}(x, t) = \frac{P_{Kr,CT}K}{p} e^{-x\sqrt{p/D}}. \quad (3.45)$$

Transforming back to  $t$  space, we get:

$$\phi(x, t) = P_{Kr,CT}K[1 - erf(x/\sqrt{4Dt})]. \quad (3.46)$$

This means the entrapment rate of krypton in this diffusion regime will be:

$$Q_{diffusion}(t) = P_{Kr,CT}K\sqrt{\frac{D}{\pi t}}. \quad (3.47)$$

The krypton entrapment rate in both of these regimes is proportional to  $P_{Kr,CT}$ , and so could be written as  $Q_{diffusion}(t) = S_{diffusion}P_{Kr,CT}$ . However, in both cases the volumetric pumping speed,  $S_{diffusion}$ , would have a time dependence, which goes against our model from the previous section, and so would seem not to fit the data.

We have less of a grasp on how we expect entrainment will behave, however we can create a simple toy model where the entrainment rate is proportional to the xenon flow rate and the pressure of krypton present in the trap:

$$Q_{entrainment} = \beta P_{Kr,CT} Q_{Xe,CT}, \quad (3.48)$$

where  $\beta$  is some constant of proportionality. Under this model we can rewrite equation 3.20:

$$V \frac{dP_{Kr,CT}}{dt} = \Phi Q_{Xe,CT}(t) - P_{Kr,CT}(t)/Z_1 - \beta P_{Kr,CT}(t) Q_{Xe,CT}(t). \quad (3.49)$$

In the equilibrium region, this would give:

$$P_{Kr,CT} = \frac{\Phi Q_{Xe,CT}}{1/Z_1 + \beta Q_{Xe,CT}}, \quad (3.50)$$

or:

$$PP_{Kr,eq} = \frac{Z_1}{180} Q_{Xe,CT} \Phi \frac{1}{1 + \beta Z_1 Q_{Xe,CT}}. \quad (3.51)$$

Comparing this to equation 3.10 we see that in this model,  $\alpha = 1/[1 + \beta Z_1 Q_{Xe,CT}]$ . Equation 3.51 has the same impedance dependence as equation 3.33, however figure 3.14 shows that  $\alpha$  does not have a dependence on xenon flow rate.

Again we are left with a dearth of satisfying explanations. Neither our predictions for the behavior of diffusion or entrainment flesh out in the data.

### 3.3.7 Model Overview

The formation of xenon ice is a complicated process, and its interaction with a time-dependent krypton pressure is likely even more so. It is perhaps unreasonable to expect such overly simplified models as we have posed thus far would suffice in describing this process adequately. That being said, in this section, we have developed some toy models that are able to predict the system's behavior to some extent. The two most important takeaways are in how the krypton RGA pressure responds to system impedance and xenon flow rate. Above about 2 SLM flow rate, the xenon ice begins to form past the first bend in the cold trap plumbing. When this happens,  $PP_{Kr}(t)$  begins to drop off of its ideal trend.

The  $PP_{Kr}(t)$  has a monotonically increasing response to increases in  $Z_1$ , although it begins to asymptote to a constant value above roughly 100x impedance. Practical considerations will likely win out at high impedances, making the optimal setting at somewhere less than 100x. The exponential response time constant of the cold trap also asymptotes to

a constant, so as the impedance is increased to be much greater than 100x, the characteristic response time of the RGA volume will likely begin to compete.

There is very little we can say about what is physically happening inside the cold trap the causes krypton to become trapped in the xenon ice. The overall effect seems to mimmic a leak with a constant volumetric flow rate,  $S_{trap}$  that is independent of both flow rate and impedance. We have found no evidence that diffusion of krypton into the ice plays a major role, and all of our test point to some effect that is dependent on active xenon flow, but whose rate is not affected by changes to the xenon flow rate.

### 3.4 Analysis Scheme

The physical value we are interested in measuring is the concentration of an impurity, specifically krypton, in a sample of xenon gas. This value is typically referred to as  $\Phi$  and cited in units of grams of krypton per gram of xenon. The calculation of  $\Phi$  is done using the RGA partial pressure data collected between steps 3 and 7 of the procedure outlined in section 3.1.2. An example of this data is shown in figure 3.22.

There are four distinct time-intervals in figure 3.22 labelled I through IV.

- I is the period of time after ice has been formed (step 3), but before the xenon flow has been started (step 5). During this interval, both xenon and krypton traces should be constant; if they are trending or otherwise varying systematically, there is some problem that needs to be addressed before continuing. The average krypton pressure over this interval is used as the baseline value and will be subtracted from the analysis pressure. The average xenon pressure can be used as a measure of the RGA gain, since the physical xenon pressure will not change between sample analyses.
- II is the period of time after xenon flow has been started (step 5), but before the krypton pressure has reached its equilibrium value. Given a long enough cold trap the

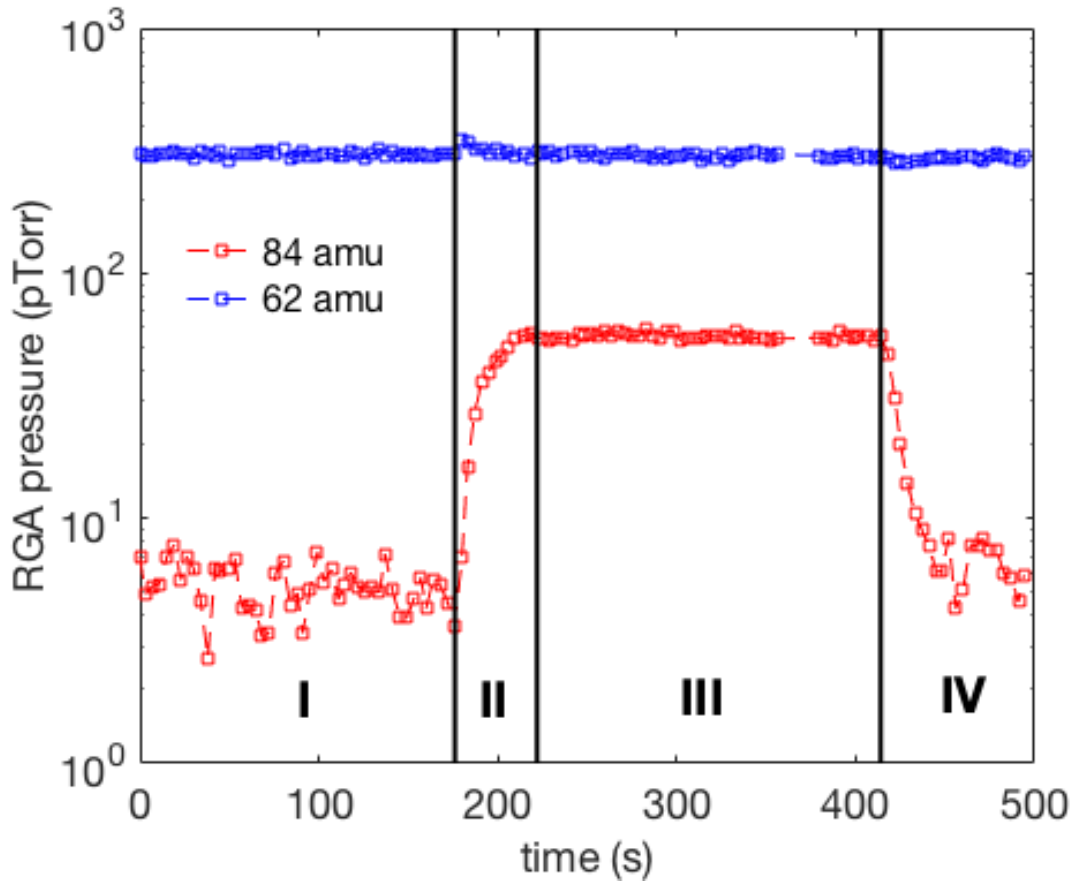


Figure 3.22: The RGA-measured partial pressures of the 84 amu krypton peak and doubly ionized Xe-124 which appears as a peak at 62 amu. The four time intervals indicate: static baseline, rising Kr trace, steady-state Kr pressure, and post-flow Kr pressure fall.

krypton pressure during this step would fit a 1-exponential model, but the geometry of the cold trap can cause kinks in the trace. It is common for there to be a small transient effect in the xenon pressure as is seen here. This is likely due to the ice temperature increasing due to the added heat load from the flowing xenon. This transient effect can illicit an electronic response in the RGA baseline pressure which will mimmic a small krypton signal. The mitigation of this effect will be described in a later section.

- III is the period of time during which the krypton pressure is at its equilibrium value.

This equilibrium pressure is determined by the flow rate of the xenon, the sensitivity of the system, and  $\Phi$ .

- IV is the period of time after the xenon flow has been stopped (step 6). During this period the krypton pressure will fall away exponentially before it eventually returns to the baseline value.

When the flow of krypton has equilibrated throughout the system,  $\Phi$  can be related to the flow rate and RGA krypton partial pressure through the following equation:

$$\Phi = \frac{PP_{Kr}}{CQ_{Xe,CT}}, \quad (3.52)$$

where  $C$  is a calibration constant which encapsulates the sensitivity of the system,  $Q_{Xe,CT}$  is the instantaneous flow rate of xenon into the cold trap, and  $PP_{Kr}$  is the krypton pressure. It is possible that there is a physical background seen by the RGA at the mass of interest (84 amu for the case of krypton), but we are only interested in the pressure which is extracted from the xenon sample. To account for any non-zero baseline we subtract out  $\bar{PP}_{Kr,0}$ , the average krypton pressure measured by the RGA during region I.

When paired with a concurrent flow-rate measurement,  $Q_{Xe,i}$ , each RGA data point,  $PP_{Kr,i}$ , collected in region III will give an individual measurement of the purity of the xenon sample,  $\phi_i$ :

$$\phi_i = \frac{1}{C} \frac{PP_{Kr,i} - \bar{PP}_{Kr,0}}{Q_{Xe,i}}. \quad (3.53)$$

We take the average of these individual purity measurements as the final result of the analysis:

$$\Phi = \overline{\phi_i}, \quad (3.54)$$

with  $N$  being the number of RGA data points collected in region III. The random uncer-

tainty on this purity result is taken to be the standard error:

$$\sigma_\Phi = \frac{\sigma_\phi}{\sqrt{N}}, \quad (3.55)$$

where  $\sigma_\phi$  is the standard deviation of the collection of  $\phi_i$ 's. This method of analysis has been previously shown to be linear with purity. [22, 24, 42]

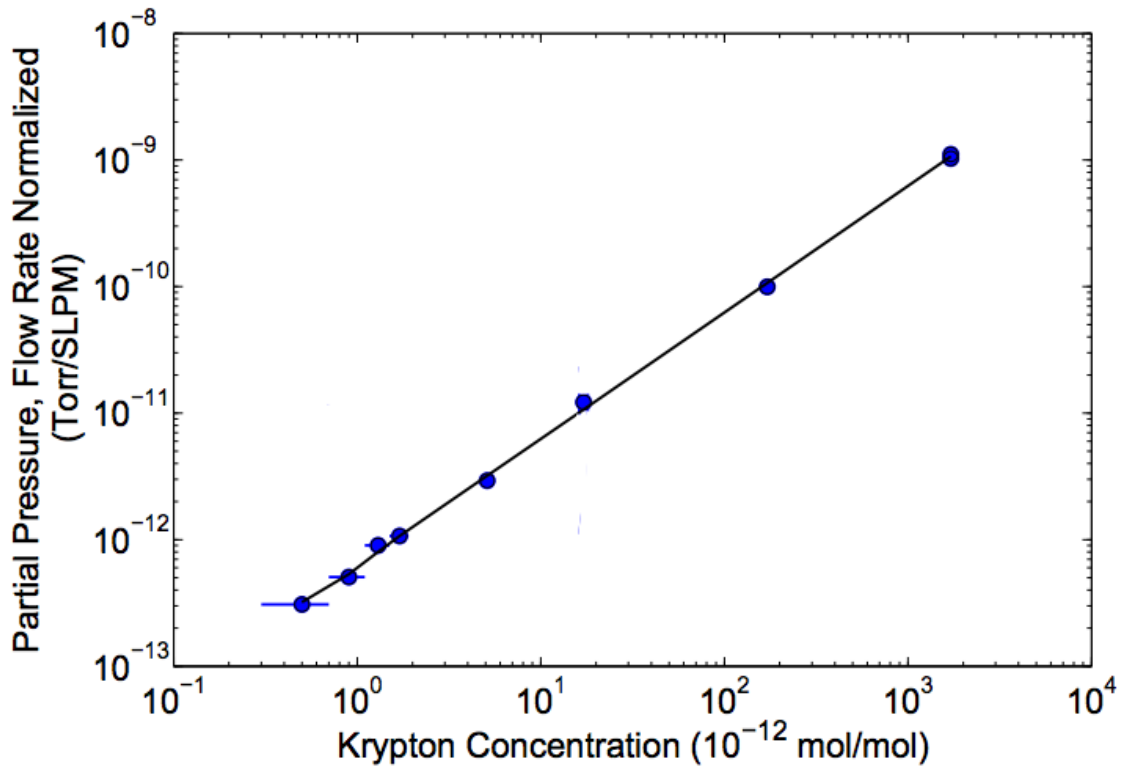


Figure 3.23: The linearity of the averaging analysis method. The slope of this line will be equal to the calibration constant,  $C$ .[24]

In order to maximize the krypton sensitivity, we operate in a high-impedance mode (described in later sections) which increases the rise and fall time of the krypton pressure. This being the case, we wish to allow  $PP_{Kr,i}$  to be drawn from the non-equilibrium regions II and IV, as well as region III. This In these cases we assume a more general version of

equation 3.52:

$$PP_{Kr}(t) = C\Phi f_Q(t), \quad (3.56)$$

where  $f_Q(t)$  is some function which defines the shape of the krypton pressure trace, given a specific flow rate profile,  $Q_{Xe,CT}(t)$ .  $\Phi f_Q(t)$  represents the flow of krypton out of the cold trap,  $Q_{Kr,RGA}(t)$ , and can be thought of as the input krypton flow,  $Q_{Kr,CT} = \Phi Q_{Xe,CT}$ , modified by the response of the system. Equation 3.56 will be valid as long as the response is linear with concentration. For example, consider the krypton trace shown in figure 3.22. The flow rate profile for this trace is:

In section 3.2 we find that an ideal system is expected to have an exponential response to flow. Convolving equation 3.16 with an exponential response yields the following shape function

$$f_Q(t) = Q_0 \begin{cases} 0 & \text{for } t \text{ in region I} \\ 1 - \exp(-\frac{t-t_1}{\tau}) & \text{for } t \text{ in region II or III} \\ \exp(-\frac{t-t_2}{\tau}) & \text{for } t \text{ in region IV} \end{cases} \quad (3.57)$$

Fitting this shape function to the data in figure 3.22 gives  $\tau = 11.6$  seconds. It should be noted here that the pressure trace shown in figure 3.24a does not fit this shape. This is because the response of the system to flow becomes non-linear at high flow rate and high impedances. Figure 3.24b shows that response does remain linear in concentration even when it is not linear in flow.

We now integrate equation 3.56 between some  $t_1$  and  $t_2$ :

$$\int_{t_1}^{t_2} PP_{Kr} dt = \Phi F_{Q,t_1,t_2}, \quad (3.58)$$

where:

$$F_{Q,t_1,t_2} \equiv \int_{t_1}^{t_2} f_Q(t) dt. \quad (3.59)$$

In terms of the discrete RGA measurements,  $PP_{Kr,i}$  this becomes:

$$\Phi = \frac{1}{F_{Q,t_1,t_2}C} \sum_{i=1}^N (PP_{Kr,i} - \bar{PP}_{Kr,0}) \Delta t_i. \quad (3.60)$$

$F_{Q,t_1,t_2}C$  is a constant of proportionality which can be measured by analyzing a xenon sample with a known  $\Phi$ . However, this constant will only hold so long as  $Q_{Xe,CT}(t)$ ,  $t_1$ , and  $t_2$  are identical between the analysis and calibration runs. To ensure consistency, it is best practice to calibrate after every sample analysis. These calibrations should follow the procedure described in section ?? and should use the left-over sample xenon which is recovered from the cold trap as the base “clean” xenon. This can be done as long as the initial concentration of krypton in the xenon sample is much less than the target concentration of the calibration xenon.

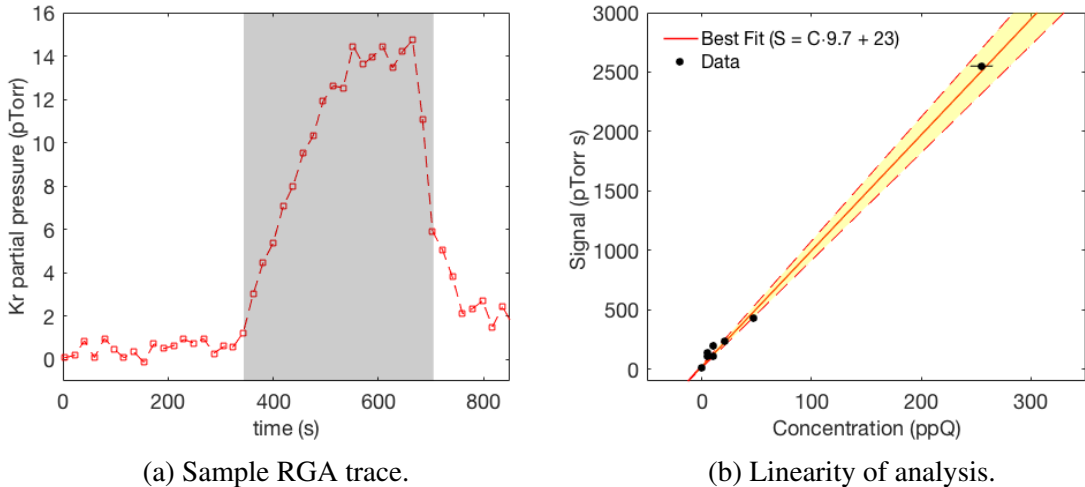


Figure 3.24: Linearity of the integration-style analysis described in equation 3.60. The krypton signals used in these measurements never reached an equilibrium value. The xenon flow profile for these measurements was a square pulse. The height of this pulse was set using an MFC, and the time-width of the pulse was defined by the size of the xenon sample used.  $t_1$  was defined as the start of the xenon flow, plus 20 seconds, and  $t_2$  was defined as the stop of the xenon flow, plus 20 seconds.

The random uncertainty of purity results calculated using equation 3.60 are harder to

estimate than those calculated using equation 3.54. The fluctuations around each datapoint cannot be measured directly, so they are estimated using the baseline data collected in region I. The fluctuations of the RGA tend to increase at higher partial pressure, as shown in figure 3.25. We take the baseline fluctuations,  $\sigma_0$ , to be equal to the standard deviation of the region I data points. The random uncertainty of each data point,  $PP_{Kr,i}$ , is then taken to be:

$$\sigma_i = \sigma_0 * (1 + 0.009 * PP_{Kr,i}). \quad (3.61)$$

The propagation of this error to  $\Phi$  is then:

$$\sigma_\Phi^2 = \frac{1}{F_{Q,t_1,t_2}^2 C^2} \sum_{i=1}^N (\sigma_i^2 + \sigma_0^2/N_B) \Delta t_i^2, \quad (3.62)$$

where  $N_B$  is the number of data points used in the calculation of  $\overline{PP}_{Kr,0}$  and  $\sigma_0$ .

## 3.5 System Parameters and Optimization

Optimizing a cold-trap sampling system is a matter of maximizing the signal to noise ratio, which comes down to minimizing the fluctuations in the RGA baseline and maximizing the system response to krypton. There are several knobs and dials to turn to achieve this, but adjusting one of the knobs might change how one of the dials affects the sensitivity. This section will attempt to catalog the affect of these adjustments in an empirical way and will describe the optimal arrangement.

### 3.5.1 RGA Parameters

The first and simplest adjustments to be made are to the RGA electronics. These adjustments can be made quickly and easily, and are largely independent from the other knobs and dials. There is a long list of internal RGA parameters which should be understood

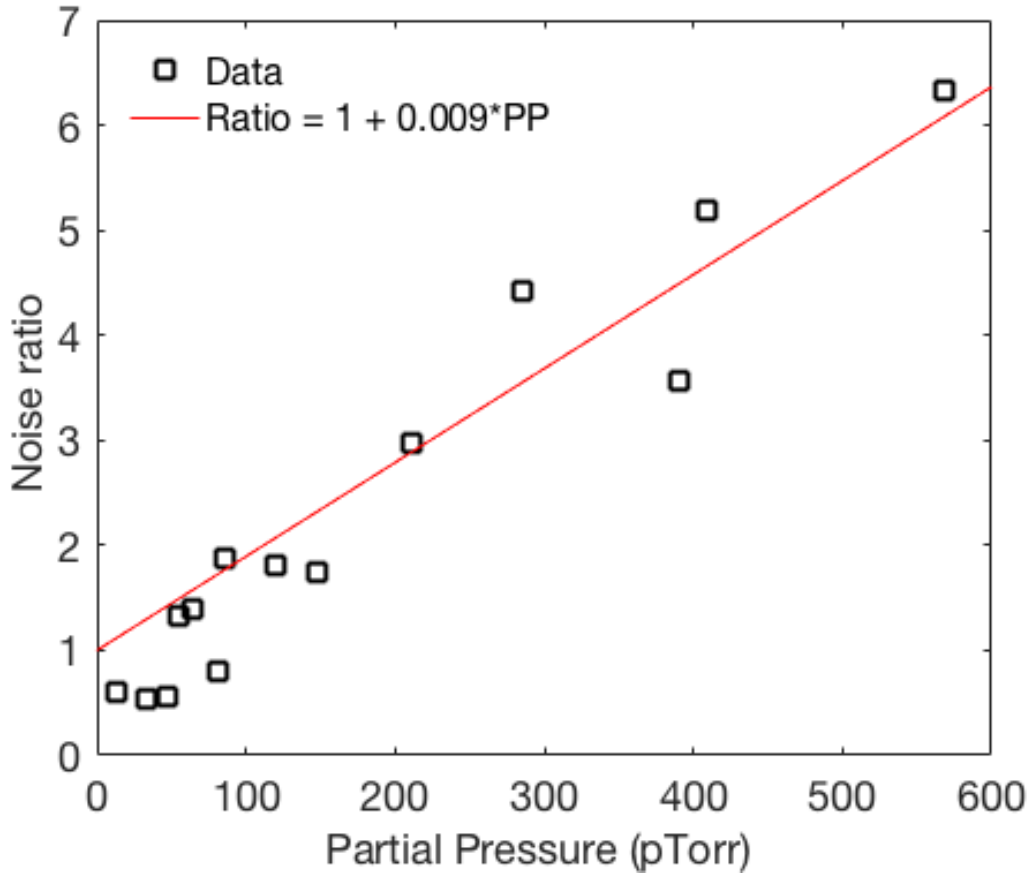


Figure 3.25: The trend in RGA fluctuations as a function of partial pressure. The noise ratio is defined as the fraction by which the RGA fluctuations increase when the partial pressure is increased from its baseline value ( $\text{Noise ratio} \equiv \sigma(\text{PP})/\sigma(\text{baseline})$ ).

before operating a cold trap system. These can be found in chapter 6 of the RGA manual. The two parameters that have the greatest effect on the sensitivity to krypton are the noise floor and the high-voltage setting of the continuous dynode electron multiplier (CDEM).

The noise floor sets the scan speed of the RGA; the lower the noise floor setting, the longer the RGA will spend integrating current on a single mass point. The practical effects are threefold. The obvious first implication is that with a low noise floor, it will take much longer to collect a single data point. At a noise floor setting of 0 the RGA will sit on a mass point for more than 5 seconds, and at a noise floor setting of 3 it will sit for less than

0.5 seconds per mass. For high-sensitivity analysis, it is better to have the noise floor set as low as possible, which will give you fewer data points which have a smaller variance. This will reduce the amount of time spent communicating with the RGA, as well as the amount of down time between communications.

At higher noise floors, there tends to be an offset in the baseline. While we usually try to account for this by using baseline-subtracted pressures in purity calculations, it is possible that the shifted baseline is not additive to the pressure signal. This is indicated by the krypton signal in the LUX run04 data decreasing artificially. There is also evidence from the SLAC system that the baseline is not strictly additive to a physical pressure signal.

Setting the voltage on the CDEM is a balancing act. Increasing the voltage increased the signal amplification. Above a certain CDEM voltage, however, the random fluctuations in the RGA baseline rise faster than the gain, and if the voltage is set too high, the xenon ice vapor pressure will begin saturate the CDEM, degrading and possibly damaging it. The CDEM voltage should be high enough that the largest xenon peaks such as 132 and 133 should be at saturation but not so high that the doubly ionized peaks such as 66 amu saturate.

The health of the CDEM can be tracked using one of the xenon ice peaks, assuming the MG and SP parameters are not changed. MG is the CDEM gain factor and SP is the mass sensitivity factor used to convert the RGA current to partial pressure. The physical values may change over time, but the parameter stored in the RGA memory will not change unless a head-calibration is run. In particular, as the CDEM degrades, the gain will fall. A drift in the gain will be seen most easily as a drop in the measured xenon ice pressure. Since the vapor pressure of xenon ice at 77 Kelvin is physically constant, if this pressure reading drops, it indicates that the gain has dropped. To maintain the CDEM gain, the xenon peak at 62 amu should be monitored. Whenever this value drops, the voltage should be increased until the pressure returns to its initial value.

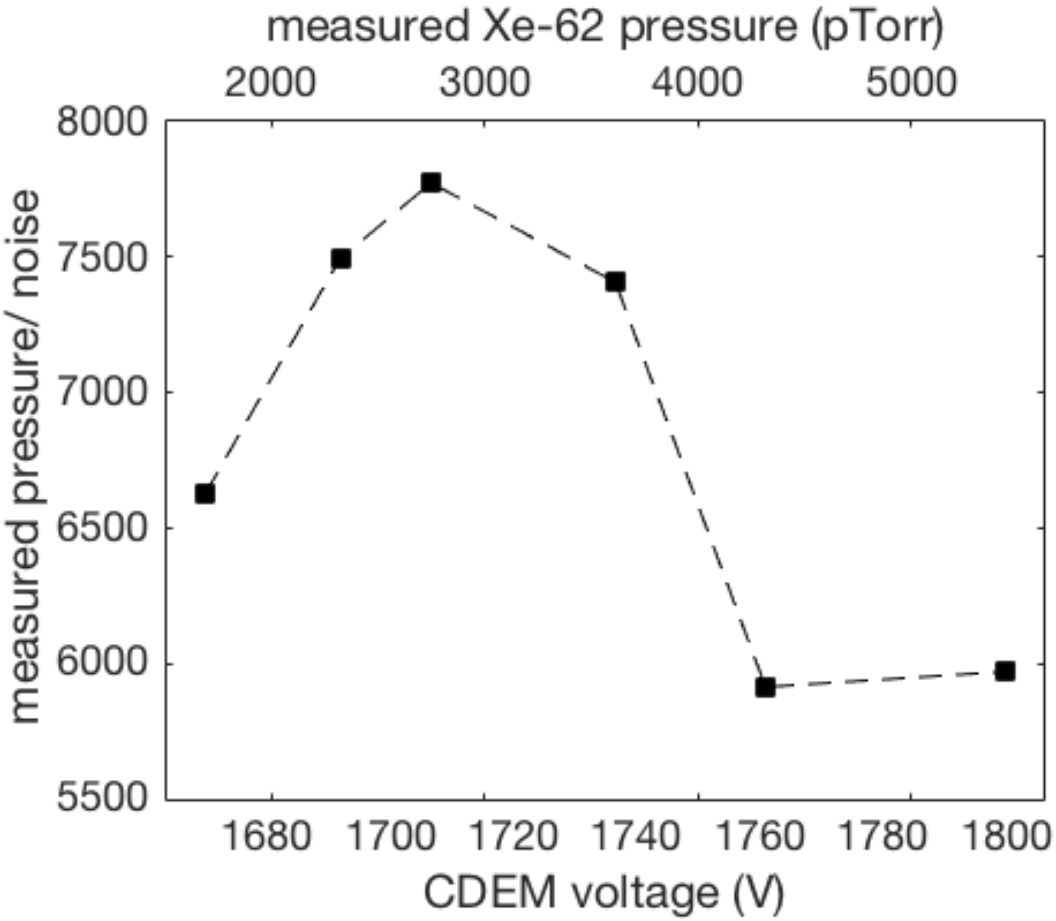


Figure 3.26: RGA sensitivity as a function of CDEM voltage.

### 3.5.2 Impedance and Flow Rate Settings

Consider the idealized pressure trace shown in figure 3.12, which is the result of a rectangular flow rate profile into a system which has an instantaneous response. The flat top of this trace will have a height given by equation 3.10:

$$PP_{Kr,eq} = \frac{\alpha}{180} Z_1 Q_{Xe,CT} \Phi_{Kr}. \quad (3.63)$$

The width of this pulse will be given by the amount of xenon used in the analysis ( $V_{SB} \Delta P_{Xe,SB}$ ) divided by the flow rate of the xenon into the cold trap  $Q_{Xe,CT}$ . Assume  $N$  is the number of

data points included in the analysis. Using a constant RGA sampling rate of  $r$  we find:

$$N = \frac{rV_{SB}\Delta P_{Xe,SB}}{Q_{Xe,CT}}. \quad (3.64)$$

By increasing the flow, we get something of a tradeoff. The pressure which we are trying to measure will increase proportionally to  $Q_{Xe,CT}$ . However the number of data-points in our analysis will also decrease proportionally to  $Q_{Xe,CT}$ , thereby increasing the uncertainty. Since uncertainty only has a dependence on  $\sqrt{N}$ , we will end up winning in signal-to-noise ratio, which will increase proportional to  $\sqrt{Q_{Xe,CT}}$ .

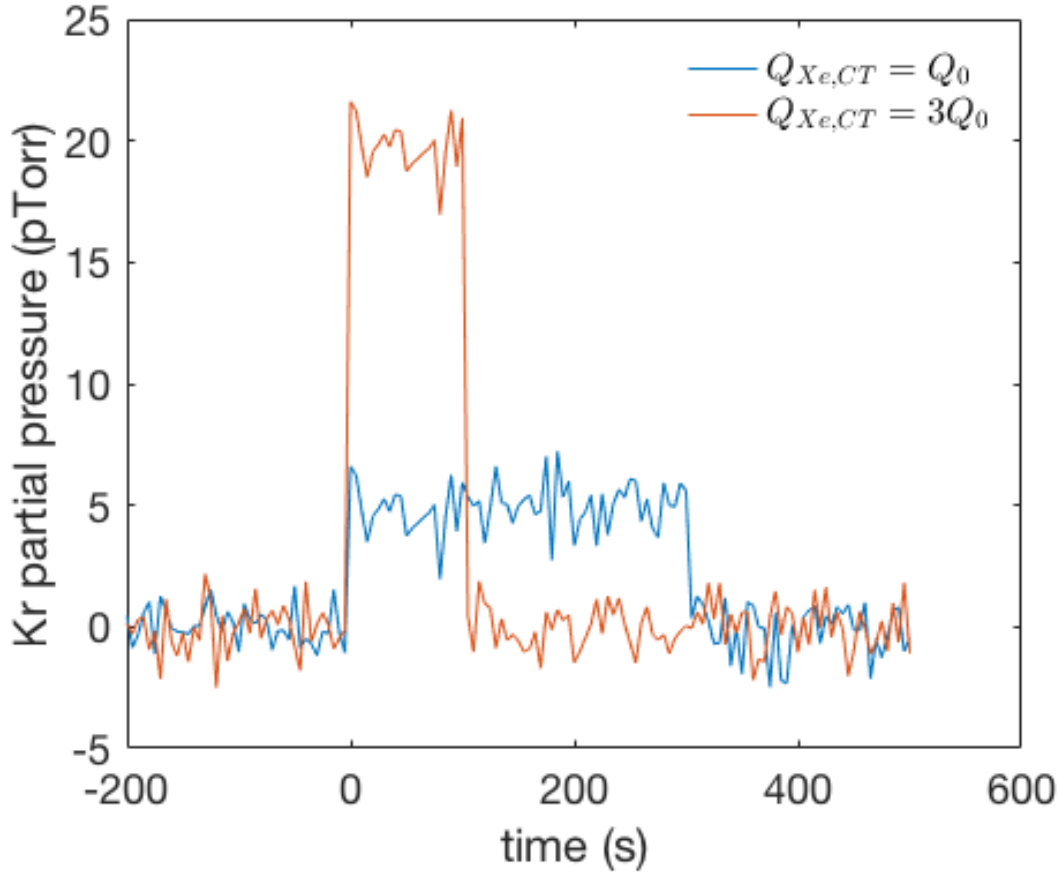


Figure 3.27: Peak krypton RGA pressure as a function of flow rate.

The dependence of our idealized signal-to-noise on  $\sqrt{Q_{Xe,CT}}$  argues for the use of as

high a xenon flow rate as possible. Unfortunately, we don't live in an ideal world, and there are forces conspiring against us in the high-flow limit. In section 3.3.3 we saw that at flow rates above about 2 SLM, the krypton throughput begins to fall. This effect will compete with, and may even overwhelm the statistical benefit we get from increasing the flow rate.

We are in a similar situation with our impedance setting. We have shown in section 3.3.4 that it is possible to amplify  $PP_{Kr}$  by modifying the impedances of IV1 and IV2. Figure 3.28 show a krypton signal which is nearly buried in electronic RGA noise can be increased more than ten-fold by adjusting the impedances. This amplification is not perfect, and comes at the cost of longer rise times and decreased krypton throughput. Even with these competing effects, the krypton equilibrium pressure remains monotonically increasing in  $Z_1$  as far as we have been able to measure.

To this point we have not yet developed a fully armed and operational model as to the physical chemistry governing the freezing of the xenon and the flow of xenon. The toy models we have developed provide some useful insights as to how to optimize the system, but significant tension with the data. In order to find the optimal settings for our cold trap system we turn instead to brute-force, empirical methods. We conduct a series of analysis-style runs at varying impedances and flow rates. The analysis procedure is standardized such that the only variables remaining are impedance and flow rate. The krypton concentration, RGA setting, and even ice-kernel formation procedure is identical for all the tests in the series. We choose an impedance setting and then scan through a series of flow rates. Once we are satisfied that we have located the optimal flow rate for that impedance, we move on to the next impedance setting.

For each setting, we conduct an integration-style analysis on the  $PP_{Kr}(t)$  data to get an

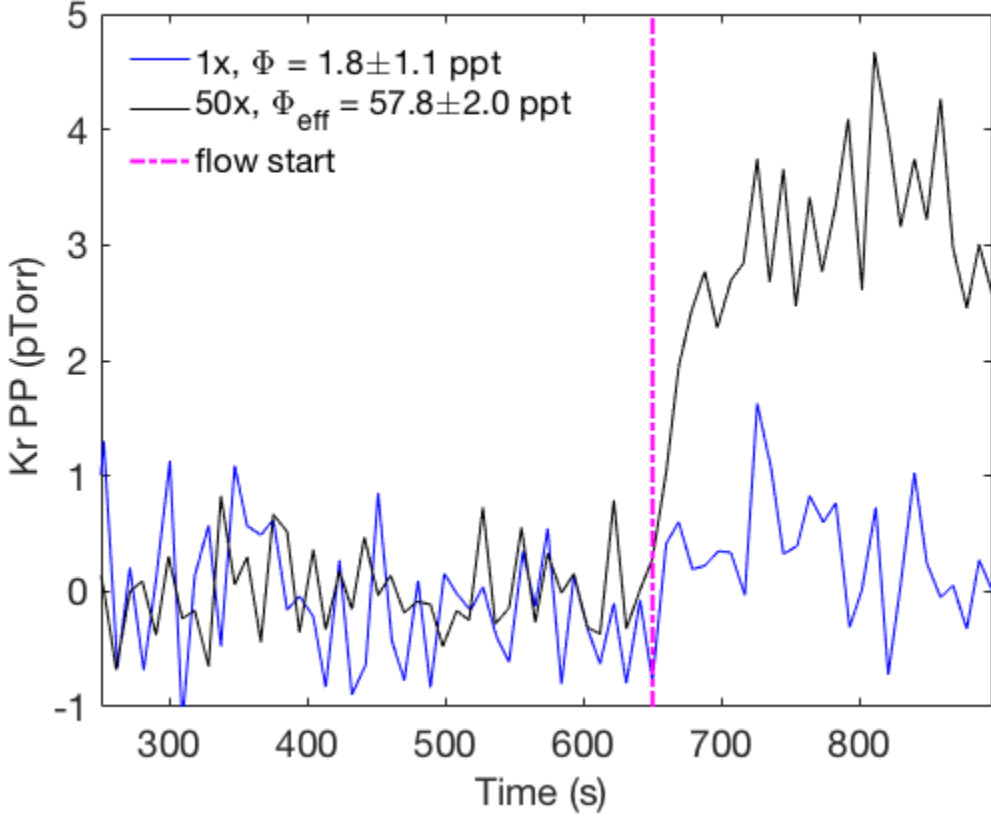


Figure 3.28: Amplification of krypton signal by increasing the impedance settings to the 50x state. Identical flow rates and xenon samples were used with the only difference being the impedance settings.  $\Phi$  is the measured krypton concentration in the 1x impedance setting and corresponding calibration.  $\Phi_{eff}$  is the equivalent measurement in the 50x state, using the 1x calibration number.

integrated pressure signal:

$$X_{Z,Q} = \sum_{i=1}^N (PP_{Kr,i} - \overline{PP_{Kr,0}}) \Delta t_i, \quad (3.65)$$

along with its corresponding uncertainty,  $\sigma_{Z,Q}$ . We use the  $X_{Z,Q}$ 's and  $\sigma_{Z,Q}$ 's to extrapolate a sensitivity, ( $\phi_{sens}(Z, Q)$ ) for each setting:

$$\phi_{sens}(Z, Q) = \Phi_{sample} \frac{\sigma_{Z,Q}}{X_{Z,Q}}, \quad (3.66)$$

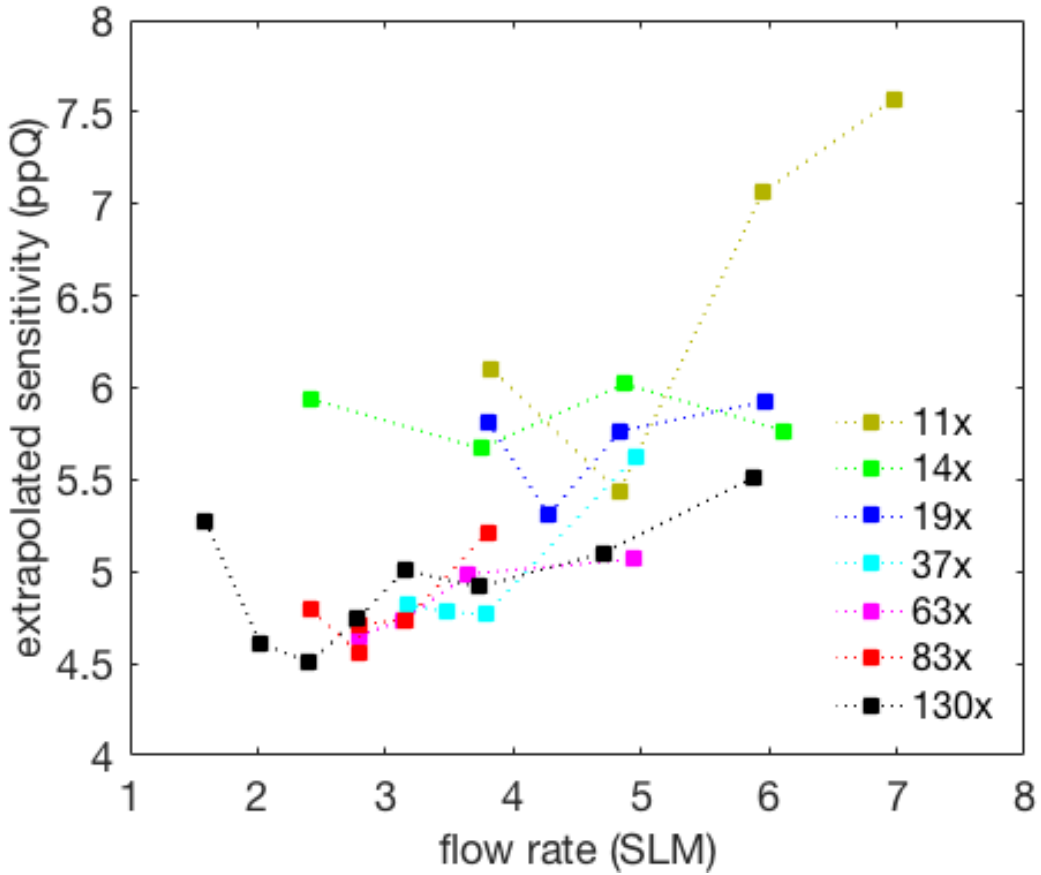


Figure 3.29: Scan across impedance and flow rate setting in search of the optimal settings.

where  $\Phi_{sample}$  is the known concentration of the xenon sample.

The minimum extrapolated sensitivity we measured during this scan was 4.5 ppQ, at 130x impedance and a flow rate of 2.4 SLM. Past about 30x impedance, the we find only a small benefit in increasing the impedance. The benefit of going from 37x impedance to 130x impedance is only about a 6% drop in extrapolated sensitivity, whereas the benefit to going from 11x to 37x is a 22% drop. Additionally, the optimal settings are all in the high xenon flow regime, but the high-impedance optimizations are near the transition point. The optimal flow for the 130x impedance is only 2.5 SLM, putting it essentially on the transition point between high and low flow regimes.

For the purposes of our final system optimization, we want to set the impedance as high as possible but will not go to the full 130x for reasons of practicality. With higher set points, the impedance becomes increasingly difficult to set repeatably. This, combined with the marginal impedance dependence above the 30x set-point leads us to aim for an impedance set-point of 90x. The optimal flow rate at this impedance is between 2.5 and 3 SLM, so we use 2.5 SLM as our MFC set-point.

### 3.6 Preparation of Calibration Xenon

Once the system has been optimized using a largely arbitrary mixture of xenon and krypton, the next key step is to measure the response of the system to a series of mixtures referred to as calibration xenon which have well known concentrations of krypton. Once this response is known, the system can be used to measure concentrations of unknown mixtures. To this end, the preparation of a mixture of xenon and krypton with a well known concentration is essential.

The first ingredient in the preparation of this mixture is extremely pure xenon. This is obtained by using the cold trap system itself to clean a small amount of stock xenon. As was explained previously, the cold trap analysis works because all but a microscopic amount of xenon is retained by the cold trap, while gasses such as krypton pass through largely unaffected. This means that the xenon that remains in the cold trap after an analysis has significantly lower krypton content than before the analysis. Depending on the system parameters, the post-run xenon will contain as little as 1/15<sup>th</sup> the krypton as the pre-run xenon. Using the system described by figure 3.32, it takes about 3 hours to purify 100g of typical stock xenon with a concentration of 1 part in  $10^9$  down to < 1 part in  $10^{15}$ ,

Once the xenon has been cleaned it is transferred to an appropriate mixing system, described by figure 3.30. The relative volumes of this system must be extremely well

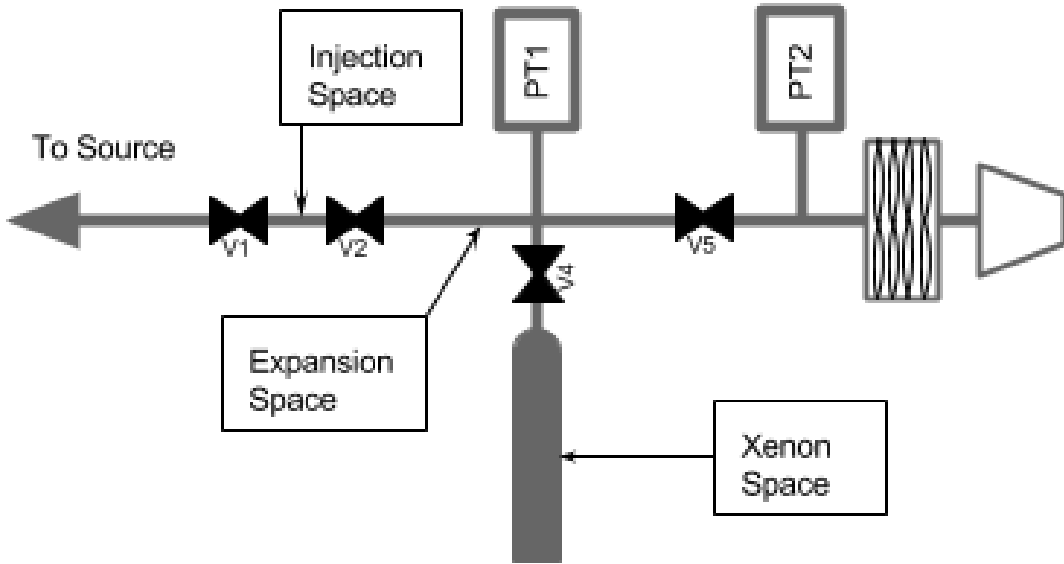


Figure 3.30: Plumbing diagram of a generalized mixing system.

known, so they are measured using volume sharing. First the full system, including injection, expansion, and xenon spaces, is filled with roughly 2000 torr of xenon as measured by pressure transducer 1. Then the expansion space is pumped to vacuum, leaving a well known pressure in both the injection and xenon spaces. Valve 4 is opened to expose the gas within the xenon space to the expansion space. The resulting pressure on PT1 gives the volume of the expansion space relative to the xenon space. Through the ideal gas law, when temperature is constant and mass is conserved, pressure times volume will remain constant:

$$P_1 V_{Xe} = P_2 (V_{Xe} + V_{inj}) \quad (3.67)$$

Therefore, the volume of the expansion space relative to the xenon space can be calculated using:

$$\frac{V_{inj}}{V_{Xe}} = \frac{P_1 - P_2}{P_2}. \quad (3.68)$$

The relative size of the injection space is then found in the same way. The absolute volumes

can be measured by expanding from the expansion space into a space with an already known volume. Typically we use Swagelok DOT-compliant sample cylinders as our xenon space. These are fabricated to have a specified volume, so we calculate the absolute volume of the expansion and injection spaces by referencing this specified volume.

To prepare the calibration xenon, the injection space is filled to some known pressure with pure krypton. The krypton is then opened to the expansion space in order to reduce the pressure, and then the expansion space is pumped out using a the turbo-pump until PT2 reads  $< 1 \times 10^{-6}$  torr. This expansion is repeated until the desired krypton pressure is reached. After the final expansion volume pump-out, the xenon space is opened to the injection volume, and the new xenon/krypton mixture is frozen back into the xenon volume using liquid nitrogen. The krypton concentration ( $\Phi_{Kr}$ ) of the calibration xenon in grams krypton per grams xenon is given by:

$$\Phi_{Kr} = \frac{a^N P_{Kr,0} V_{inj} \rho_{Kr}}{P_{Xe} V_{Xe} \rho_{Xe}}, \quad (3.69)$$

where the expansion ratio,  $a$ , is given by  $V_{inj}/(V_{inj} + V_{expansion})$ ,  $N$  is the number of expansions,  $P_{Kr,0}$  and  $P_{Xe}$  are the krypton and xenon pressures initially injected into the system, and  $\rho_{Kr} = 3.4692$  g/liter and  $\rho_{Xe} = 5.4535$  g/liter are the krypton and xenon gas densities.[41]

Except for the densities, which are assumed to be exact, the pressures and volumes usually have comparable fractional uncertainties, with the exception of  $V_{inj}$ , which will be slightly dominant. After a few expansions this dominance becomes more pronounced. If we keep in mind the definition of  $a$  from above, we find the following expression for the

uncertainty on  $\Phi_{Kr}$ :

$$\sigma_\Phi^2 = \Phi_{Kr}^2 \left[ \left( (N+1) \frac{\sigma_{V_{inj}}}{V_{inj}} \right)^2 + \left( N \frac{\sigma_{V_{exp}}}{V_{exp}} \right)^2 + \left( \frac{\sigma_{P_{Kr}}}{P_{Kr}} \right)^2 + \left( \frac{\sigma_{P_{Xe}}}{P_{Xe}} \right)^2 + \left( \frac{\sigma_{V_{Xe}}}{V_{Xe}} \right)^2 \right]. \quad (3.70)$$

This expression is not a perfect estimation of the error on the uncertainty. Typically either  $V_{inj}$  will be used to measure  $V_{exp}$ , or vice versa. To incorporate the effects of correlated uncertainties, we can run the calculations for volume measurements and concentrations many times, randomly varying the pressure measurements and reference volume according to their respective uncertainties.

The final injection pressure must be kept above 0.01 torr to ensure the krypton remains above the molecular flow regime. This sets a lower limit on the concentration of calibration xenon that can be produced through this method. With an injection volume of 5cc and a xenon volume of 4000cc, the lowest concentration than can be produced from pure krypton is about 5 ppB. In order to produce calibration xenon with smaller concentrations, the pure krypton is replaced with the ppB level calibration xenon, which is diluted into clean xenon through the same process outlined in the previous paragraph.

### 3.7 Sensitivity Demonstration at SLAC

With our system optimized to the best of our ability, we predict that we will be able to measure krypton contamination in a xenon sample of roughly 5 ppQ gram per gram. Our procedure will utilize the results from all of our optimization studies. The RGA CDEM voltage was set such that the highest xenon peaks were saturating the data collection, and the doubly ionized  $^{124}\text{Xe}$  peak was reading 2300 pTorr. For our setup, this was 1750 Volts. The xenon flow rate used was 2.5 SLM, and the impedance was set to 90x. We used the modified technique of forming the ice kernel, using only 50 standard cc and forming the

kernel prior to fully submerging the trap in the LN bath. This technique was described in section 3.3.2.

For all of the tests in this demonstration we used a single sample of xenon. To initially prepare this sample, we filled our  $4073 \pm 5$  cc sample volume (the green section in figure 3.26) with  $2720 \pm 14$  Torr of xenon. Using the method described in section 3.6, we cleaned this xenon to the point where were no longer able to detect krypton. Into this clean xenon we mixed very small amounts of xenon which was previously-prepared with 274 ppB “cocktail xenon”. After every analysis run, we would refreeze this xenon into SB, and then do whatever combination of cleaning and mixing was necessary to prepare for the next desired test.

### 3.7.1 Blank Runs

We analyze the RGA data from the 84 amu peak ( $PP_{Kr,i}$ ) according to equation 3.60, leaving off the constant term:

$$X = \sum_{\text{flow start}+20\text{sec}}^{\text{flow stop}} (PP_{Kr,i} - \overline{PP_{Kr,0}}) \Delta t_i. \quad (3.71)$$

The error propagation for this is:

$$\sigma_X^2 = \sum_{\text{flow start}+20\text{sec}}^{\text{flow stop}} (\sigma_i^2 + \sigma_0^2/N_B) \Delta t_i^2, \quad (3.72)$$

where  $\sigma_i$  is defined by equation 3.61. As before,  $\overline{PP_{Kr,0}}$  is the average of the RGA readings at 84 amu prior to starting flow,  $\sigma_0$  is the standard deviation of these points, and  $N_B$  is the number of these points used. We will only include the data in the closed time interval starting 20 seconds after flow was started and ending at the time the flow stopped. This  $X$  will be the figure of merit we use in establishing our limit of sensitivity. We will measure  $X$

for a series of prepared concentrations of xenon,  $\Phi$ . If our system is working as predicted, the data  $(\Phi, X)$  will fit to a line with a slope equal to  $F_{Q,t_1,t_2} C$ .

Before demonstrating that the system is capable of a positive measurement, we first show that it is capable of measuring 0 ppQ. To do this we start with our newly cleaned xenon, and run a series of “blank” measurements in which we do not mix krypton into the xenon. The values of  $X$  in these blank runs should fluctuate around 0  $pTorr \cdot s$ , although there may be some offset due to RGA baseline issues. Our measurements bear this out. We ran 15 blank runs. The average value of  $X$  for these runs was 10 pTorr seconds, and the standard deviation was 31 pTorr seconds. The average uncertainty on these points is  $\sigma_X = 26.2 \pm 0.8$  pTorr seconds.

There was one significant outlier in our blank data which had a value of  $118 \pm 35$  pTorr seconds. We decided not to use this datapoint because the RGA baseline was acting up and had a clear periodicity. We made sure that our other measurements were taken on top of an unvarying baseline.

### 3.7.2 Mixing of ppQ Level Samples

The previously mentioned 274 ppB cocktail xenon<sup>7</sup> was prepared using a separate system at the University of Maryland. The volumes of this system were measured by volume sharing as described in section 3.6. The pressure gauge used was an MKS Baratron 722b capacitance manometer. The accuracy of the 722b pressure gauge is 0.5% of the reading. We also observe a constant zero offset of the gauge to be  $0.8 \pm 0.5$  Torr which will be subtracted from the pressure readings. The absolute reference volume was a 500cc Swagelok DOT-compliant sample cylinder. The output of this bottle was modified to accommodate a 1/4 inch VCR B-series bellows valve. We take the volume of this space to be  $500 \pm 10$  cc. This reference volume doubled as the xenon space.

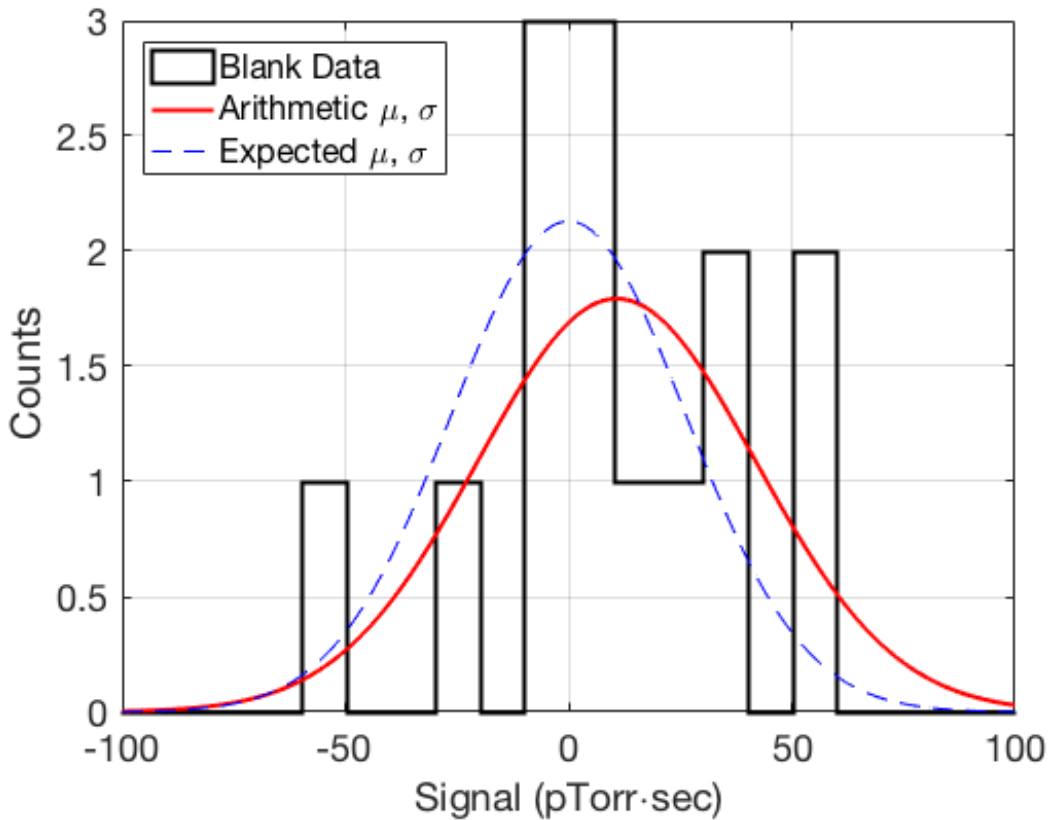


Figure 3.31: Histogram of measurements of xenon which has  $< 1$  ppQ of krypton.

The volume of the injection space was measured to be  $16.00 \pm 0.25$  cc. The expansion ratio is  $a = 0.0261 \pm 0.0008$ . The starting xenon pressure was  $841 \pm 4$  Torr in the 500cc xenon space. We injected an initial krypton pressure of  $638 \pm 3$  Torr in the injection space. We expanded three times before mixing it with the xenon yielding a mixture with  $276 \pm 25$  ppB (g Kr)/(g Xe).

The second-order mixings to dilute the 276 ppB cocktail xenon were done in-situ in the SLAC system. The SLAC sampling system is diagramed in figure 3.32. The blue boxes and corresponding arrows indicate the various isolated spaces in the system, the volumes for which are listed in table ???. The spaces of interest for mixing are spaces 1, 3, 4, 5, 6, and 7. The cocktail xenon is stored in space 6, the clean xenon is held in spaces 1, and the

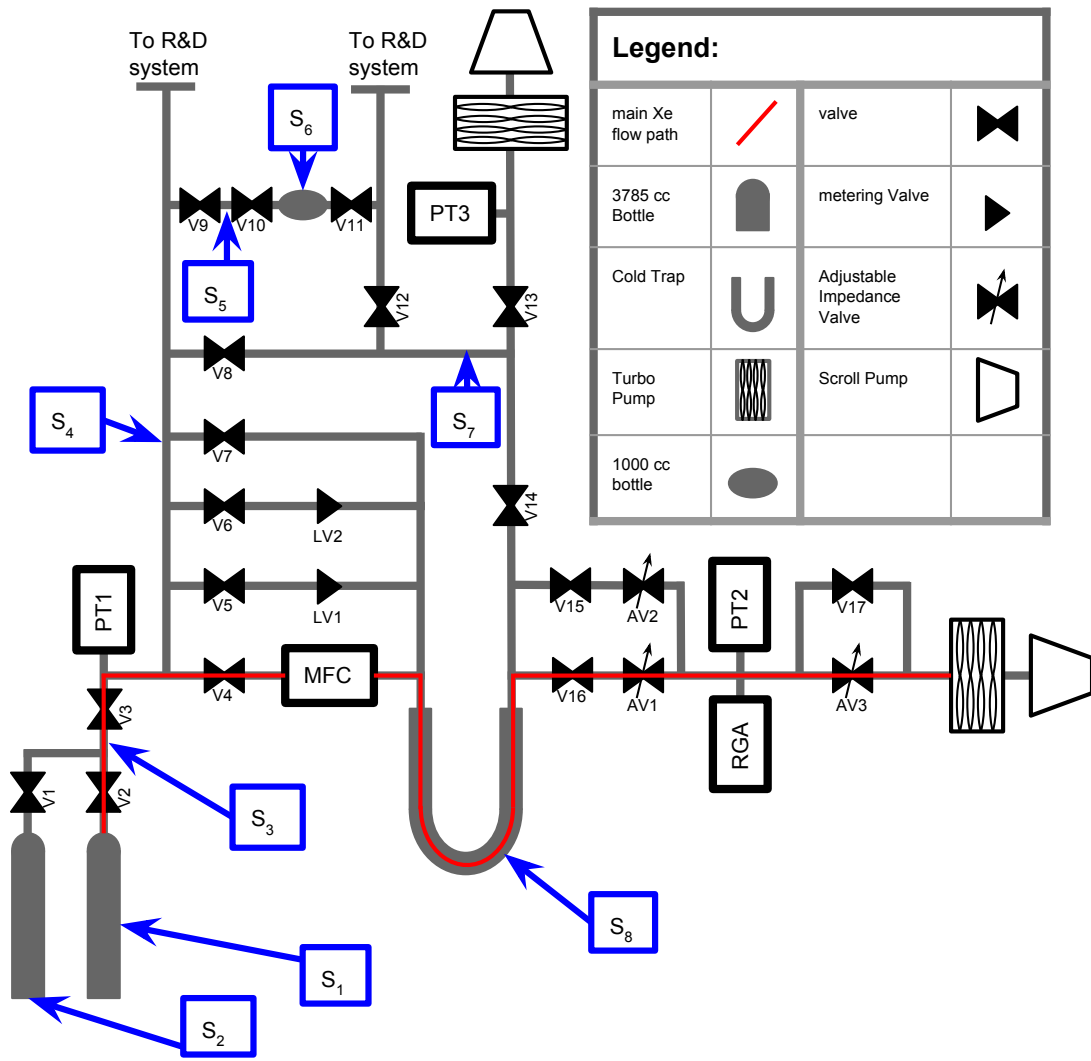


Figure 3.32: P&ID of the SLAC sampling system.

injection volume is space 5. As our primary expansion volume we used space 4 and used spaces 7 and 3 to increase the volume as needed.

The cocktail xenon was initially at a pressure of  $128.0 \pm 0.6$  Torr. Since we do not have a pressure gauge on space 6, every time we volume share with the injection volume, we calculate the new pressure contained in space 6. This calculation is simply the old pressure multiplied by the volume ratio  $(4.9 \text{ cc})/(4.9 \text{ cc}+1000 \text{ cc})=0.0049$ .

The procedure for mixing follows the same outline as in section 3.6. We select a desired

Space #	Volume (cc)	$\pm$ (cc)
1	3864	10
2	3837	10
3	23.9	1.4
4	186.3	1.9
5	4.92	0.09
6	1000	5
7	93.8	1.6
8	221.0	4.9

Table 3.2: List of SLAC system volumes. Refer to figure 3.32 for descriptions of spaces.

$\Phi$ (ppQ)	$\pm$ (ppQ)	Expansion Spaces	$N_{exp}$	$N_{inj}$	$P_{inj}$ (Torr)
4.92	0.49	5+7	2	1	128
4.90	0.49	5+7	2	1	127.4
10.8	1.1	5	2	1	126.8
21.6	2.2	5	2	2	126.3,125.8
46.1	4.9	(5),(5+3)	1,1	1*	125.2
10.7	1.1	5	2	1	124.6
255	24	5+7+3	1	1	124.0

Table 3.3: Parameters of the sample concentrations used to demonstrate the sensitivity of the SLAC system. The indicated uncertainties do not include the 7% systematic uncertainty from the cocktail xenon concentration.

sample concentration ( $\Phi_{Kr}$ ), choose the appropriate expansion space ( $V_{exp}$ ), expand the required number of times ( $N_{exp}$ ), and then mix the remaining cocktail xenon into the clean sample xenon. The resulting concentration will be given by:

$$\Phi_{Kr} = \frac{(274 \text{ ppB}) \cdot (4.9 \text{ cc}) \cdot P_{inj}}{(4073 \text{ cc}) \cdot (2720 \text{ Torr})} \left( \frac{4.9 \text{ cc}}{4.9 \text{ cc} + V_{exp}} \right)^{N_{exp}} \quad (3.73)$$

The actual values used in the preparation of our ppQ level samples are listed in table ???. The total expansion volume will be equal to the sum of volumes indicated in the “Expansion Spaces” column. There are two samples with slightly altered mixing procedures. The 21.6 ppQ sample was prepared by completing two consecutive injections using the same mixing parameters in order to approximately double the previous 10.3 ppQ concentration. The

46.1 ppQ sample was prepared in a slightly more complex way. We first filled the injection volume (space 5) and expanded once into space 4 as usual. However, after pumping out the expanded cocktail xenon in space 4, we expanded into both space 4 and space 3. We then pumped out spaces 4 and 5, and mixed our clean sample xenon with the cocktail xenon that had expanded into space 3. The calculation for this concentration is then:

$$\Phi_{Kr} = \frac{(274 \text{ ppB}) \cdot (24.4 \text{ cc}) \cdot (125.2 \text{ Torr})}{(4073 \text{ cc}) \cdot (2720 \text{ Torr})} \frac{4.9 \text{ cc}}{189.2 \text{ cc}} \frac{4.9 \text{ cc}}{213.6 \text{ cc}} \quad (3.74)$$

### 3.7.3 Measurements of ppQ Level Samples

With the measurability of 0 established, and low-concentration xenon samples in hand, we move to measure the sensitivity limit of the SLAC sampling system. To do this we first measure  $X$  as described in equation 3.71 for each of the samples listed in table ??, and then fit a line to the set of  $(\Phi_{Kr}, X)$ . The data and best-fit line are shown in figure 3.33. The slope of the best fit line is  $10.1 \pm 1.4$  pTorr seconds/ ppQ, and the intercept is  $22 \pm 12$  pTorr seconds.

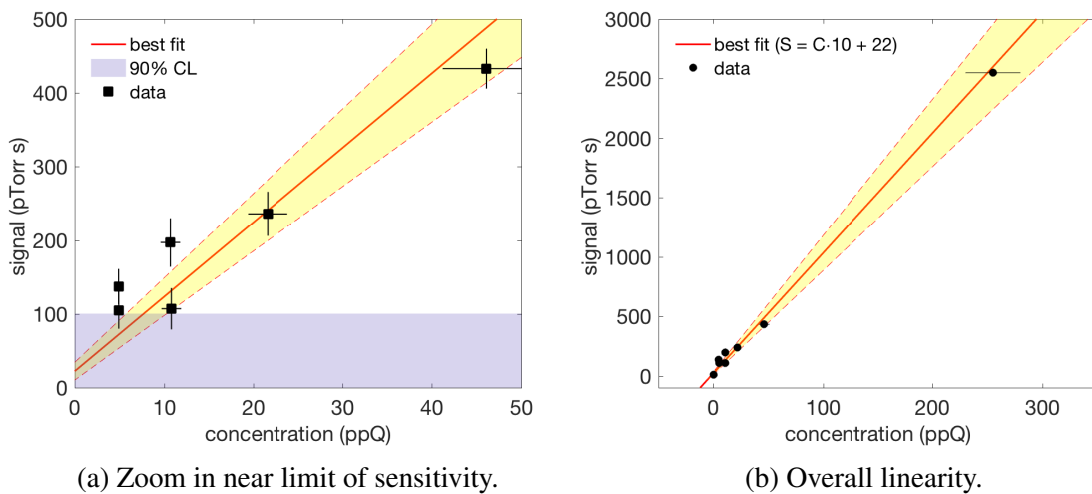


Figure 3.33:

The limit of sensitivity will be defined as the concentration at which 90% of analyses will produce results greater than  $1-\sigma$  above a 0 ppQ measurement. Our 0 ppQ measurements have a signal of  $10 \pm 31$  pTorr seconds. The lowest-concentration measurements ( $< 30$  ppQ) deviate off of the best fit line by 46 pTorr seconds, so the 90% confidence limit at any concentration will be 59 pTorr below the best fit line. Putting this together, we are looking for the concentration at which the best fit line drops crosses 100 pTorr seconds. This puts our limit of sensitivity at  $7.7 \pm 2.0$  ppQ.

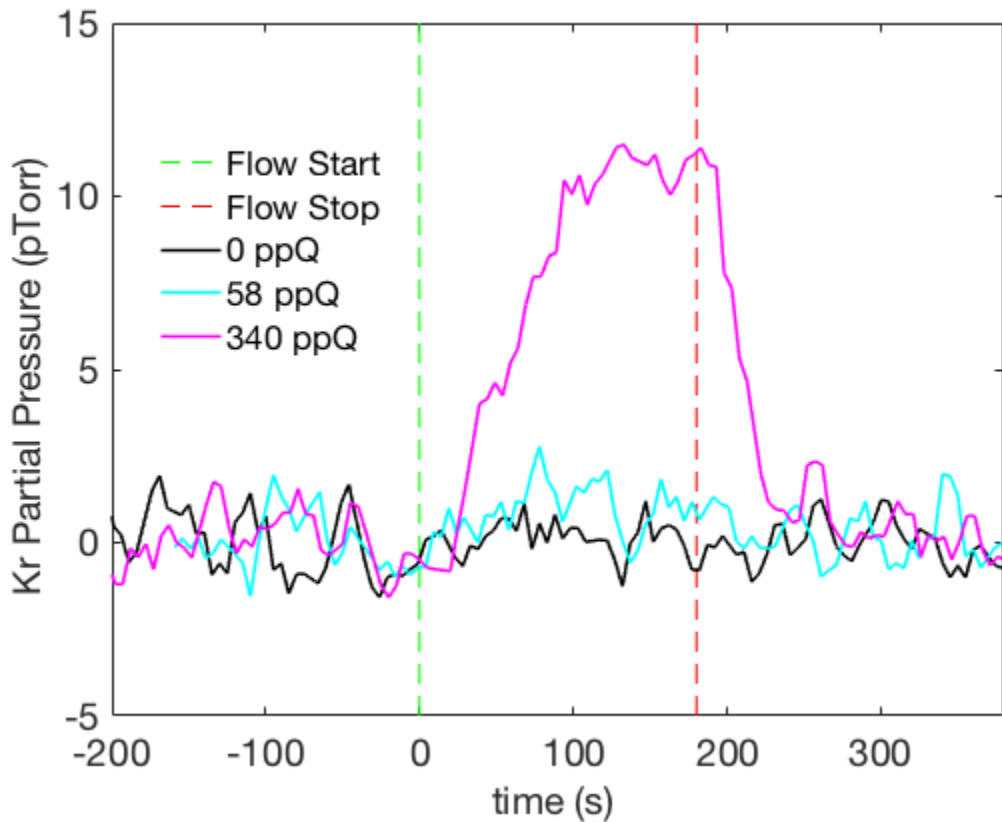


Figure 3.34: Krypton pressure vs time traces near the limit of sensitivity.

## Chapter 4: LUX Post-Run 04 Calibration Campaign

After the LUX Run4 WIMP-search was completed in June of 2016, the response of the detector was exercised using ER and NR calibration sources. The usual ER calibrations of krypton-83m[36, 37] and tritiated methane ( $\text{CH}_3\text{T}$ )[7] were performed, along with NR calibrations using the deuterium-deuterium (DD) neutron generator[6, 63]. In addition to these standard calibrations, there were additional techniques and sources used which were novel to the LUX detector.

The first novel calibration performed was a modification to the DD NR calibration. The rest of these new calibrations were to the ER response and will be the primary focus of this chapter, but we will pause here briefly to discuss the DD calibrations. The NR response of the LUX detector was measured using a beam of neutrons which was directed into the cryostat. These neutrons were generated using a commercially available DD generator,

Source	Date	$\tau_{1/2}$ (days)	Energy (keV)	Rate (Hz)
DD	-8/7, 8/22-8/23	-	(<355)	-
Kr-83m	8/2, 8/8, 8/10, 8/17, 8/25, 8/31	0.076	41.5	130
Xe-131m	8/9	12	163.9	10
$\text{CH}_3\text{T}$	8/18	0.3	0-18.1	50
$^{14}\text{CH}_4$	8/23	0.3	0-156	100
Rn-220	8/27, 8/29	0.3		50
Ar-37	8/31	0.3	35	70

Table 4.1: Table sources which were used during the post-Run04 calibration campaign.

and were collimated using a gas filled conduit which was suspended in the water tank. Because the neutrons entering the detector have a known energy and direction, it is then possible to calculate the precise recoil energy of a neutron from the beam scattering off of a xenon nucleus, assuming the scattering angle is known. The calculation is the same for neutron-nucleus scattering as for WIMP-nucleus scattering:

$$E_R = \frac{E_n r}{2} [1 - \cos(\theta)], \quad (4.1)$$

where  $\theta$  is the scattering angle in the center of mass frame, and  $r = 4M_A M_n / (M_A + M_n)^2$ . The scattering angle in the lab frame can be easily measured for events where the scattered neutron interacts with a second xenon atom before exiting the detector, and for large nuclei such as xenon, the approximation  $\theta_{CM} \approx \theta_{LF}$  can be made. The result of this procedure is a continuous NR recoil spectrum where the energy of each event is precisely known. These events will be located along the beam line, so will all be at roughly the same drift time. By moving the conduit up and down, the detector NR response as a function of drift time can be mapped out[6, 63].

The novel modification to the DD calibration in the post-run 04 campaign was to first scatter the neutrons off of a D<sub>2</sub>O target before sending them into the conduit. The only neutrons of a single, known, scattering angle will pass through the conduit, so this procedure effectively converts the 2.45 MeV mono-energetic neutron source to a 272 keV mono-energetic neutron source. The main portion of the post-Run4 DD campaign ended on August 7<sup>th</sup>, although there was a final brief period of testing between August 22<sup>nd</sup> and 23<sup>rd</sup>[63].

On August 9<sup>th</sup>, <sup>131m</sup>Xe became the first of the non-standard, post-Run4 ER sources to be injected. Xenon-131m is a gamma-emitter with an energy of 163.93 keV and a half life of 11.84 days.[1]. The xenon-131m was collected from an iodine-131 pill in an otherwise

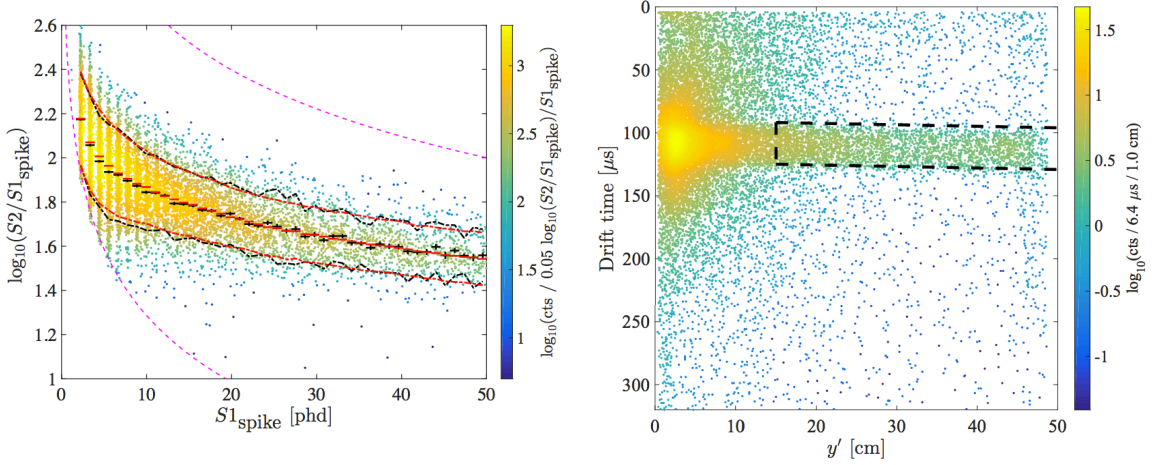


Figure 4.1: Plots of the measured neutron beam line (left) and the NR recoil band (right) from a previous LUX D-D calibration. The  $y'$  coordinate in the beam line plot is a transformation of the standard LUX  $x$  and  $y$  coordinates, such that it measures the horizontal distance along the beam line. The NR recoil band plot shows the continuous nature of the recoil spectrum. Figures taken from [6]

empty stainless steel bottle and was injected using the tritium injection described in [7]. The 12 day half life of this source meant that all subsequent sources in the month long campaign have the  $^{131m}\text{Xe}$  line as a background. The  $^{131m}\text{Xe}$  line is sufficiently separated in energy from most of the other sources, so that this background will not have a significant effect. However, the  $^{131m}\text{Xe}$  line is only 8 keV above the  $^{14}\text{C}$  Q value of 156 keV and so obscures the highest-energy portion of the  $^{14}\text{C}$  beta spectrum. This has two major effects on our analysis of the carbon-14 data. First, it limits us from probing the energy deposition properties of liquid xenon near the endpoint of the spectrum, and second, it provides an extremely useful reference point which can be used in energy calibration, efficiency corrections, and characterization of detector pathologies.

The tritium calibration was started on the 18<sup>th</sup>, and the second new ER source,  $^{14}\text{C}$  was injected five days later on the 23<sup>rd</sup>. Both of these sources rely on the injection of radio-labelled methane and are purified out by the LUX getter with a time constant of about 10 hours. This means that the tritium will have been reduced by about 12 e-folds, or a factor of 150,000, by the time the  $^{14}\text{C}$  was injected. Since the amount of tritium events in this

injection was about 1 million, there should be an overlap of  $<10$  events in the  $^{14}\text{C}$  injection.

The next source injected was radon-220. There were two injections, each with peak activity of about 50 Hz on the 27<sup>th</sup> and 29<sup>th</sup>. Radon-220 is part of the thoron-232 decay chain, which ends with the stable lead-208. The transition time from  $^{220}\text{Rn}$  to  $^{208}\text{Pb}$  is dominated by the  $\beta^-$  decay of  $^{212}\text{Pb}$  to  $^{212}\text{Bi}$ , which has a half life of about 10.6 hours.

A 70 Hz injection of  $^{37}\text{Ar}$  took place on the 31<sup>st</sup>, about 3 days after the second radon-220 injection. This meant that there was about 1 Hz of  $^{212}\text{Pb}$  remaining in the detector. The most common and most energetic  $^{37}\text{Ar}$  decay will deposit 2.8 keV into the xenon via x-ray. The low energy of the decay means that the  $^{37}\text{Ar}$  events will be well separated from the MeV-level alphas and betas of  $^{212}\text{Pb}$  and its daughters. The high rate and 35 day half life of the injected  $^{37}\text{Ar}$  meant that this was the final injection performed in the post-Run4 campaign, and was in fact the last physics data collected by the LUX detectors.

The rest of this chapter will focus on the  $^{131m}\text{Xe}$ ,  $^{37}\text{Ar}$ , and  $^{14}\text{C}$  sources. We will also present a review  $^{83m}\text{Kr}$  and  $^3\text{H}$ . This particular suite of sources is exciting in the fact that it includes two continuous beta spectra, which can be used to map out xenon ER yields from 140 keV down to threshold, as well as three ER lines that can be used to correct for position dependent detector efficiency and examine systematic pathologies.

## 4.1 Data Selection

There were several preliminary data selection cuts applied to isolate the  $^{37}\text{Ar}$  K-capture,  $^{131m}\text{Xe}$ ,  $^{83m}\text{Kr}$ ,  $^3\text{H}$ , and  $^{14}\text{C}$  events. The time interval which these events were drawn from is August 17<sup>th</sup> until September 3<sup>rd</sup>. In figure 4.2 this corresponds to the third krypton injection at T=16.6 days, until the end of data taking. The periods of DD generator and  $^{220}\text{Rn}$  activity were excluded (from T=21.4 to 22.3 days and T= 26.8 to 30.5 days, respectively). There was also a period of time after the  $^{14}\text{C}$  calibration, from T=24.5 to 26.8 days, where

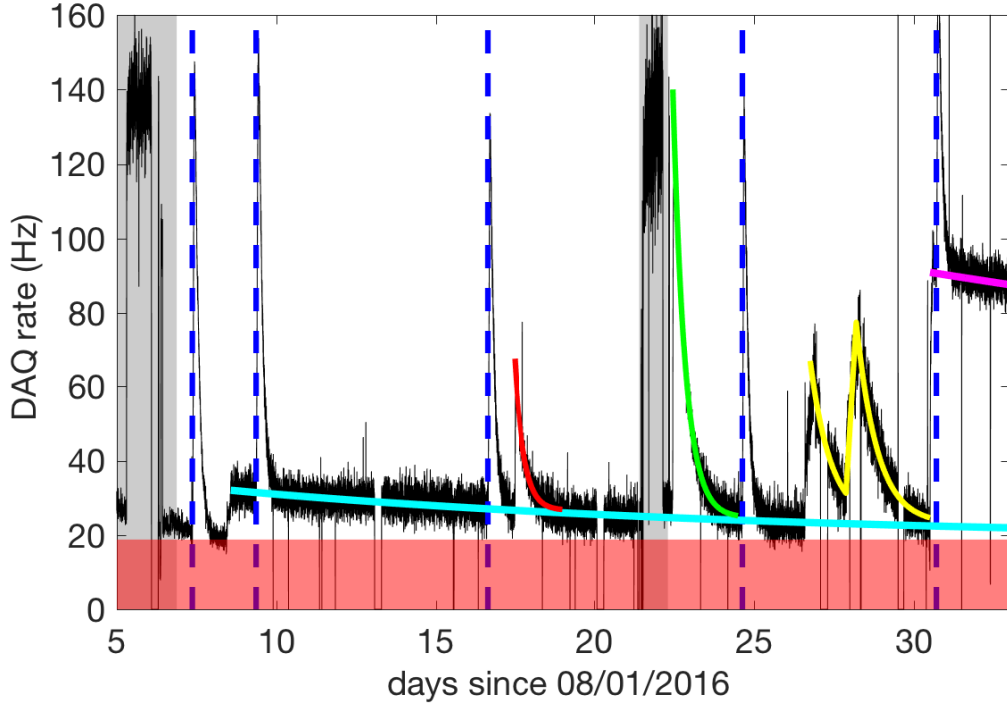


Figure 4.2: The black line shows the DAQ rate for the post-run04 injection campaign. The red shaded region shows the constant baseline, while the grey shaded regions show the DD NR-calibration campaign. The vertical dashed blue lines show the times of standard  $^{83}\text{Kr}_m$  injections. The cyan, red, green, yellow, and magenta lines trace the  $^{131m}\text{Xe}$ ,  $^3\text{H}$ ,  $^{14}\text{C}$ ,  $^{220}\text{Rn}$ , and  $^{37}\text{Ar}$  activities, respectively.

one of the PMT's was misbehaving. This time period, which included the fourth krypton injection, was also rejected.

#### 4.1.1 Single-Scatter Cut

The fully processed LUX data is organized into events. These events span a 500 microsecond window on either side of an initial trigger and is subdivided into ten “pulses” which are categorized as S1, S2, single-liquid-electron, single-photoelectron, or other. We would like to make a selection cut on single scatter events; events in which there is exactly one interaction within the detector which is located at a point position. The simplest cut one can make to this end is to keep only those events which contain exactly one S1, which

is followed by exactly one S2. This cut, however, turns out to have an energy dependence, especially above 100 keV, which will alter the shape of our continuous spectra.

We can quantify this energy dependence by looking at the Xe-131m peak. A cut on single-S1 events will only accept about 77% of Xe-131m events, while a cut on single-S2 will accept only about 68%. Combining these cuts forms a naive single scatter cut, and accepts only about 61% of the xenon-131m events. Conversely, the single scatter cut for carbon-14 events from threshold up to about 50 keV has greater than 90% acceptance.

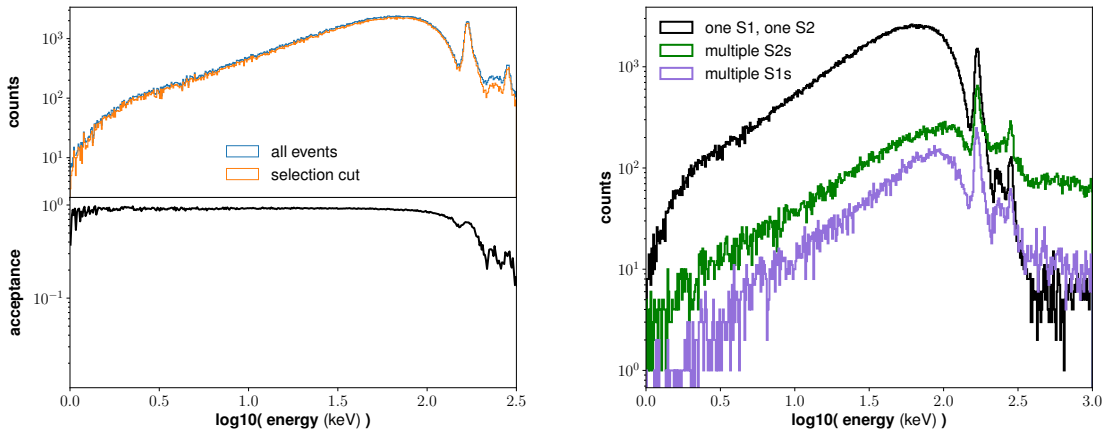


Figure 4.3: Visualization of the energy dependence of a single-scatter cut on carbon-14 and Xe-131m events. The loss of such a cut quickly rises above about 50 keV, to the point where there is less than 10% acceptance above about 500 keV.

The loss of acceptance at higher energy is largely dominated by the same pathology that is thought to cause S2 tails, which will be discussed in a later section. Electron trains are extended streams of electrons which are extracted from the liquid surface, persisting for millisecond time-scales. These trains seem to be seeded by S2s, and have a larger effect on higher-energy events. When an electron train is large enough, several of these electrons can pile up in a single pulse causing it to be classified as an S2. These secondary S2s will cause the event to fail the single scatter cut, and since the high-rate tails are more

likely at higher energy, this will introduce an energy-dependence to the single-scatter cut.

For these reasons, we developed a more nuanced cut that allows for any number of S1s and S2s to be present. We first enforce the condition that there is at least one S1 before the first S2. We then cut on the ratio of the area of the first S2 to the sum of all of the S2 areas contained in the event. The idea is that we want the first S2 to contain greater than 93% of the total S2 area, while allowing for subsequent smaller S2s to be present. We apply the cut to the S1s, however we only include S1s that occur before the first S2 in our total area sum.

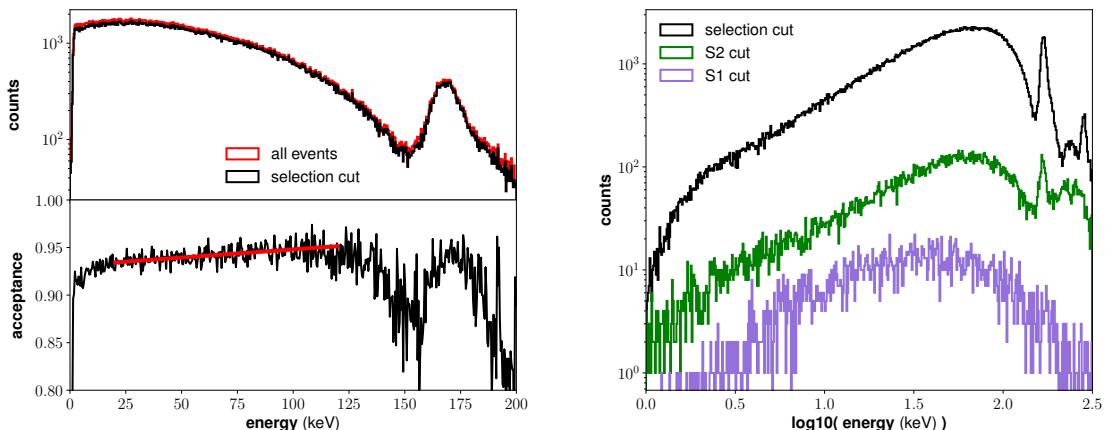


Figure 4.4: Visualization of the modified single scatter cut. This cut has a significantly better acceptance than the 1-S1, 1-S2 cut shown in figure 4.3. The acceptance of Xe131 events has been improved from 61% to about 92%. Similarly the acceptance for C-14 events is greater than 90% across the entire energy range. There is a slight slope of  $0.17 \text{ MeV}^{-1}$  to the acceptance of C-14 events which is indicated by the red best-fit line in the lower left panel.

This cut has a significantly better acceptance than the 1-S1, 1-S2 cut. The acceptance of Xe131 events is improved from 61% to about 92%. Similarly the acceptance for C-14 events is greater than 90% across the entire energy range. There is a slight slope of  $0.17 \text{ MeV}^{-1}$  to the acceptance of C-14 events which is indicated by the red best-fit line in the lower left panel. This slope will introduce a systematic error in our measurement of the carbon-14 non-statistical shape factor, which will be described in section 5.1.3.

### 4.1.2 Radial Selection Cut

We would like to be able to eliminate events close to the wall from our analysis. The LUX Run4 and post-Run4 drift field was highly non-uniform in the z-coordinate, so there must be a drift time dependence added to any radial event-selection cut. There is, to a lesser degree, some non-uniformity in the radial and azimuthal directions as well. Since we would like to make a radially symmetric selection cut, we can to, first order, ignore the radial dependence. The radial cut was defined by first dividing the detector into  $5\mu\text{s}$  drift time bins. Each drift time bin was re-centered around the mean S2-space x and y positions. These re-centered positions were then divided into 36  $\phi$  bins. We used the assumption that the argon-37 events will be distributed uniformly in radius-squared to define the cut position for each of these  $\phi$  bins. We define  $r_{cut}(dT, \phi)$  such that 77% of events in the associated bin will have  $r < r_{cut}(dT, \phi)$ . The true radius of this event should be  $\sqrt{0.77}R_{wall} = (0.877) \cdot (25 \text{ cm}) = 21.9 \text{ cm}$ . The values of  $r_{cut}(dT, \phi)$  should then all be about 3 cm from the wall. We apply this cut in each drift time bin ( $dT_i$ ) by performing a linear interpolation between the values of  $r_{cut}(dT_i, \phi)$  and cutting out events with radii greater than the interpolated values.

## 4.2 Argon-37 Non-Gaussianities

Argon-37 provides three useful low-energy ER calibration lines. It decays through electron capture to  $^{37}\text{Cl}$  with a half life of 35 days. The long half life, combined with the fact that argon is chemically inert means that once injected, it will be on the order of a year before it has been sufficiently removed. That being the case, it was only injected immediately prior to LUX decommissioning[16, 33].

The  $^{37}\text{Ar}$  source was produced through stimulated  $\alpha$  emission of a  $^{40}\text{Ca}$  target using a

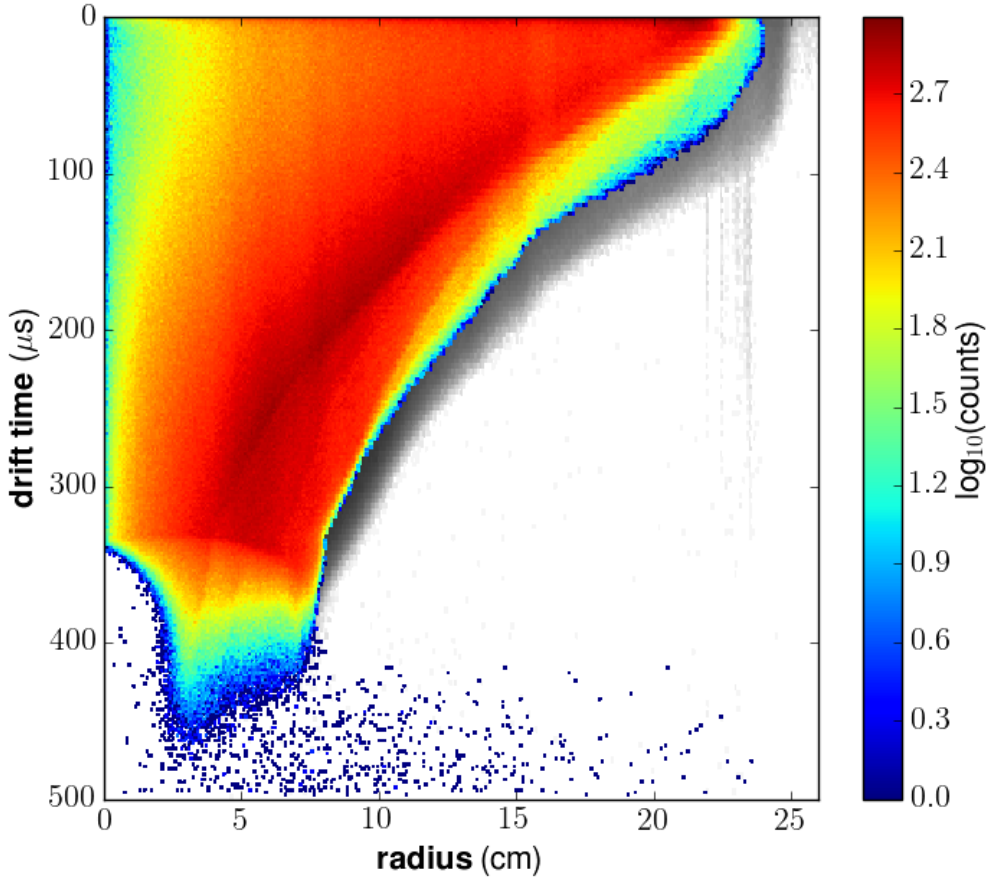


Figure 4.5: Visualization of the radial cut derived from the  $^{37}\text{Ar}$  data. The greyscale maps show the data without any position cuts, while the overlaid heat-maps show the selected by the radial cuts.

neutron beam. The  $^{37}\text{Ar}$  sample used in LUX was produced by irradiating an aqueous solution of  $\text{CaCl}_2$  with neutrons from an AmBe source. The gas above this solution was then collected and purified to obtain the gaseous sample of  $^{37}\text{Ar}$ [16]. This sample was injected into the LUX xenon circulation using the same system as the  $^{83m}\text{Kr}$  calibrations[37].

The three lines in the  $^{37}\text{Ar}$  decay are from the capture K-shell, L-shell, and M-shell electrons. The different captures have branching ratios of 0.9, 0.09, and 0.009 and will deposit x-rays with energies of 2.8224 keV, 0.2702 keV, and 0.0175 keV, respectively. The

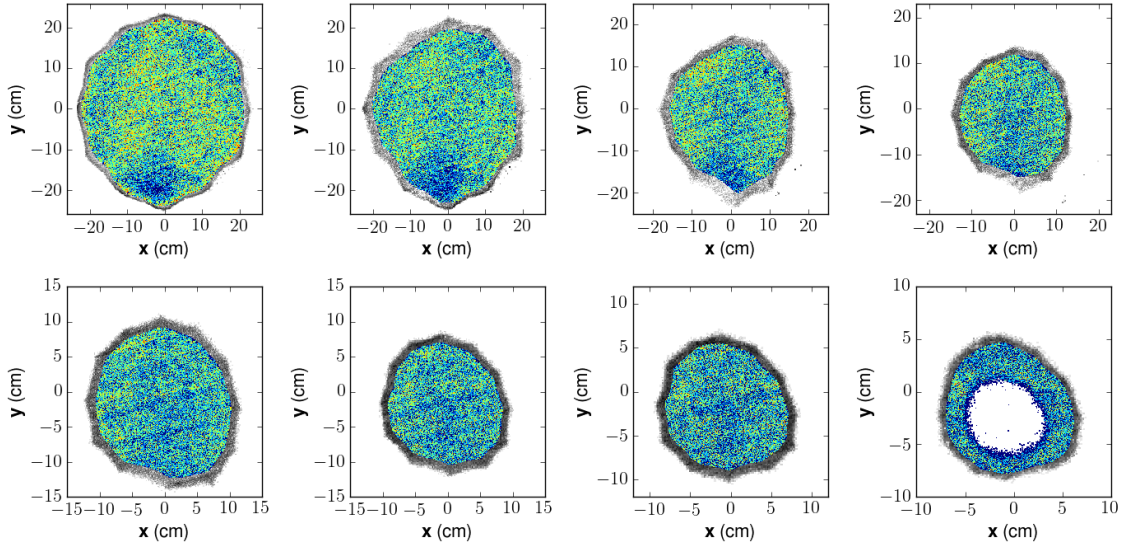


Figure 4.6: Selected  $5 \mu\text{s}$  drift time slices used in the  $^{37}\text{Ar}$  drift time section cut. The greyscale map show the data without any position cuts, while the heat-map shows the selected by the radial cuts. From top left to bottom right, the drift time of the cots are  $20 \mu\text{s}$ ,  $50 \mu\text{s}$ ,  $100 \mu\text{s}$ ,  $150 \mu\text{s}$ ,  $200 \mu\text{s}$ ,  $250 \mu\text{s}$ ,  $300 \mu\text{s}$ , and  $350 \mu\text{s}$ . The linear diagonal lines that can be seen in the heat-maps are physical features created by the grids.

L-shell and M-shell captures are below the LUX threshold and so are of limited use to the work presented in this document. The K-capture x-ray will produce about 76 scintillation electrons, which will produce an S1 signal of about 6.7 phd. This is a small enough signal that there will be some non-Gaussian distortion in the S1 spectrum due to threshold effects. The charge yield for the K-capture is about 50 electrons/keV. With a 70% extraction efficiency, there will be about 100 electrons extracted from an argon-37 event, which would produce an S2 of roughly 2500 phd assuming a single electron size of 25 phd. This is large enough that the S2 spectrum should be free of threshold effects.

The high rate and long lifetime of the argon-37 injection also meant that there was a huge number of events. From the injection on August 31<sup>st</sup> until the end of data-taking on September 3<sup>rd</sup> there were about 8.8 million argon-37 events. The fact that we have such a high-statistics dataset, combined with the spatially uniform nature of injection sources

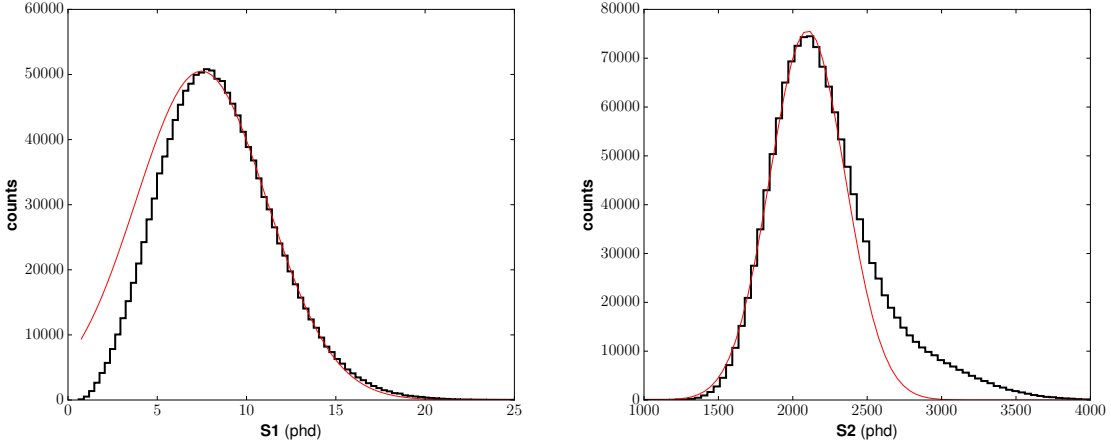


Figure 4.7: The S1 and S2 spectra for the LUX  $^{37}\text{Ar}$  injection (black histograms), along with gaussian fits (red lines). Events with drift times between 105 and 170  $\mu\text{s}$ . The S1 spectrum clearly does not behave like a gaussian on the low energy side of the spectrum. The S2 spectrum does have a gaussian shape up until about  $1 \sigma$  above the mean at which point a pathological tail takes over. These S2 tails are a known issue and will be characterized in a later section.

means that we can very finely probe the position-dependence of the detector response. This feature will be used to measure the S2 efficiency corrections and in defining our radial cut.

### 4.3 Signal Corrections fo Post-Run04 Data

#### 4.3.1 S2 Efficiency Correction from $^{37}\text{Ar}$

In Run4, the position-dependent efficiency corrections for the LUX S1 and S2 signals were obtained from a combination of tritium and  $^{83m}\text{Kr}$  calibration data. This method which was described in section 2.2.2, relies, in part, on the fact that the S2 yields for small energy deposits have a minimal dependence on electric field. The first step in the KrypCal procedure is to measure the position dependence of the tritium peak S2 value. In order to derive the detector efficiency part of the position dependence, the field effect must first be removed. This field dependence is itself dependent on the energy of the events that

contribute to the S2 peak. Since tritium is a beta spectrum, events with many energies will contribute to this peak, so an approximation is made that all of these events occur at 2.5 keV.

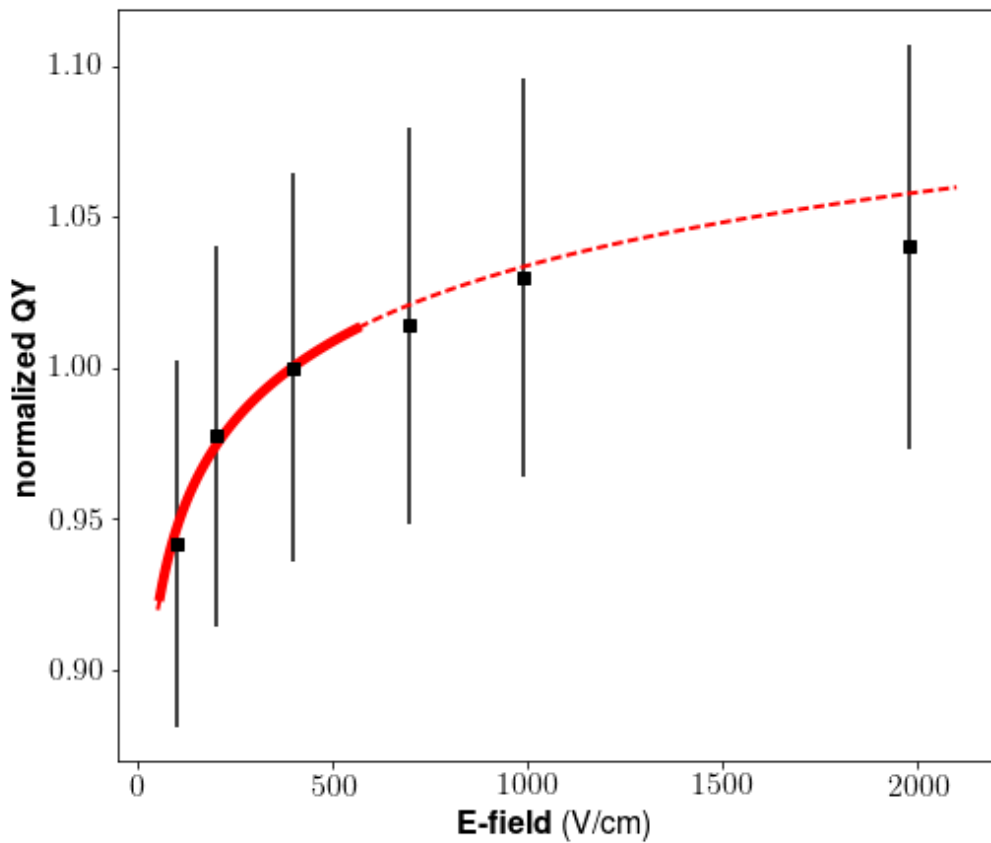


Figure 4.8: NEST model of the  $^{37}\text{Ar}$  vs the measurements from PIXeY[16]. The solid portion of the line indicates the range of fields in the LUX post-Run4 calibration data. There is about a 10% variation due to electric field in the LUX post-Run4 data. The NEST v0.98 model traces the trend in the PIXeY data quite well.

It is here that we see a huge benefit in using the  $^{37}\text{Ar}$  K-capture peak instead of the tritium beta spectrum in deriving the S2. Because  $^{37}\text{Ar}$  is a mono-energetic line source rather than a continuous beta spectrum, we know that all of the events making up the S2

peak will come from a 2.8224 keV event, and no assumption or approximation need be made.

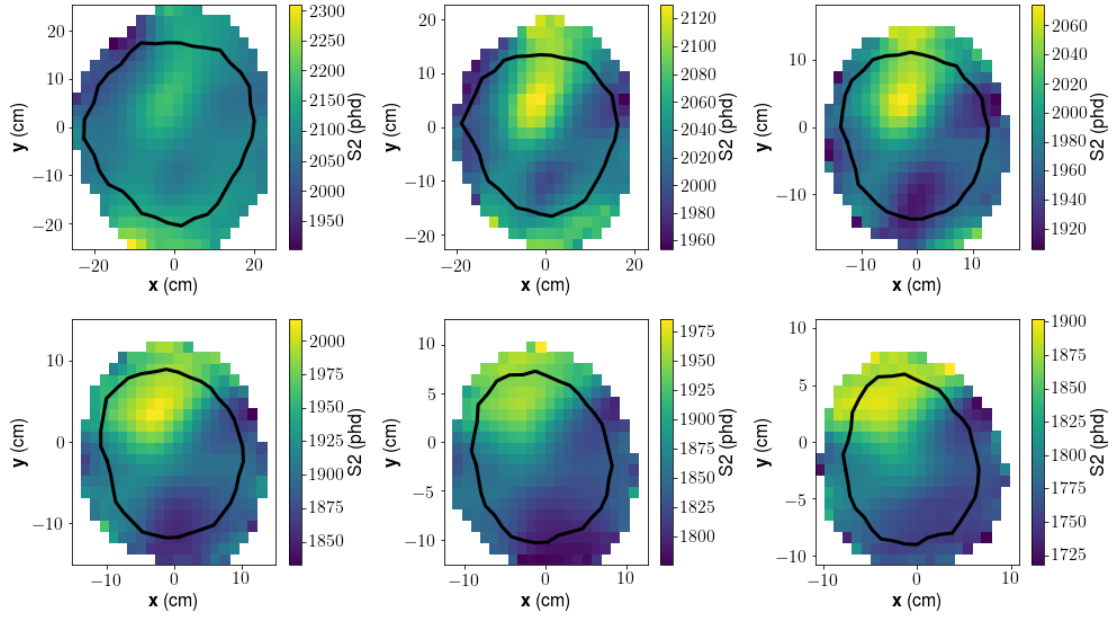


Figure 4.9: Measured Ar-37 S2 means in selected drift time bins. The bins from top left to bottom right are 50, 100, 150, 200, 250, and 300 microseconds. The black outline indicates the x-y position of the radial selection cut at the given drift time. The measurements of the S2 mean outside of this border exist because of the smearing applied in the calculation.

The first step is to divide the detector into bins of 10 microseconds. We set the highest drift time bin edge to be at 5 microseconds, which is the approximate position of the gate grid. The lowest bin edge is set to 485 microseconds, although our analysis will only include events above 330 microseconds in drift time, which corresponds to the bottom of the detector at  $x=y=0$  cm.

Each drift time bin is then divided into a  $22 \times 22$  x-y grid. The radial extent of events is highly dependent on drift time, so the density in x and y of events near the top of the detector is much less than the density near the bottom of the detector. Events from the bottom of the detector are focused from about 25 cm in real space to about 9 cm in S2 space. This means that the S2 from a wall event (25 cm radius) near the bottom of the

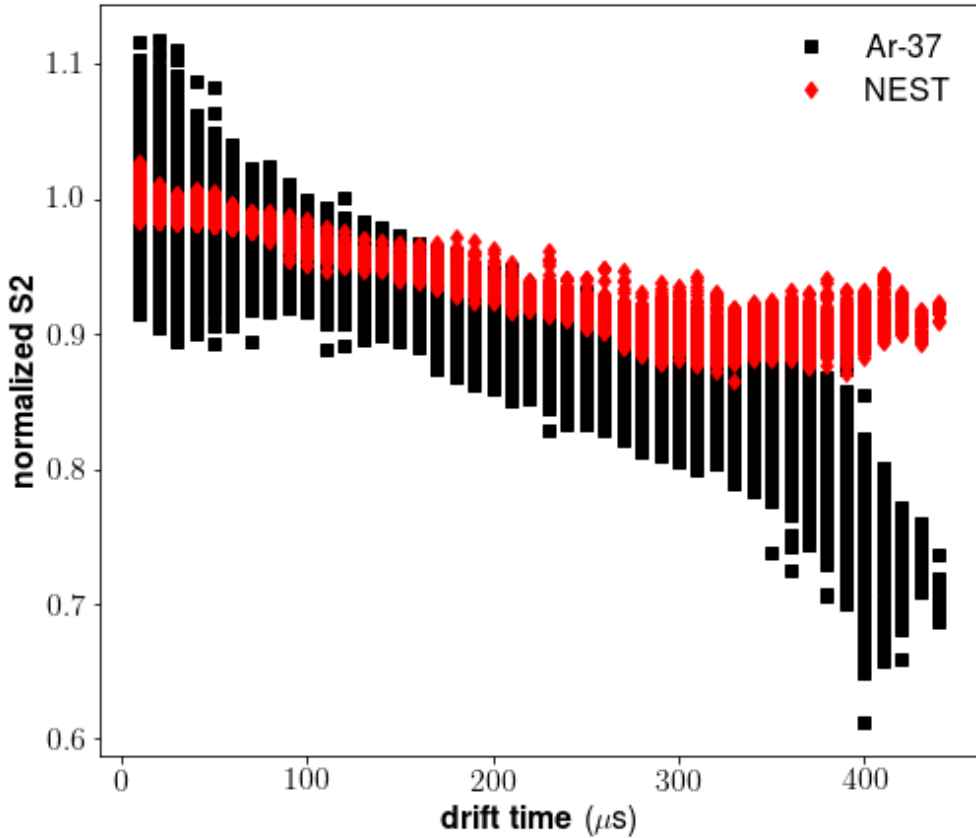


Figure 4.10: The black markers here show the measured S2 means, normalized to the top center of the detector. The red markers show the expected variation due to electric field alone. The S2 efficiency correction can be thought of as the red values divided by the black values.

detector will appear to have a radius of about 10 cm. An x-y bin with edge-width of 2 cm at the top of the detector will have an effective width of about 5 cm at the bottom of the detector. To account for these effects, we scale the x-y grid for each drift bin by the maximum radius of events within that bin. The 10 microsecond drift bin has an x-y grid that spans from -25.2 to 25.2 cm, while the 330 microsecond grid goes from -9.4 to 9.4 cm.

When calculating the mean values, we treat the drift time bins independently but allow the x-y bins to smear together. We draw a circle with a radius equal to 2.5 times the bin

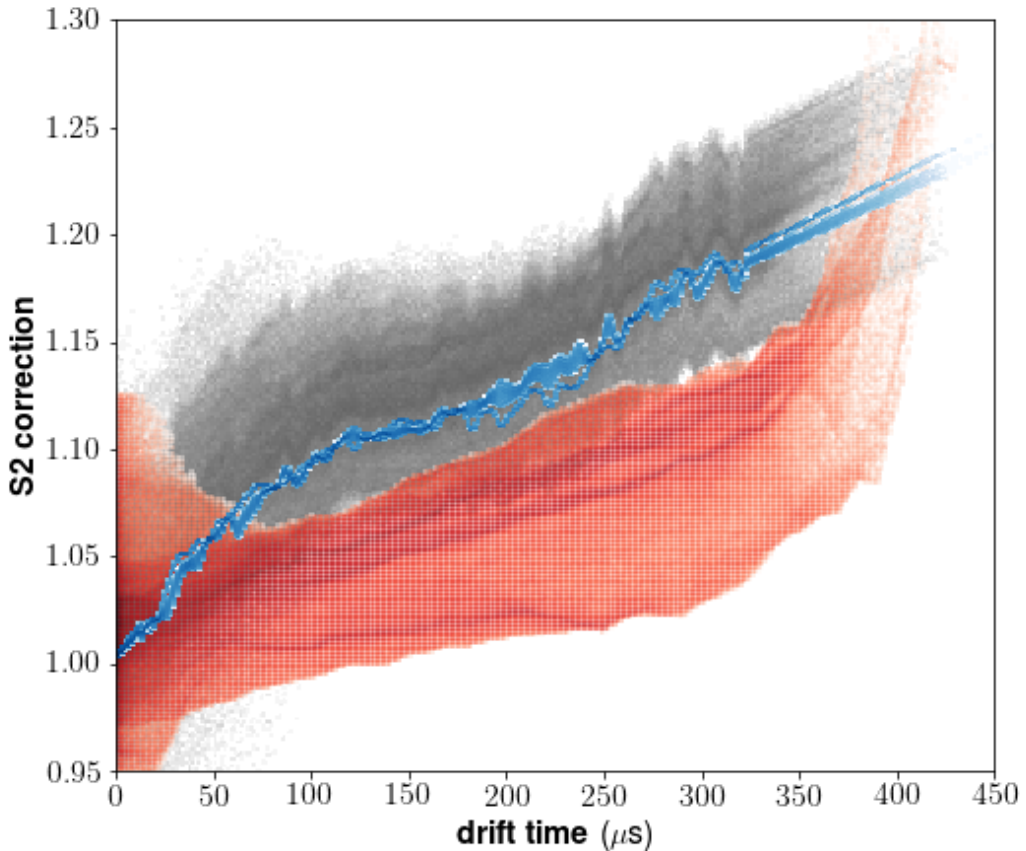


Figure 4.11: The KrypCal z-only (blue) and xyz (grey) S2 corrections compared to the Ar-37 S2 correction (red). At drift times greater than about 100 microseconds the two methods are in decent agreement. At smaller drift times, however, there is a steep trend observed in KrypCal that is not present in the corrections measured using Ar-37.

width around the center of each x-y bin. We include all of the events within that circle in our calculations for that bin. For each bin we calculate the mean S2 ( $S2_{H3,ijk}$ ), where  $i$  is the x-index,  $j$  is the y-index, and  $k$  is the drift time index, as well as the mean electric field using values interpolated from a field-map described in section 2.2.1. The electric field value is used to generate an expected S2 value from NEST, ( $S2_{NEST,ijk}$ ).

The S2 measurements need to be normalized to the top center of the detector. We

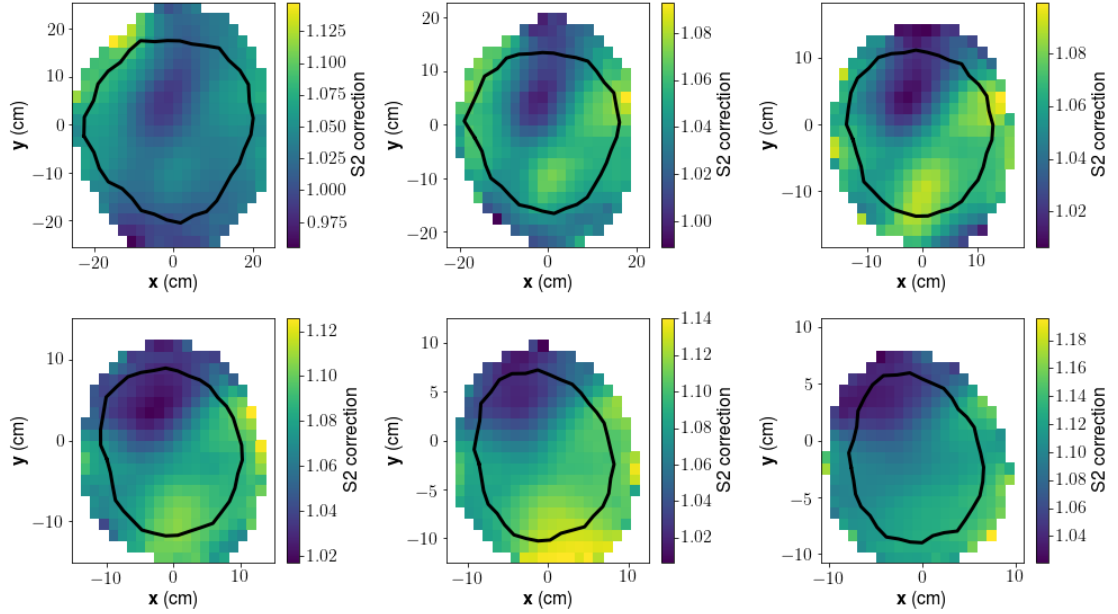


Figure 4.12: Measured S2 corrections for the same drift time bins as in figure 4.9.

calculate the S2 value in this region by taking the average of bins from the top three drift time slices that lie inside a radius of 10 cm from the center of the detector. The S2 correction is then defined:

$$C_{S2,ijk} = \frac{S2_{NEST,ijk}}{S2_{H3,ijk}} \cdot \frac{S2_{H3,top}}{S2_{NEST,top}}, \quad (4.2)$$

where  $S2_{NEST,top}$  and  $S2_{H3,top}$  are the values calculated at the center top of the detector.

Figure 4.11 shows a comparison of the S2 corrections measured using the procedure described in this section and those measured using the KrypCal procedure. Below about 100 microseconds in drift time, the slope from the two corrections methods are in good agreement. For drift times less than 100 microseconds, the KrypCal corrections see a significantly larger slope than those measured using argon-37. There are fewer assumptions that go into the argon-37 S2 corrections. In particular, the assumption that the peak of the tritium spectrum can be approximated by a mono-energetic peak has the potential to introduce systematic effects. A change in the electric field may induce enough of a change

to the charge and light yields that the energy of events in the peak of the tritium S2 spectrum is dependent on electric field.

We test this by looking at simulated tritium events which were generated using charge and light yields which will be presented in the next chapter. We take the mean input energy of events in a 200 phd window centered on the maximum of the uncorrected S2 spectrum. At the top of the detector, where electric field equals 491 V/cm, the energy of events in the peak of the S2 spectrum is 4.0 keV. At the bottom of the detector where the electric field is 43 V/cm, the energy of the S2 peak is 20% higher at 4.8 keV. At these energies, the charge yield has a steep dependence with energy, so there will likely be non-negligible systematic effects introduced by assuming the tritium S2 dependence can be approximated using a constant energy. This clearly highlights the advantage of using the mono-energetic Ar-37 peak to measure the S2 position-dependent efficiency.

### 4.3.2 S1 corrections from Xenon-131m + Krypton-83m Doke Plot

In a detector with a non-uniform electric field, the S1 efficiency correction is more complicated to measure than the S2 correction. In order to limit the effects of electric field variation, we would like to use a low-energy calibration source because the field dependence of charge and light yields is smallest at low energies. This is also the energy scale with the lowest light yield and combined with the typically low light-collection efficiency of liquid xenon TPC's (roughly 9-10% for LUX), these low-energy sources suffer from threshold effects in their S1 spectra. The KrypCal procedure feeds the S2 efficiency correction measured using tritium data into the krypton-83m S2 spectrum. This yields a field-dependent S2 spectrum which is used to measure the position-dependent recombination of krypton-83m data. This recombination measurement is then fed into the krypton-83m S1 spectrum in order to get a measurement of the S1 position-dependent efficiency.

Here we test an alternate method for measuring the S1 efficiency corrections which utilizes both the xenon-131m and krypton-83m calibration data. This method takes advantage of the fact that the field dependence of the charge and light yields is completely contained in the recombination probability. This means that when the data is plotted on a Doke-style plot, variation in the electric field will only work to move points along a line and will not change the line's parameters. The aim of this method, then, is to use a Doke-style plot to directly measure the light correction efficiency ( $G1$ ) in each of our  $(x, y, dT)$  bins which were described in the previous section. This method relies on the same recombination model the KrypCal assumes but, unlike KrypCal, does not require prior knowledge of the initial exciton to ion ratio,  $\alpha$ .

We use the same method to measure the krypton-83m and xenon-131m S1 and S2 means for each voxel as was used in section 4.3.1 to measure the S2 means of argon-37. Once these means ( $S1_{Kr83m,ijk}$ ,  $S1_{Xe131m,ijk}$ ,  $S2_{Kr83m,ijk}$ , and  $S2_{Xe131m,ijk}$ ) have been measured, we use them to measure G1 and G2 at the center of the detector. We define the center of the detector as the mean drift time of argon-37 events, which is calculated to be 162.2 microseconds. We select bins that are within 20 microseconds drift time of the detector center and have a radius less than 5 cm. We take the average of the uncorrected S1 values, and the average of the corrected S2 values ( $S2_{ijk} \cdot C_{S2,ijk}$ ). We then construct our Doke-plot using:

$$\begin{aligned} X_{center} &= W \cdot S2_{center} \cdot C_{S2,center} / E \\ Y_{center} &= W \cdot S1_{center} / E, \end{aligned} \tag{4.3}$$

where  $W = 1/73$  is the average work function for ionization and scintillation in liquid xenon, and  $E$  is the energy of the calibration line. We draw a line through the points  $(X_{Xe131m,center}, Y_{Xe131m,center})$  and  $(X_{Kr83m,center}, Y_{Kr83m,center})$ . The x-intercept of this line

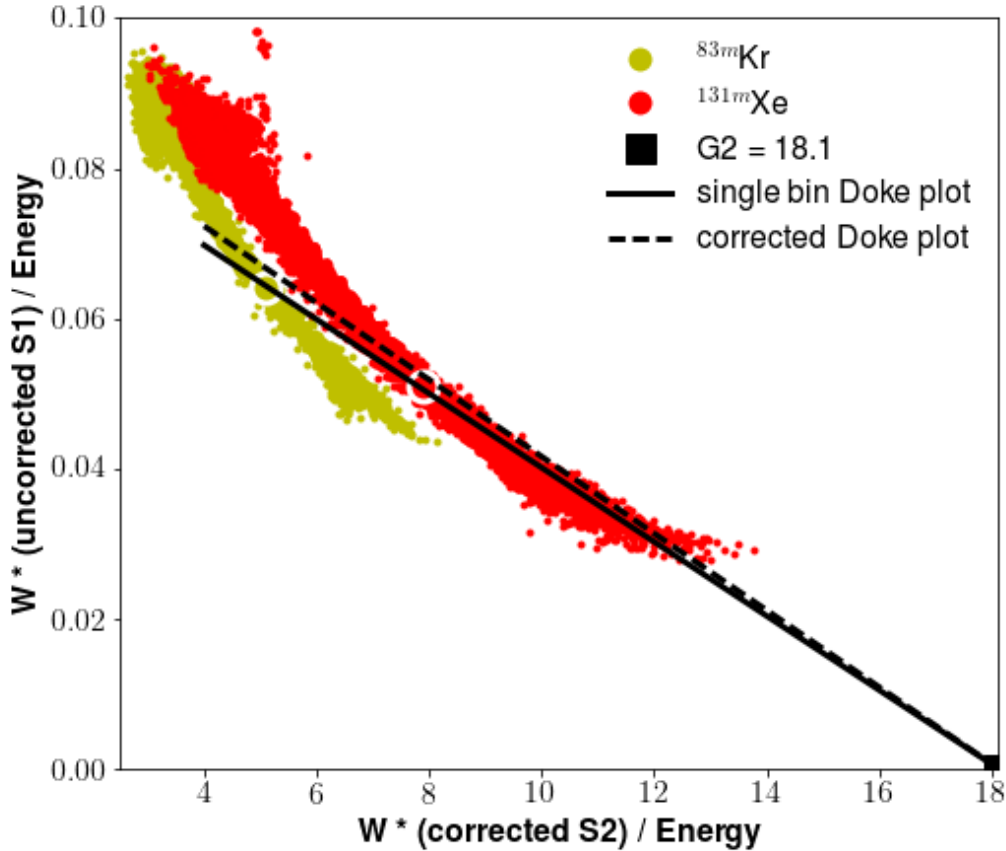


Figure 4.13: Doke plots of xenon-131m and krypton-83m for the bins described in section 4.3.1. By forcing G2 to be constant, we perform a single-parameter fit to find G1 in each bin. The solid black line shows the best fit line for the selected bin, and the dashed line represents G1, G2 as measured at the center of the detector.

will be taken to be  $G2_{center}$ , and the y-intercept will be  $G1_{center}$ .

The value of G1 for the individual voxels is calculated in the same manner as was done for the detector center. We define the points  $(X_{ijk}, Y_{ijk})$  for krypton-83m and xenon-131m in the same way we defined  $(X_{center}, Y_{center})$ . Here, instead of analytically drawing a line through the two points, we fix the x-intercept to  $G2_{center}$  and allow the y-intercept to float in order to find the best-fit  $G1_{ijk}$ . These values of  $G1_{ijk}$  are direct measurements of the position-dependent S1 efficiency, so by normalizing them to the detector center we can

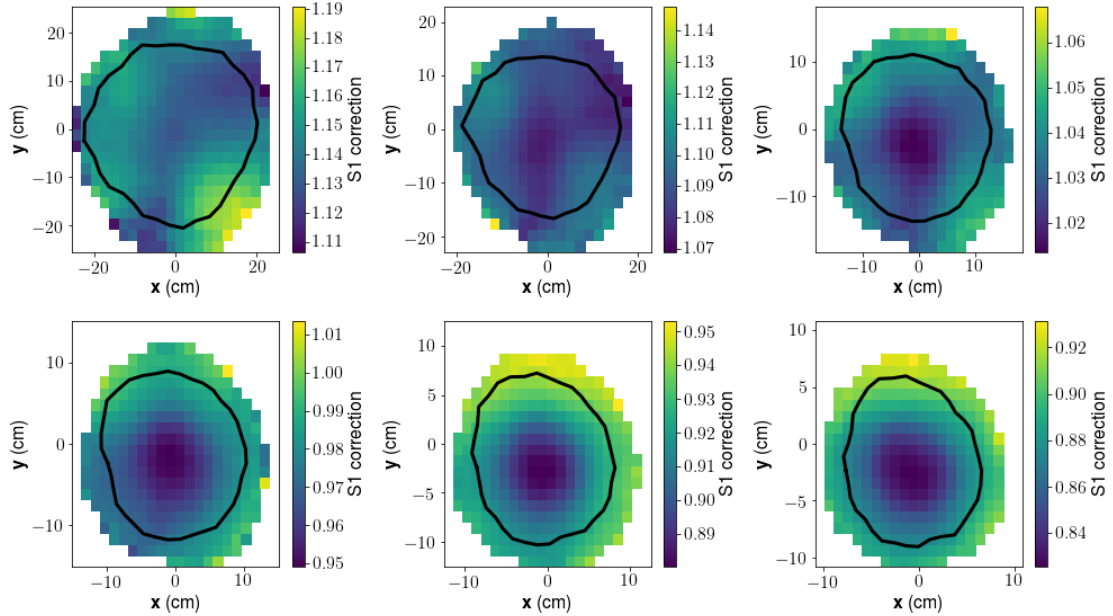


Figure 4.14: Measured S1 corrections for the same selected drift time bins as in figure 4.9.

easily write the S1 efficiency correction:

$$C_{S1,ijk} = \frac{G1_{center}}{G1_{ijk}} \quad (4.4)$$

This method of deriving the S1 efficiency correction is more consistent with KrypCal than the argon-37 S2 corrections were. This is more or less expected, since the two methods rely on the same physical assumption. The primary discrepancy between the two would be expected to come from the fact that both methods require the S2 correction as an input. The roughly 5% discrepancy in the S2 correction is subdominant to both the variation in both recombination and S1 efficiency, so it has only a minor effect on the measurement of the S1 correction.

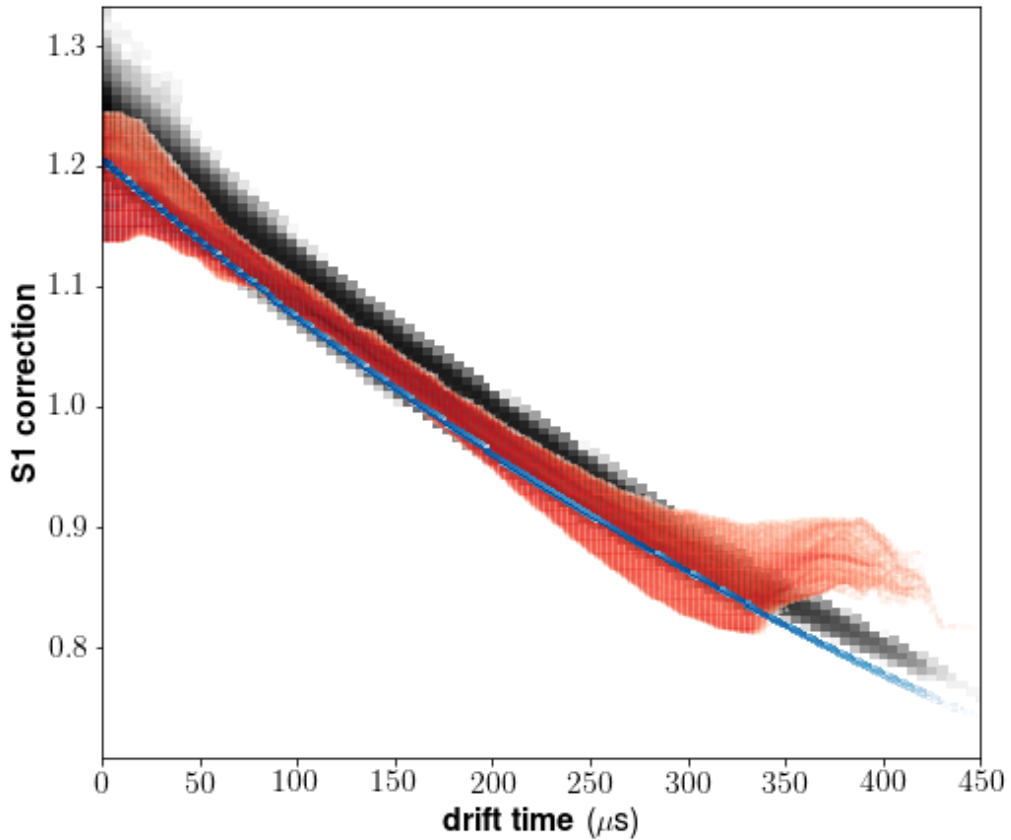


Figure 4.15: Comparison of the KrypCal z-only (blue) and xyz (grey) S1 corrections with the Doke-style S1 corrections introduced in this section (red).

### 4.3.3 Applied Corrections

Now that we have measured a new set of corrections we would like to apply them to our data in order to see how they compare to the existing KrypCal corrections. To do this we need to interpolate between the measured  $C_{S2,ijk}$  and  $CS1,ijk$  to find a set of corrections for arbitrary x, y, and dT.

In order to ensure that there is no out-of-bounds interpolation error, we set the corrections values of any empty bins equal to that of their nearest non-empty neighbor. For each

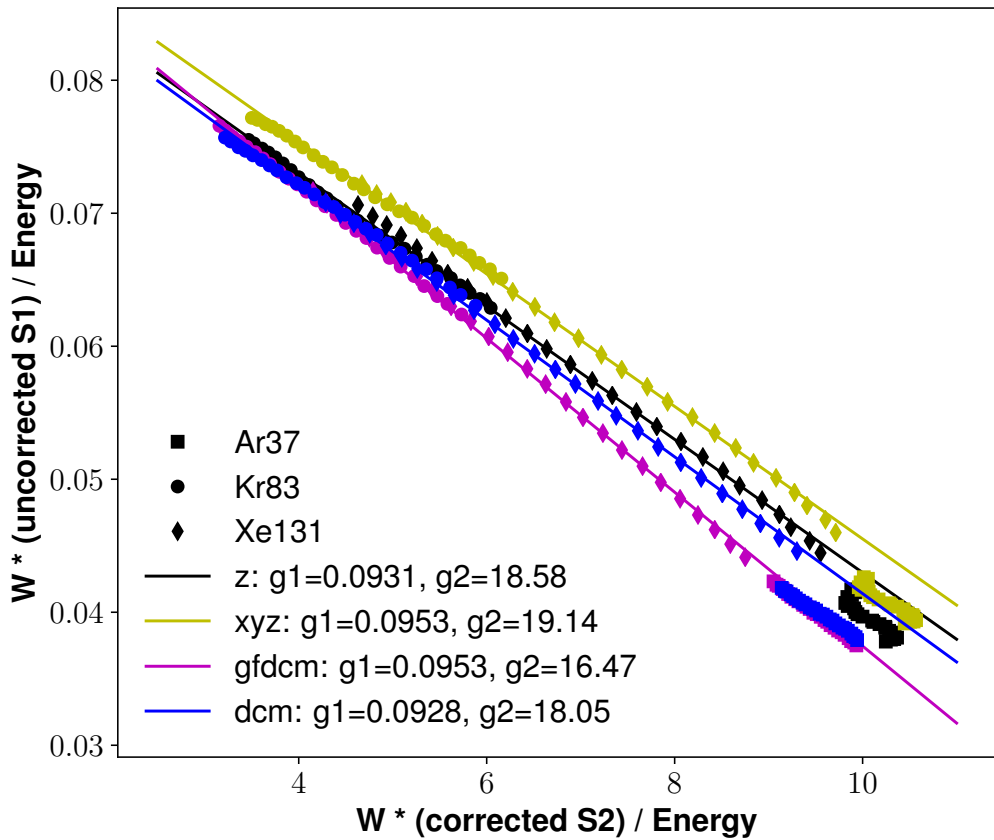


Figure 4.16:

drift time bin we apply a bivariate spline in x and y, taking  $C_{S2,ijk}$  and  $C_{S1,ijk}$  to be located at the center of their respective bins. After that we apply a linear interpolation in drift time between the values of the x-y splines. Again we assume the values are located at the centers of their respective drift time bins.

With the newly corrected data in hand, we now check to see how we did. We first need to measure the final G1 and G2 for both types of corrections to do this we finely slice the detector in drift time and generate a Doke-style plot using the same procedure as in the previous section. This time we include the krypton-83m and xenon-131m points from all

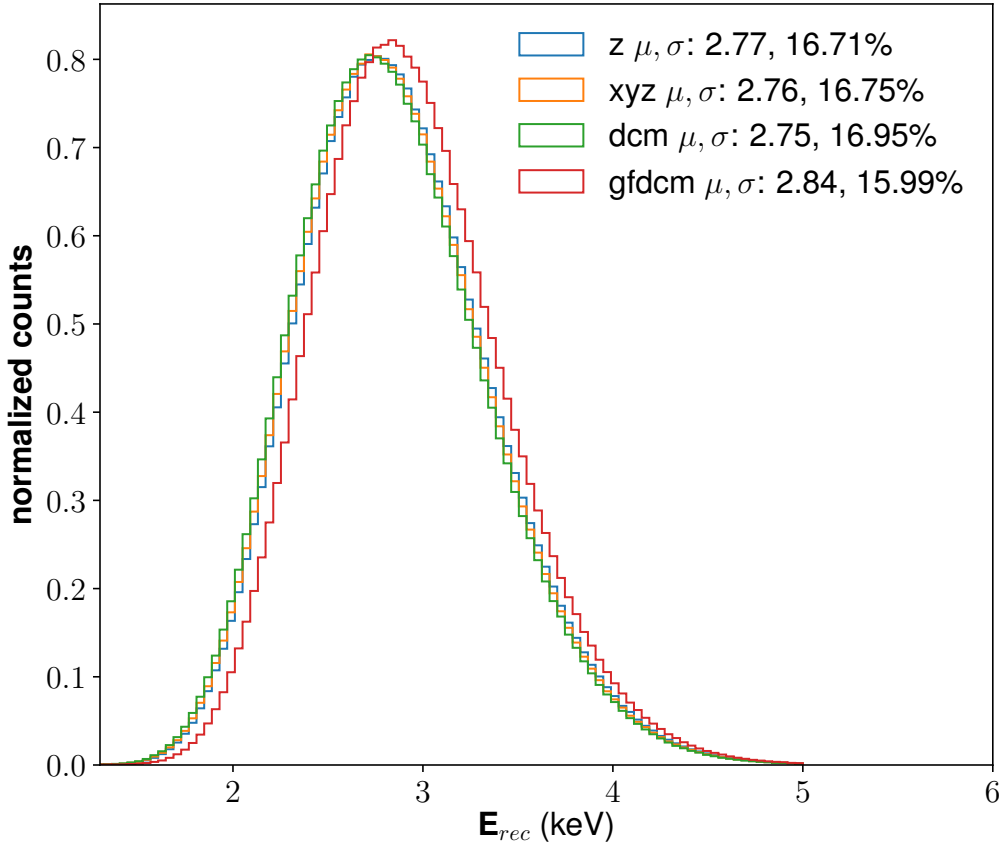


Figure 4.17: Reconstructed energy spectrum for the 2.8224 keV argon-37 spectrum. The  $\mu$  indicates the peak location and is in units of keV.  $\sigma$  indicates the width/energy of the spectrum.

of the drift time slices when fitting our line, and we allow both G1 and G2 to float. We do not include the argon-37 point in the fit because they are too close to threshold and are not expected to lie on the Doke-plot line.

The results of these fits are shown in figure 4.16. In this plot the lines labeled “z” and “xyz” are KrypCal corrections. The line labeled “dcm” is using the corrections derived in the previous two sections. The “dc” in “dcm” is shorthand for “Doke-corrected”, and the “m” indicates that the S1 and S2 averages in the various bins were calculated by arithmetic

mean. We also generated a set of corrections which fit a Gaussian peak to the S1 and S2 distributions in the individual bins, but the two methods yielded equivalent results, so we discarded the latter for the sake of simplicity.

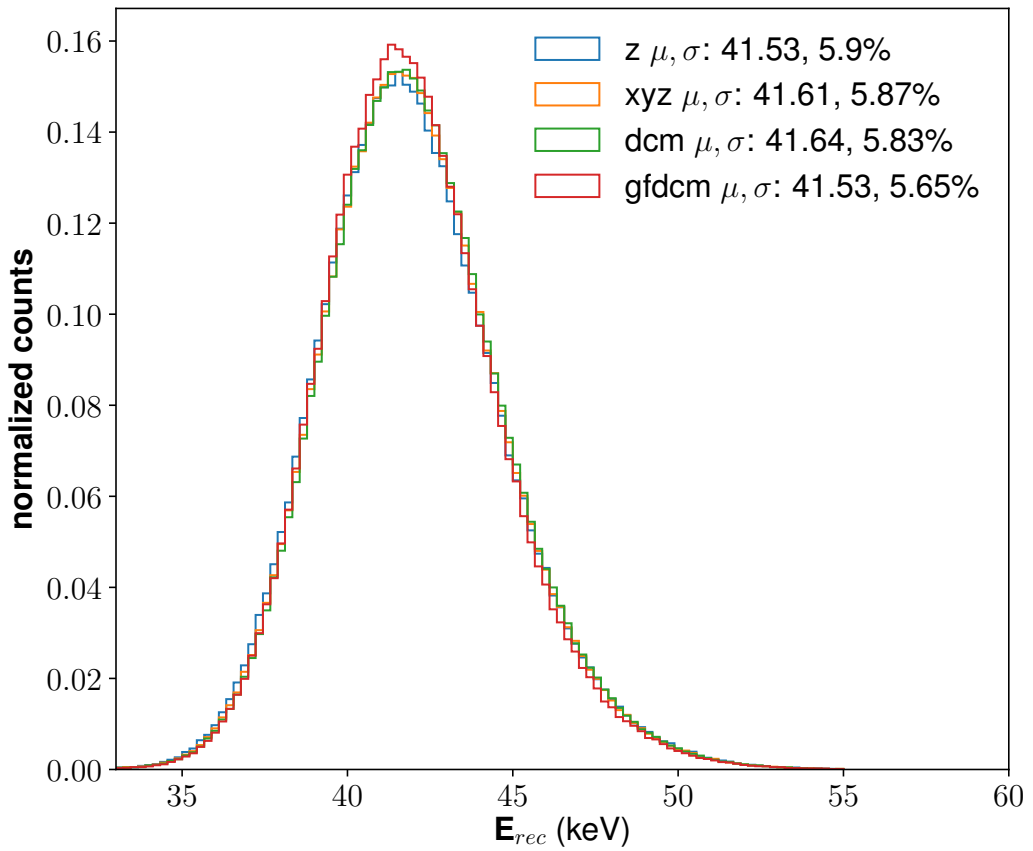


Figure 4.18: Reconstructed energy spectrum for the 41.5 keV krypton-83m spectrum. The  $\mu$  indicates the peak location and is in units of keV.  $\sigma$  indicates the width/energy of the spectrum.

The line in figure 4.16 labeled “gfdcm” also uses the corrections derived in the previous two sections. The difference between this data and the “dcm” data is that it uses a different measure of S2. The “dcm” data, along with “z” and “xyz”, uses the “pulse-finder” area as the measure of S2. This is just a raw sum of the S2 waveform. The “gfdcm” data uses the

area under a Gaussian function (hence the “gf”) which has been fit to the S2 waveform as the measure of S2 size.

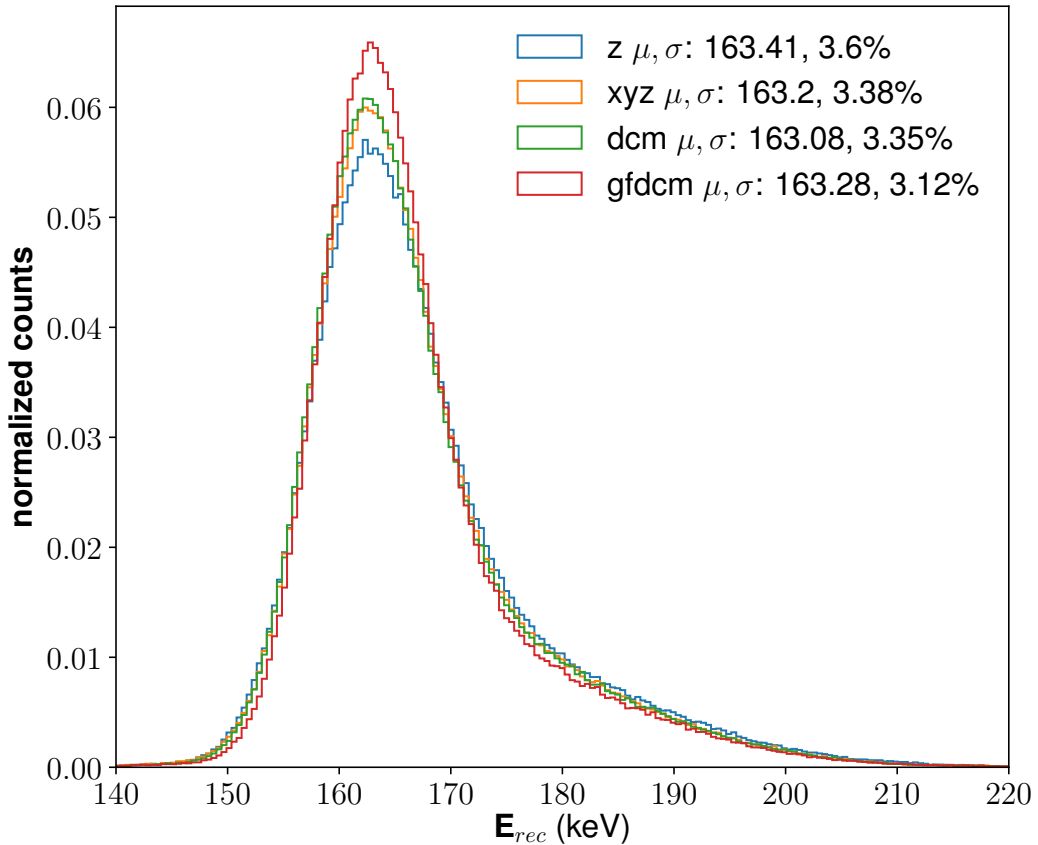


Figure 4.19: Reconstructed energy spectrum for the 163.93 keV xenon-131m spectrum. The  $\mu$  indicates the peak location and is in units of keV.  $\sigma$  indicates the width/energy of the spectrum.

The first observation we take from figure 4.16 is that there is a systematic variation in the argon-37 points, causing them to be “S” shaped. This effect is not present in the “dcm” or “gfdcm” plots, and so provides further evidence that the steep trend in the KrypCal S2 correction near the top of the detector does not represent a genuine efficiency effect. The argon-37 populations in the “z”, “xyz”, and “dcm” plots are also offset from the best fit

line. This is not entirely unexpected since the argon-37 S1 spectrum is bumping against threshold, although the size of the offset is larger than expected.

We use the G1 and G2 values taken from to generate reconstructed energy spectra for xenon-131m, krypton-83m, and argon-37. We find that “z”, “xyz”, and “dcm” generate a roughly equivalent energy spectrum for argon-37 and krypton-83m, both in the peak location and resolution. For xenon-131m, “dcm” and “xyz” are roughly equivalent and “z” produces a spectrum which is wider by about 7.5%.

Interestingly, the “gfdcm” corrections produce significantly narrower spectra than any of the others, for all three calibration lines. Additionally, it produces the only argon-37 spectrum whose energy is higher than the true value of 2.8224 keV. This is important because the reconstructed energy for argon-37 should be artificially high because the low energy side of the spectrum is hidden by threshold. Moving forward, we will focus on the following three corrections methods:

- “dcm”, because it produces ever-so-slightly better Doke plot and energy spectra than “z” and “xyz”
- “gfdcm”, because it produces the best energy spectra and Doke plot
- “z”, in order to be consistent with, and to create applicable results for existing LUX analysis

#### 4.4 Model of the Pathological S2 Tails

The energy spectra shown in figures 4.17, 4.18, and 4.19 all have a clear non-Gaussian tail toward high energy. These tails are propagated from a pathological effect in the S2 signals and are thought to be caused by the electron-trains described in section 2.2.3. The

S2 tails are present both during the LUX Run04 WIMP-search and in the post-Run04 calibration campaign.

We look for insight into this issue by comparing the S2 spectra of argon-37, xenon-131m, and krypton-83m at different drift times, as in figure 4.20. We find that the relative amplitude and slope of the tails do not change significantly at different energies or drift bins. From this we conclude that the tails will be approximately proportional to the initial S2 size. This is good news because it means that the combined energy model presented in section ?? will still be expected to hold. We also see from figure 4.21 that the shape and size of the argon-37 tails do not change when additional activity, in the form of krypton-83m events, is added to the detector.

To first order, the effect of the pathological tails will be absorbed into the measurement of G2. In calculations where the detector resolution are important, such as in the measurement of recombination fluctuations or when dealing with continuous energy spectra, a more nuanced understanding may be required. To this end, we aim to develop an empirical model which will allow us to estimate the systematic effects of this pathology.

The model of S2 tails will be implemented as an adjustment to the libNEST model by adding some random number of electrons to number of electrons extracted from the liquid. The expected value for the number of extracted electrons before the tail is added is given by:

$$\langle N_{e,extr} \rangle = \varepsilon N_e / C_{S2}(x, y, dT), \quad (4.5)$$

where  $\varepsilon$  is the extraction efficiency,  $C_{S2}(x, y, dT)$  is the efficiency correction for the event, and  $N_e$  is the number of electrons generated in the liquid. To simulate the effect of the S2 tails, we will alter  $N_{e,extr}$  to give  $N'_{e,extr}$ , which will then continue to propagate through the libNEST model as usual. The resulting S2 spectra generated will hopefully reproduce the shape of the S2 spectra we observe in data.

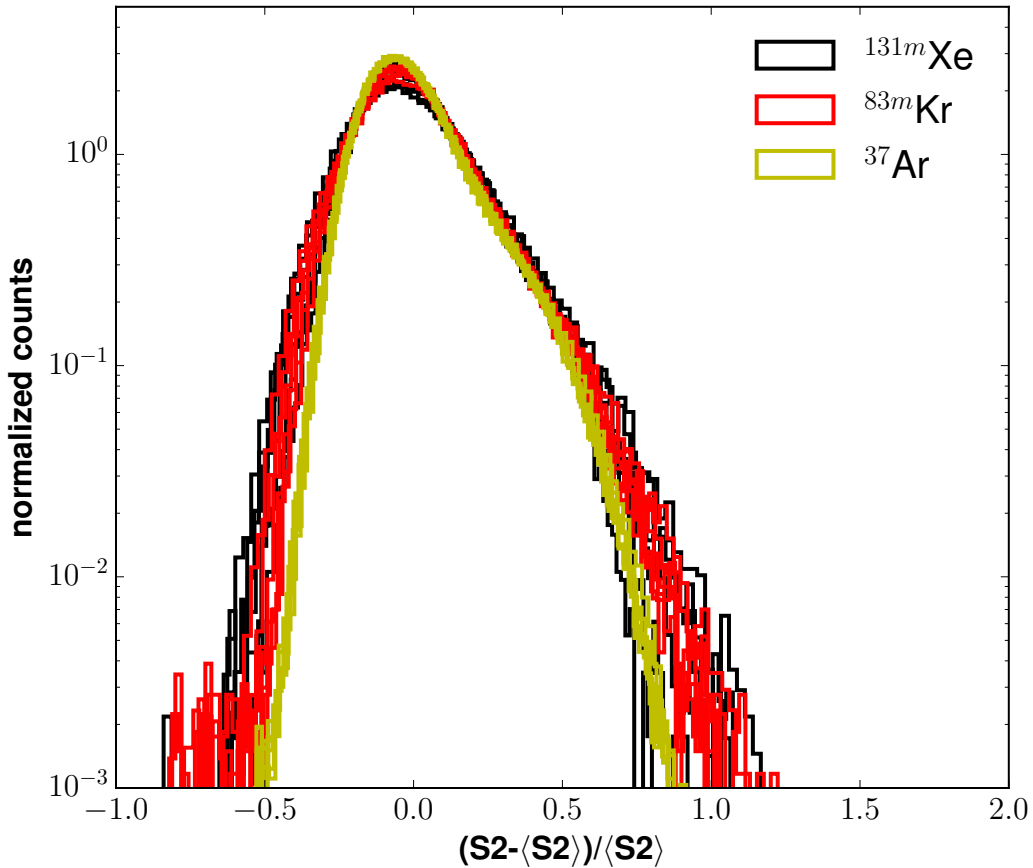


Figure 4.20: Mean-subtracted and normalized S2 spectra for argon-37, krypton-83m, and xenon-131m. The spectra are divided into 6 drift time bins from 40 to 310 microseconds. We see in this plot that the fractional size of the S2 tails is roughly constant in both energy and drift time.

We have a few observations in hand that help to motivate the development of a model of the S2 tails. First, it appears that not all events possess additional tail area, so we will try a model that assigns some probability,  $P_{tail}$ , that an event will be given additional area. We see from figure 4.20 that the size of the tails approximately follows an exponential distribution, and that the amplitude of the distribution is roughly proportional to the S2 size. With these observations we develop the model of S2 tails as follows:

1. Generate a random test variable,  $T$ , uniformly distributed between 0 and 1.

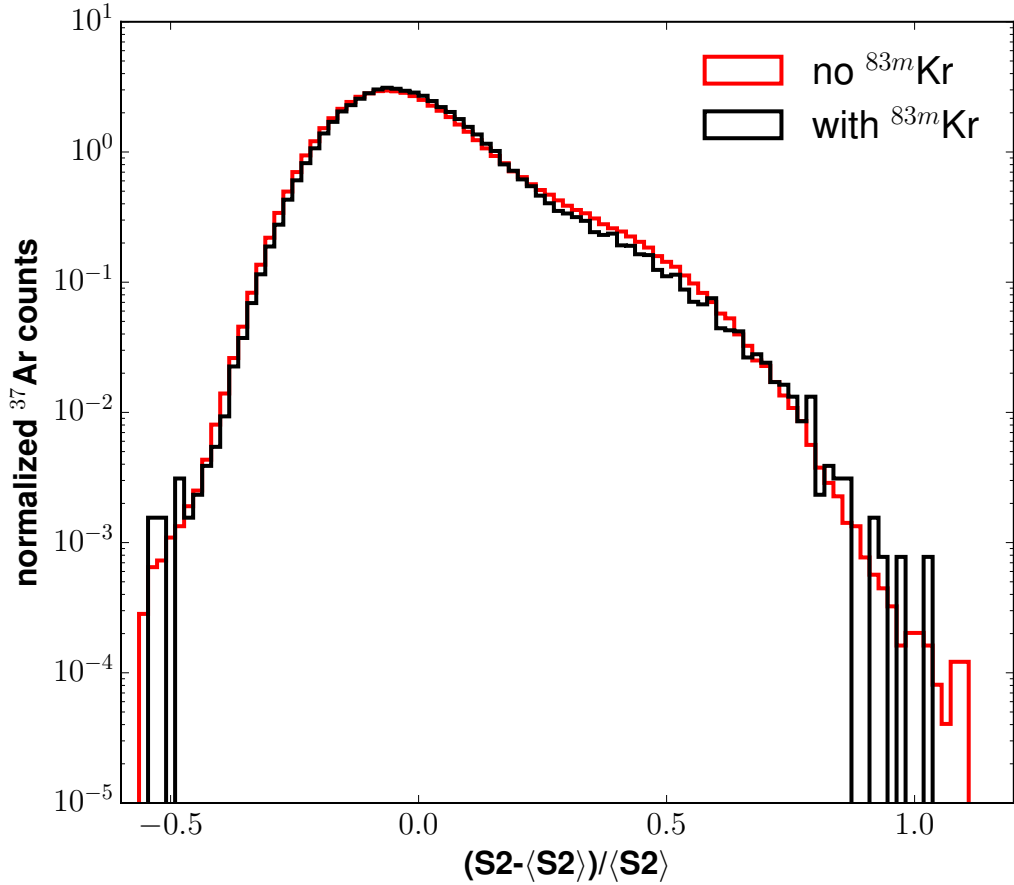


Figure 4.21: Mean-subtracted and normalized S2 spectra for argon-37. We show the spectrum both during a krypton-83m calibration (black), and when no additional activity is present (red).

2. If  $T > P_{tail}$ , we set  $N'_{e,extr} = N_{e,extr}$
3. If  $T \leq P_{tail}$ , we draw another random number  $n_{tail}$  from an exponential distribution whose mean is equal to  $b_{tail}$ . We then set  $N'_{e,extr} = N_{e,extr}(1 + n_{tail})$ .

This model is then dependent on three parameters,  $P_{tail}$ ,  $b_{tail}$ , and the “true” value of G2, which needs to be input into the libNEST model. The G2 values as measured in figure 4.16 will artificially high because of the pathological S2 area added by the tails. By varying these three parameters, we can optimize the model until it reproduces the observed energy

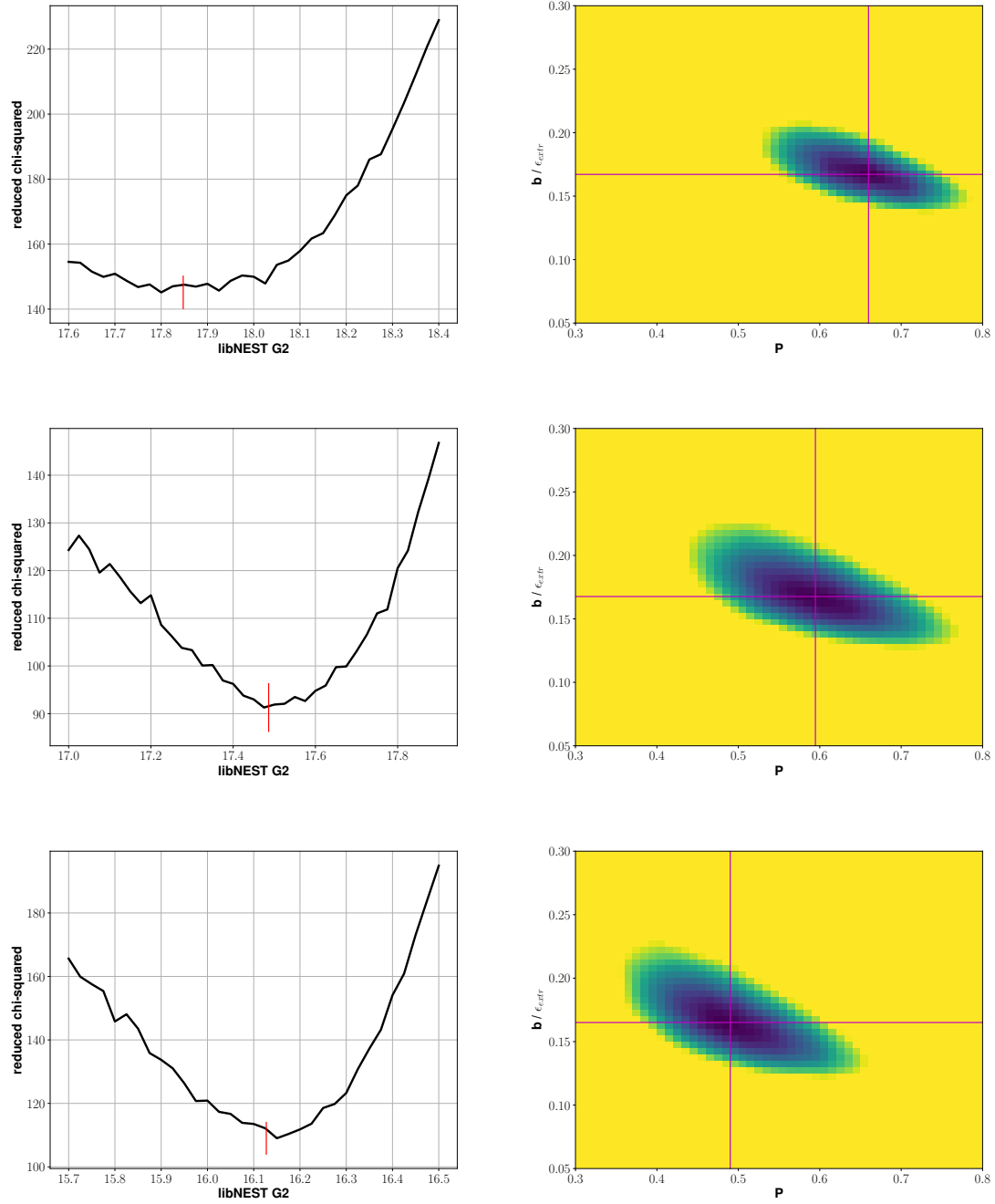


Figure 4.22: Best fit results for the tail model for “z” (top), “dcm” (middle), and “gfdcm” (bottom) corrected data. The red and magenta lines indicate the best fit values calculated using the Metropolis algorithm.

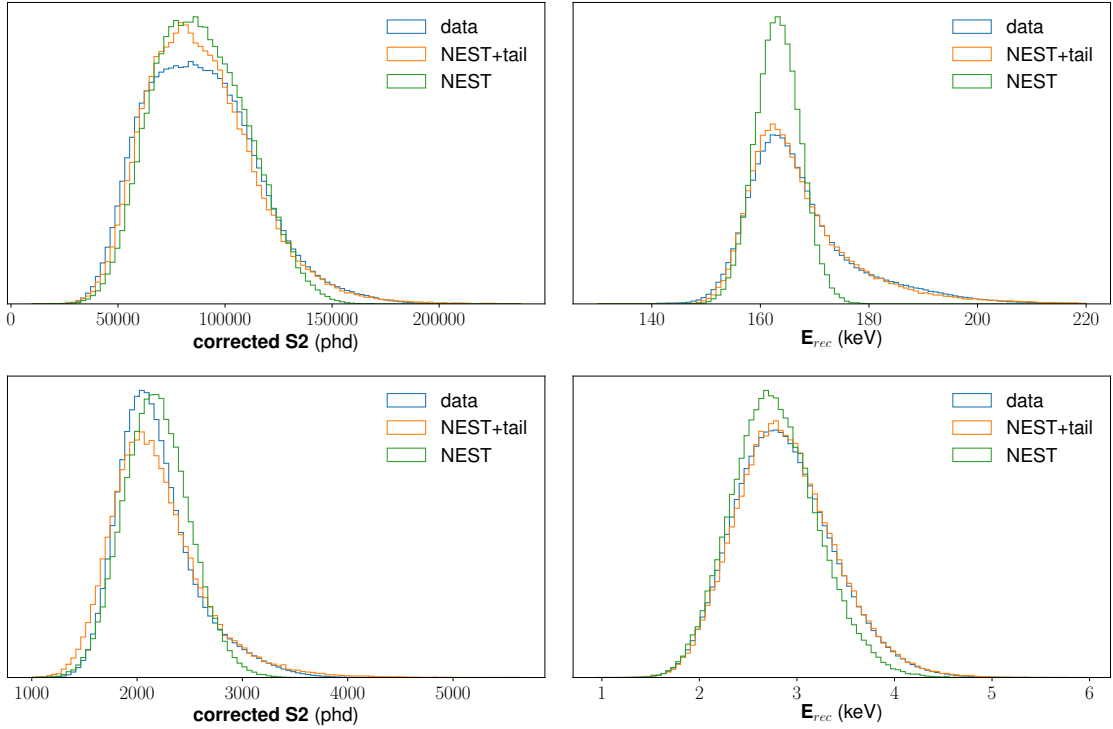


Figure 4.23: Best-fit spectra for “z” corrected data. The top plots are for the xenon-131m data, and the lower plots are for the argon-37 data. The green histogram, labeled “NEST”, is the libNEST simulation with no S2 tail model added. The orange histogram, labeled “NEST+tail” is the libNEST model, plus the model of the S2 tails described in this section. The blue histogram shows what is observed in data. The spectra are calculated for 50 to 300 microseconds drift time.

spectra.

We use our argon-37 and xenon-131m spectra as reference, calculating the  $\chi^2$  difference between the libNEST S2 and reconstructed energy spectra, and those measured in data. We first scan across the parameters to locate the approximate location of the optimal parameters. This grid scan uses a modified model for computational convenience. Instead of adding the tail area to to  $N_{e,extr}$ , we add it to the final S2 area. Since this modified is applied after the extraction efficiency is modeled, the fractional tail area,  $n_{S2,tail}$  will be drawn from an exponential distribution with a mean of  $b_{tail}/\epsilon$ .

After the grid scan locates the approximate minimum, we then apply the Metropolis

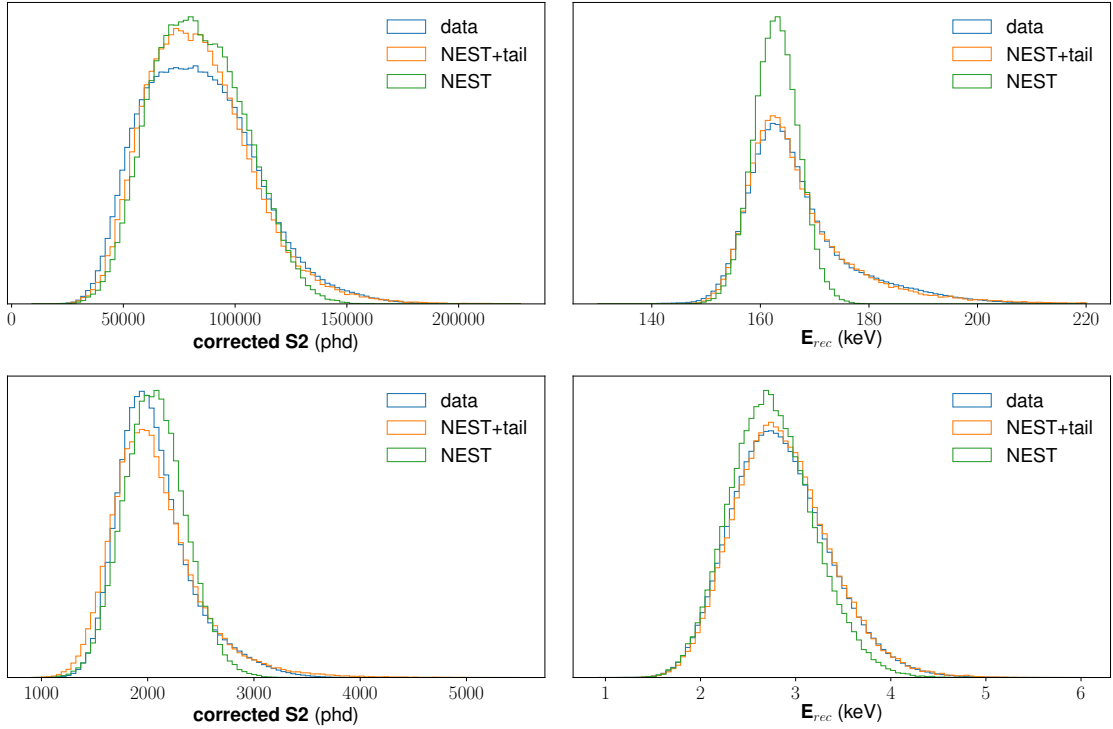


Figure 4.24: Best-fit spectra for “dcm” corrected data. The top plots are for the xenon-131m data, and the lower plots are for the argon-37 data. The green histogram, labeled “NEST”, is the libNEST simulation with no S2 tail model added. The orange histogram, labeled “NEST+tail” is the libNEST model, plus the model of the S2 tails described in this section. The blue histogram shows what is observed in data. The spectra are calculated for 50 to 300 microseconds drift time.

algorithm to fine tune the fit[2, 48]. For this algorithm, we use the model as we initially described it. For each iteration, we draw a new set test parameters from a normal distribution centered at the values of the previous iteration. These normal distributions have standard deviations of 0.005 for  $b_{tail}$ , 0.01 for  $P_{tail}$ , and 0.05 for  $G2_{true}$ . We then accept the new values of the parameters with a probability of  $P_{accept} = \min(1, \exp(-(\chi_i^2 - \chi_{i-1}^2)/2))$ . We run at least 1000 iterations and allow for a burn-in period of 200 iterations. We take the best-fit values of the parameters to be equal mean of the iterations excluding the burn-in period.

We apply this fitting method to the three corrections methods we are testing; “z”, “dcm”,

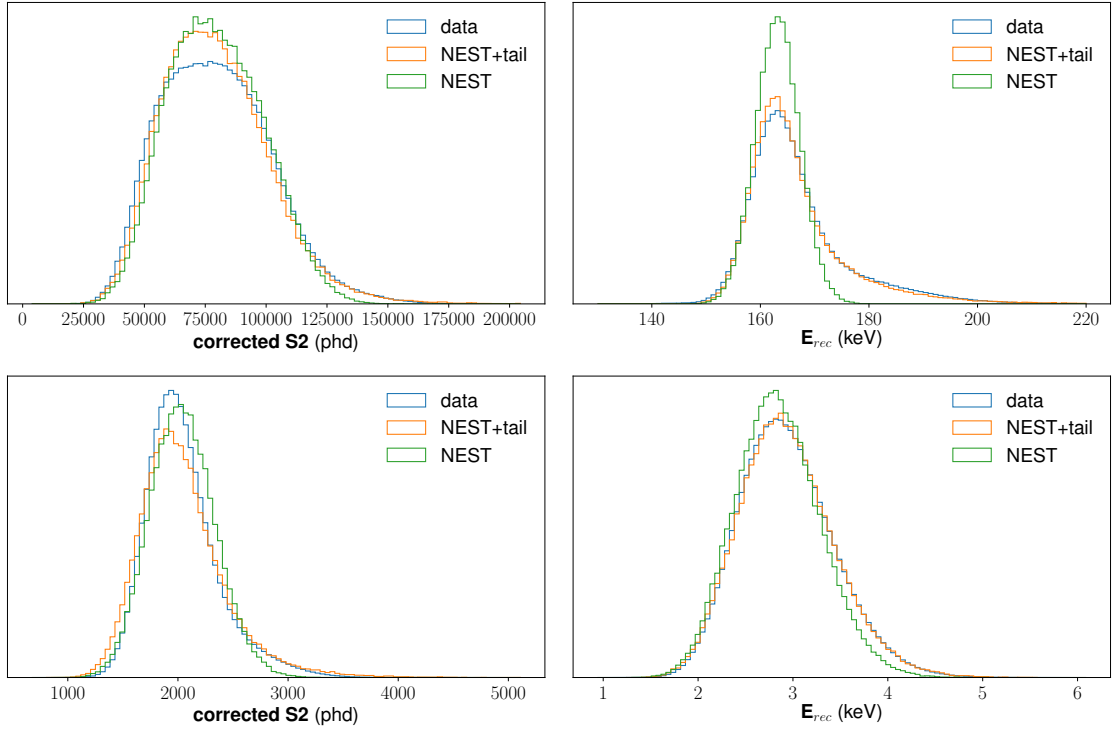


Figure 4.25: Best-fit spectra for “gfdcm” corrected data. The top plots are for the xenon-131m data, and the lower plots are for the argon-37 data. The green histogram, labeled “NEST”, is the libNEST simulation with no S2 tail model added. The orange histogram, labeled “NEST+tail” is the libNEST model, plus the model of the S2 tails described in this section. The blue histogram shows what is observed in data. The spectra are calculated for 50 to 300 microseconds drift time.

Correction	$b_{tail}$	$\pm$	$P_{tail}$	$\pm$	$G2_{true}$	$\pm$
z	0.112	0.003	0.73	0.02	17.6	0.05
dcm	0.116	0.004	0.63	0.02	17.36	0.04
gfdcm	0.109	0.004	0.53	0.02	16.02	0.03

Table 4.2: Best fit results for the S2 tail model.

and “gfdcm”. The results of the fit are shown in figure 4.22, as well as in table 4.2. The data and NEST+tail energy histograms are in good agreement, indicating that our tail model is successful. There is some disagreement in the S2 spectra near the peak value. This is likely explained by incorrect values for the input recombination fluctuations. We will aim to better measure this input value in the next chapter.

## Chapter 5: Detector Response to $^{14}\text{C}$ Beta Decay

The carbon-14 calibration follows the same preparation and injection procedure as the tritium calibration, which has been described in previous papers[7, 23, 38]. Both of these calibration sources have half-lives greater than the lifetime of the experiment, so we rely on the LUX gas processing system to chemically remove the injected activity. We have previously characterized our ability to remove radio-labelled methane from the LUX detector and found that tritiated-methane ( $\text{CH}_3\text{T}$ ) is removed with a decay time of about 7-10 hours, leaving no observed residual activity in the detector. Carbon-14 labelled methane ( $^{14}\text{CH}_4$ ) is chemically identical to  $\text{CH}_3\text{T}$  and so we find it to have the same removal characteristics. The tritiated methane is removed with a time constant of 8.2 hours, and the carbon-14 labeled methane is removed with a time constant 9.1 hours. This variation in removal time is within reason given the variation in previous trials with tritiated methane.

The endpoint of the carbon-14 spectrum is obscured by the xenon-131m line. We do not assume that gammas and betas behave in the same way in liquid xenon, so we need to cut out the xenon-131m events in order to measure the energy deposition properties of carbon-14. At 145 keV, the xenon distribution falls to less than 5% of the carbon-14 distribution, so we will only include events with reconstructed energy  $< 145$  keV in our measurement of the carbon-14 yields and recombination..

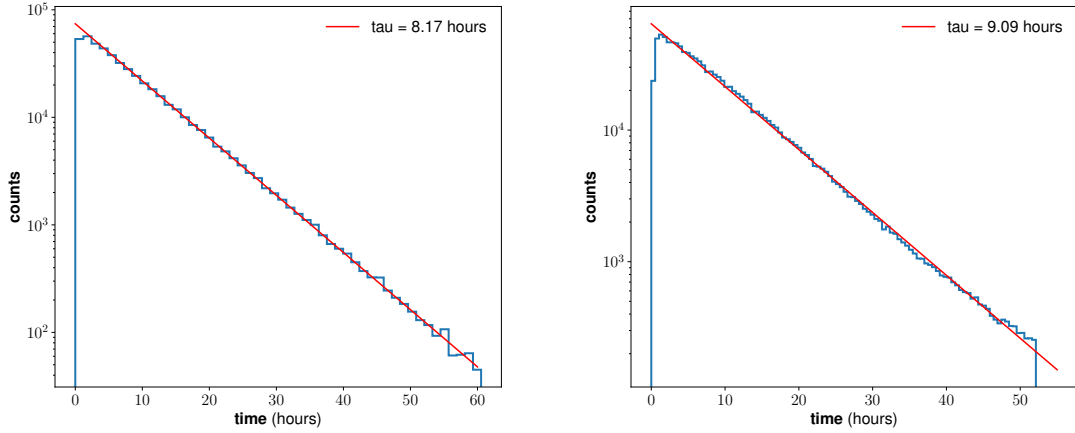


Figure 5.1: Purification of methane radio-labeled with tritium (left), and carbon-14 (right). The tritiated methane is removed with a time constant of 8.2 hours, and the carbon-14 labeled methane is removed with a time constant 9.1 hours.

## 5.1 The Theoretical $^{14}\text{C}$ Beta-Spectrum

The shape of the theoretical spectrum of the carbon-14 beta decay has been of interest in the context neutrino mass experiments[65], where the goal is to measure the precise endpoint, and in liquid scintillator experiments, which have  $^{14}\text{C}$  as a major background and so need to model the spectrum with high precision[9, 12]. This decay also is of interest in theoretical nuclear physics because it has an abnormally long half life[31, 32, 40]. The transition of  $^{14}\text{C}$  to the ground state of  $^{14}\text{N}$  is an allowed Gamow-Teller ( $0^+ \rightarrow 1^+$ ) transition. The 5730 year half-life, and corresponding comparative half life,  $\log_{10}(f_t) = 9.04$ , makes it empirically consistent with second-forbidden transitions[40, 65].

This extended half life indicates an anomalously small Gamow-Teller nuclear matrix element of  $\langle GT \rangle \approx 2 \times 10^{-3}$ . This points to cancellation in the lowest order terms of the nuclear matrix element and means that higher order terms must be taken into consideration. These higher-order terms may introduce momentum-dependent deviations from the allowed spectral shape. There have been several experiments[9, 12, 40, 59, 65] which have

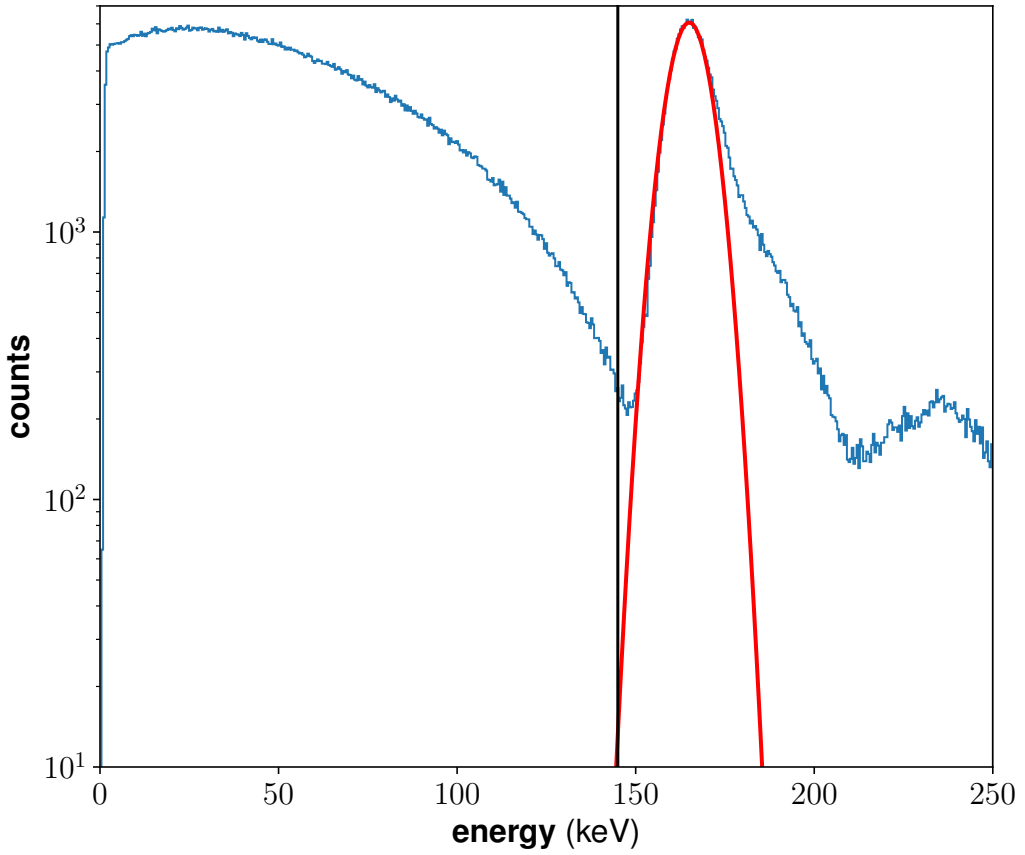


Figure 5.2: Reconstructed energy spectrum of the carbon-14 calibration. The blue histogram was generated using all of the events in the dataset, including both carbon-14 and Xe-131m. Most of the events are in the smooth carbon-14 beta spectrum, which extends from 0 to 156 keV, but the Xe-131m line is clearly visible at 164 keV. The red curve shows a Gaussian fit to the xenon-131m spectrum, excluding the high energy side. The black line shows our energy cut at 145 keV.

made measurements of the spectral shape which are consistent with non-statistical corrections to the allowed shape. These results are in some tension with each other, as well as with previous measurements which show a purely allowed spectral shape[50].

### 5.1.1 The Allowed Spectrum

Carbon-14 decays to the ground state of nitrogen-14 by way of an allowed Gamow-Teller,  $0^+$  to  $1^+$  transition. This decay has a Q-value of 156 keV and a half life of 5730 years. In general, the theoretical spectrum for this decay takes the form[40]:

$$\frac{dN}{dE} = \frac{1}{2\pi^3} \xi C(E) F(Z, E) pE(E_0 - E)^2 \quad (5.1)$$

Here,  $p$  and  $E$  are the momentum and total energy of the emitted beta, and  $E_0$  is the endpoint energy of the spectrum. In equation 5.1 we have neglected the neutrino mass as well as a radiative correction term which is expected to have  $< 1\%$  effect on the shape of the spectrum[65]. The initial distribution of momentum between the electron and neutrino is proportional to  $pE(E_0 - E)^2$ . This is derived by the phase space density of free particles and will be referred to as the phase space factor. The Fermi function  $F(Z, E)$  contains information about the interaction between the emitted beta and the daughter nucleus. The terms  $\xi$  and  $C(E)$  represent the energy independent and energy independent parts of the nuclear matrix element.

### 5.1.2 The Fermi Function

As the emitted beta travels away from the daughter nucleus, the two interact and either increase or decrease the momentum of the beta, depending on its charge. In the case of  $^{14}C$ , the beta has a negative charge and has to climb up out of the electric potential created by the  $^{14}N$  daughter nucleus. The resulting observed beta spectrum will then be pulled to lower energy than the initial phase space factor. This modification to the spectrum if known as the Fermi function,  $F(Z, E)$ . The traditional derivation of  $F(Z, E)$  begins by assuming the daughter nucleus is a fixed point charge and then evaluates the electron wave-function

given the resulting field. The wave function is only evaluated down to the nuclear radius,  $R$ , in order to avoid divergence[66]:

$$F(Z, E) = 2(\gamma + 1)\Gamma(2\gamma + 1)^{-2}(2pR)^{2(\gamma - 1)}e^{\pi\alpha ZE/p}|\Gamma(\gamma + i\alpha ZE/p)^2|^2 \quad (5.2)$$

There is also a much simpler closed-form solution in the low-Z, non-relativistic approximation[62]:

$$F_{NR}(Z, E) = \frac{x}{1 - \exp(-x)}, \quad (5.3)$$

where  $x = 2\pi Ze^2/\hbar v$ . Here,  $Z$  is the atomic number of the daughter nucleus,  $e$  is the electron charge, and  $v$  is the final velocity of the beta particle.

Electrons in the higher-momentum part of the spectrum will have velocities exceeding  $0.5c$ , so the non-relativistic approximation may not hold. This being the case, we consider the Bethe-Bacher approximation, which estimates the relativistic correction[15, 62]:

$$F_{BB}(Z, E) = F_{NR}(Z, E)[W^2(1 + 4\gamma^2) - 1]^S, \quad (5.4)$$

where  $W \equiv E/m_e c^2$ ,  $\gamma \equiv \alpha Z$ , and  $S \equiv (1 - \gamma^2)^{1/2} - 1$ . The full relativistic Fermi function can be estimated by a series expansion on powers of  $(\alpha Z)$ [65, 66]. This sum is of limited use to us here because it becomes invalid at low kinetic energy and in fact diverges at zero.

The final correction to the Fermi function we consider is the correction for screening of the Coulomb potential by the orbital electrons. This essentially amounts to a shift in the origin of  $F(Z, E)$ [26, 65]:

$$F_S(Z, E) = \frac{E' p'}{Ep} F(Z, E'), \quad (5.5)$$

where  $E' = E - V_0$  and  $p'$  is the associated momentum. For the  $^{14}\text{C}$  beta decay,  $V_0 = 495\text{eV}$ [65].

Figure 5.3 compares the non-relativistic approximation to the various corrections described in this section. We can see that the Wilkinson expansion differs from  $F_{NR}(7, E)$  by less than a percent down to a few eV, at which point it diverges. The Bethe-Bacher approximation is similarly very close to  $F_{NR}(7, E)$ , but it does not display the same pathological behavior at the origin. The correction for electron screening peaks at 1.5% at a kinetic energy of  $T = 3.5\text{keV}$ . Because of the pathology in the Wilkinson expansion, we will take our Fermi function to be the combination of equations 5.4 and 5.5:

$$F(Z, E) = \frac{E' p'}{E p} F_{NR}(Z, E') [(E'/m_e c^2)^2 (1 + 4\gamma^2) - 1]^S, \quad (5.6)$$

with  $F_{NR}(Z, E)$  as defined in equation 5.3 and  $E'$  and  $p'$  as defined for eqaution 5.5.

### 5.1.3 The Shape Factor

For a typical allowed decay, the shape factor is dominated by interference between the Gammow-Teller axial matrix element,  $\langle GT \rangle$  and the weak magnetism matrix element,  $\langle WM \rangle$ . Such a shape factor has the form[17, 31, 40, 65]:

$$C(E) \approx 1 + \frac{4}{3M} \frac{\langle WM \rangle}{\langle GT \rangle} [E - E_0/2 - m_e^2/E], \quad (5.7)$$

where  $M$  is the nucleon mass,  $m_e$  is the electron mass, and  $E_0$  is the endpoint energy of the beta-spectrum. Usually the energy dependence of  $C(E)$  is small enough that it can be neglected, but in the  $^{14}\text{C}$  beta decay the suppressed decay rate means that  $\langle GT \rangle$  is small enough to make its consideration necessary. Under the conserved vector current hypothesis (CVC), the weak magnetism matrix element can be analogized to that of an M1 electromagnetic transition ( $\langle WM \rangle = \langle M1 \rangle$ ) for the purpose of calculating the expected shape factor. The ground state of  $^{14}\text{C}$  is an element of an isospin triplet, together with the  $^{14}\text{O}$  ground

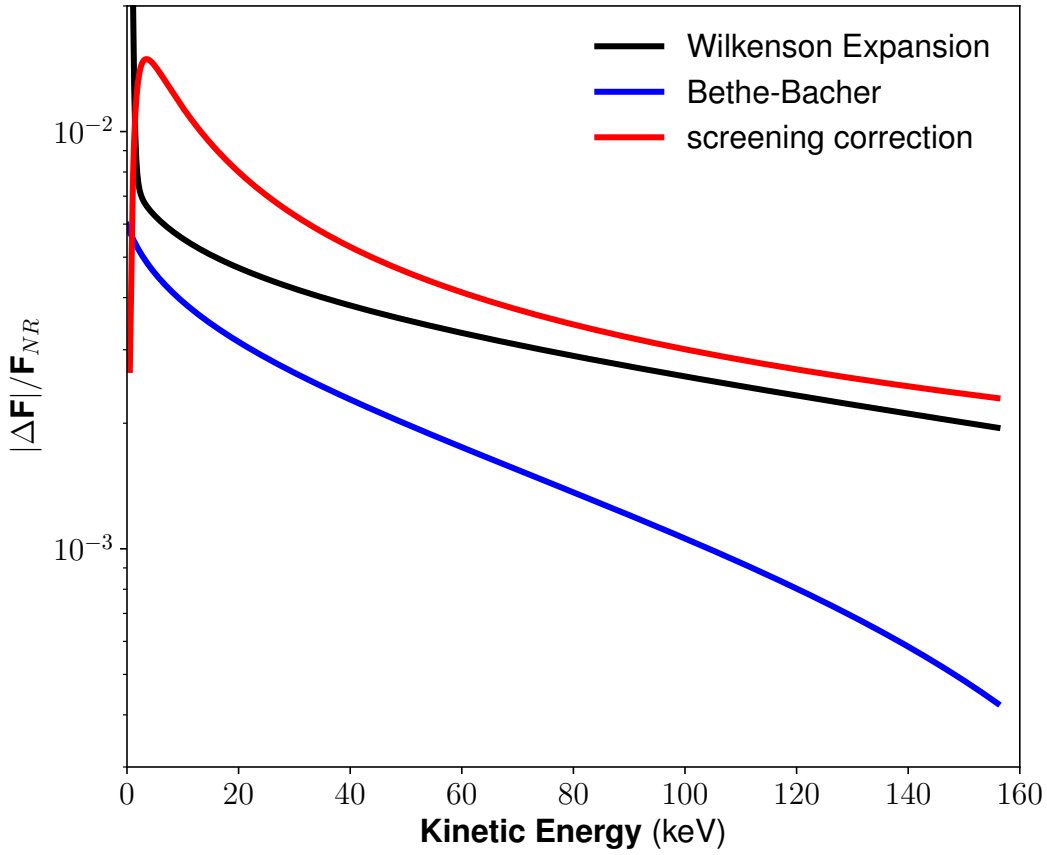


Figure 5.3: Correction factors for the  $^{14}\text{C}$  beta Fermi function. We compare the non-relativistic approximation,  $F_{NR}(7, E)$  to the relativistic corrections described in section 5.1.2, as well as the non-relativistic function after having been adjusted to account for screening by the orbital electrons. Plotted is  $|F'(7, E) - F_{NR}(7, E)|/F_{NR}(7, E)$ , where  $F'(7, E)$  are the adjusted Fermi functions as indicated in the legend.

state and the first excited state of  $^{14}\text{N}$ . The M1 transition is the same as that of the first excited state of  $^{14}\text{N}$  transitioning to the ground state.

There have been several calculations of the predicted shape factor[31, 32, 65]. These typically use a more general form of the  $C(E)$  which takes into account terms which have

been neglected from equation 5.7:

$$C(E) = 1 + aE + \mu_1 \gamma_1 b/E + cE^2, \quad (5.8)$$

where  $\gamma_1 = [1 + (\alpha Z)^2]^{1/2}$  and  $\mu_1$  is a special Coulomb function. The coefficients  $a$ ,  $b$ , and  $c$  can be calculated using the appropriate matrix elements. The matrix elements are typically calculated using model wave functions for the  $^{14}\text{C}$  and  $^{14}\text{N}$  ground states.

The first measurement of the  $^{14}\text{C}$  shape factor was made by Sonntag et. al. in 1970[59]. In units of MeV, his measured shape factor was,  $C(E) = 1 - 9.14E + 1.53/E + 7.66E^2$ . Genz et. al.[32] used this result in part to derive phenomenological wave functions which replicate the shape factor. Later experiments and theoretical calculations have rejected this shape factor.

Wietfeldt et. al. found their data to be consistent with a shape factor of  $C(E) = 1 + aE$ , with  $a = -0.45 \text{ MeV}^{-1}$ [65]. This result is very close to their own theoretical calculation of  $a = -0.38 \pm 0.04 \text{ MeV}^{-1}$ , along with theoretical calculations by Garcia and Brown[31], and Calaprice and Holstein[17]. However, the best-fit value of  $a$  was inconsistent depending on what range of energies was fit, and a second measurement of the spectrum 2 years later yielded a best fit parameter of  $a = -0.63 \pm 0.05 \text{ MeV}^{-1}$ .

The Borexino collaboration attempted to measure the shape of the  $^{14}\text{C}$  beta spectrum using their counting test facility (CTF). They assumed the same functional form as the Wietfeldt paper and excluded all  $a < -0.72 \text{ MeV}^{-1}$  with 90% confidence[9].

Most recently, V. Kuzminov and N. Osetrova measured the shape factor of the  $^{14}\text{C}$  beta decay using a wall-less proportional counter[40]. They assumed a shape factor with the form,  $C(E) = 1 + \beta(Q - T)$ , with  $Q$  being the endpoint energy and  $T$  being the kinetic energy of the electron. They measured  $\beta = 1.24 \pm 0.04 \text{ MeV}^{-1}$ , which is in agreement with a theoretical calculation by Genz et. al.[32]. This result is equivalent to  $a =$

$-0.68 \pm 0.02$  MeV $^{-1}$  in a Wietfeldt-style shape factor and is very close to both the Borexino measured limit, as well as the second Wietfeldt measurement.

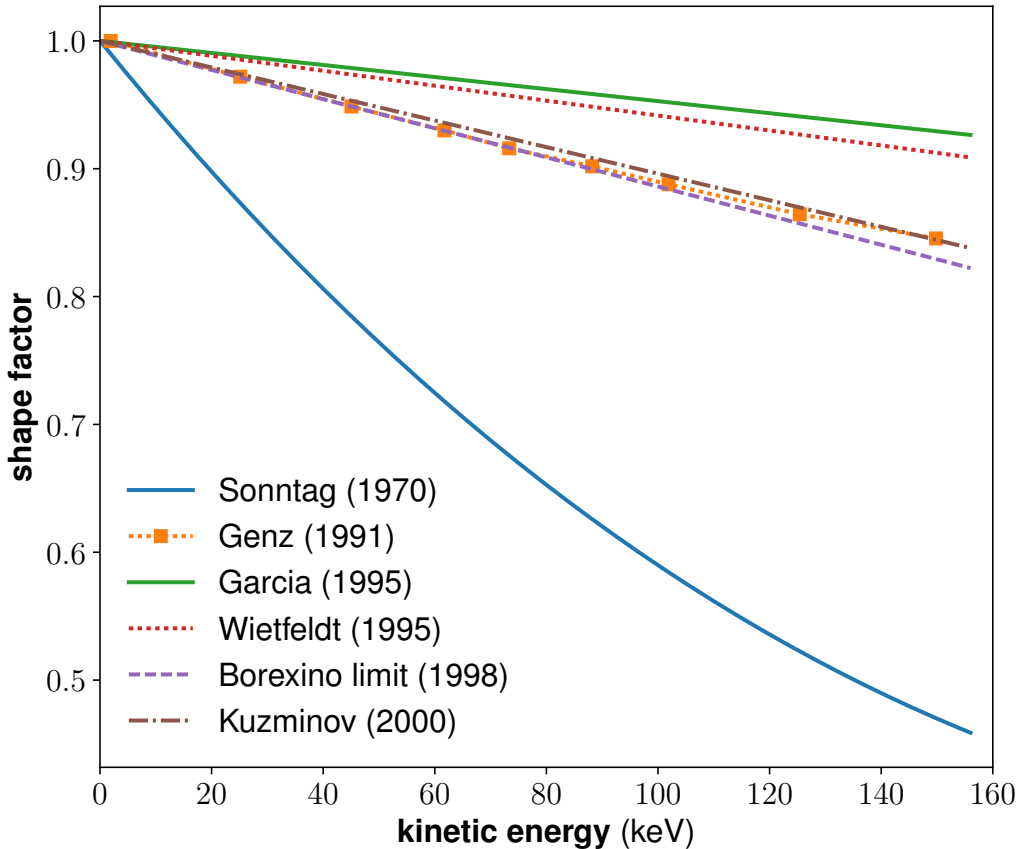


Figure 5.4: Various measurements and theoretical calculations of the  $^{14}\text{C}$  shape factor. They have all been normalized to equal 1 at kinetic energy=0 keV. The Sonntag[59], Wietfeldt[65], Borexino[9], and Kuzminov[40] lines are all experimental measurements, while the Genz[32] and Garcia[31] lines are theoretical calculations. It is clear that the Sonntag result is strongly disfavored by all subsequent experiments and theoretical calculations. This figure also shows Genz, Borexino, Kuzminov, as well as the second Wietfeldt result (not shown) all converging around  $C(E) \approx 1 - (0.7 \text{ MeV}^{-1})E$ . It would be difficult, however, to claim this as consensus because the only true measurement in this subset is the Kuzminov line. Neither the Borexino paper nor the Wietfeldt paper claim a strong measurement of the shape factor.

## 5.2 Preliminary Measurement of Light and Charge Yields

The carbon-14 injection was based on the tritium calibration, which was first performed in August of 2013, after the first LUX data run was completed. The data from this calibration was used to calculate the energy deposition properties of electronic recoils in liquid xenon. To this end, a method was developed by Attila Dobi which deconvolved the effects of detector-resolution from the interesting physics involved in the process[7, 23].

Unfortunately this method, which we will refer to as the Dobi method, is largely irrelevant to the post-Run04 data. It relies on a robust understanding of the detector resolution and uses a Gaussian model of the energy smearing to obtain the necessary corrections. The S2 tails described in section 4.4 were not present in the LUX Run03 data and mean both that our understanding of the energy-dependent detector resolution is limited and that the Gaussian model will not apply. To address these issues, we will develop a numerical version of the Dobi method using our modified version of libNEST which includes the empirical model of the S2 tails.

### 5.2.1 Accounting for Gaussian Smearing of Continuous Beta Spectra

This deconvolution of detector resolution is necessary because of the continuous nature of beta spectra. We do not know the true deposition energy,  $E_{true}$ , of any given event and therefore only have access to the reconstructed energy,  $E_{rec}$ . In the Run03 measurements, the reconstructed energy of any event would be drawn from a Gaussian distribution centered at the true deposition energy, with the width of this distribution being the energy resolution,  $\sigma_E$ .

When this Gaussian smearing is applied to a continuous spectrum with a non-zero slope, it will create a systematic offset the measured reconstructed energy from the true energy. We take the spectrum shown in figure 5.5 as an example. The true energy of the events

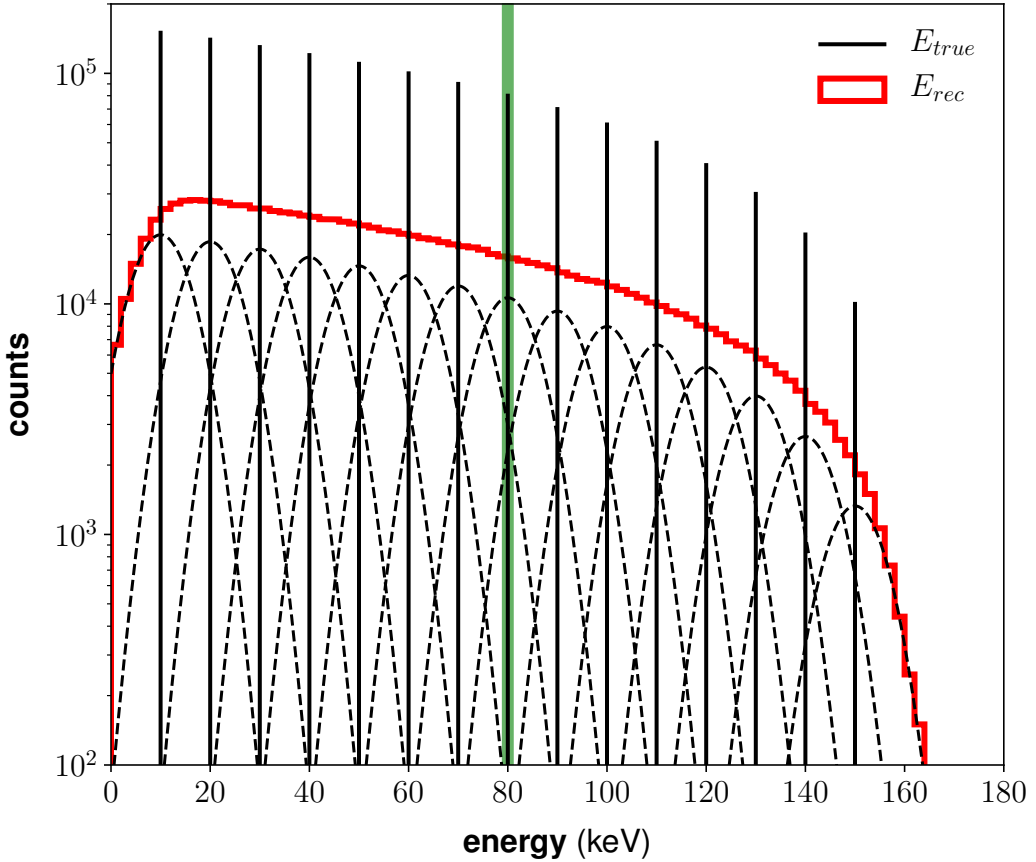


Figure 5.5: Smearing of a discrete, linearly falling spectrum. The true energy of the events is distributed at  $(10, 20, 30, \dots, 150)$  keV, as indicated by the solid black lines. The number of events at each energy decreases linearly. We then apply Gaussian smearing with a flat resolution of 6 keV to the true energy (dashed lines). The reconstructed energy (red histogram) shows the resulting spectrum. The average true energy of events in a slice from  $79.75 \text{ keV} < E_{rec} < 80.25 \text{ keV}$  (green area) is  $70.65 \pm 0.09$  keV. This average is offset from the selected energy due to smearing.

is distributed at discrete energies, 10, 20, 30, up to 150 keV. We apply Gaussian smearing with a constant resolution of  $\sigma_E = 6$  keV to give us our reconstructed energy spectrum. When we take a small slice in reconstructed energy, from 79.75 to 80.25 keV, we find that the average true energy of events in this slice is systematically offset to  $79.53 \pm 0.09$  keV. This offset is due to the negative slope of the true energy spectrum. The lower energy bins

are more prominent than the higher energy ones, and therefore will have more events smear into our reconstructed energy slice.

It is possible to calculate this offset explicitly by integrating the contribution from each individual Gaussian. The number of events contributed to our reconstructed energy slice by the  $i^{th}$  true energy bin will be given by:

$$\begin{aligned} A_i &= \int_{79.75}^{80.25} dx \frac{N_i}{\sqrt{2\pi\sigma_E^2}} e^{-(x-E_{true,i})^2/2\sigma_E^2} \\ &= \frac{N_i}{2} \left( \operatorname{erf}\left(\frac{80.25 - E_{true,i}}{\sqrt{2\sigma_E^2}}\right) - \operatorname{erf}\left(\frac{79.75 - E_{true,i}}{\sqrt{2\sigma_E^2}}\right) \right) \end{aligned} \quad (5.9)$$

where,  $N_i = C(16 - i)$  is the number of events in the  $i^{th}$  bin, and  $C$  is a scaling constant. The expected mean true energy,  $v_{slice}$ , of events in the slice will then be given by:

$$v_{80} = \frac{\sum_i E_{true,i} A_i}{\sum_i A_i} \quad (5.10)$$

For the stated values of  $N_i$ ,  $E_{true,i}$ , and  $\sigma_E$ , equation ?? yields  $v_{80} = 79.56$  keV, which is consistent with the result found in the previous paragraph.

Equation ?? can be used to recenter an arbitrary reconstructed energy bin. This correction will be most important for energy regions where the spectrum in question is steeply changing and at its endpoints. For instance, if we take a reconstructed energy slice of our toy spectrum from 149.75 to 150.25 keV, the predicted low-energy bias goes from 0.44 keV as it was for the 80 keV slice, to 3.5 keV. This prediction is consistent with the measured bias of  $3.4 \pm 0.2$  keV.

We can generalize equations 5.9 and 5.10 to apply to decays with continuous energy spectra. If the energy resolution of the detector,  $\sigma_E(E)$ , and the shape of the spectrum,  $\frac{dN}{dE}$ ,

are both known, equations 5.9 and 5.10 can be rewritten:

$$A(B_1, B_2) = \frac{1}{2} \frac{dN}{dE} \left( \operatorname{erf}\left(\frac{B_2 - E}{\sqrt{2\sigma_E(E)^2}}\right) - \operatorname{erf}\left(\frac{B_1 - E}{\sqrt{2\sigma_E(E)^2}}\right) \right), \quad (5.11)$$

and:

$$v(B_1, B_2) = \frac{\int A(B_1, B_2) E dE}{\int A(B_1, B_2) dE}, \quad (5.12)$$

where  $B_1$  and  $B_2$  are the edges of the reconstructed energy slice. The calculated  $v(B_1, B_2)$  can then be used to recenter the arbitrary reconstructed energy bin to the average true energy of events in that bin.

### 5.2.2 Accounting for Non-Gaussian Smearing

The results from the previous section, shown in equations 5.11 and 5.12 provide a powerful correction method for experiments with Gaussian detector resolution. Unfortunately, the resolution of LUX Run04 and post-Run4 data is not Gaussian. The pathological S2 tails make the resolutions approximately exponential to the high-energy side while leaving it roughly Gaussian on the low-energy side.

The asymmetry combined with the extended range of the resolution severely limit the effectiveness of equations 5.11 and 5.12. For this reason, we move from an analytical approach to a numerical one. The libNEST model has been fine-tuned to replicate the LUX detector resolution, so we will combine it with the model of the S2 tails described in section 4.4 to un-smear the data.

### 5.3 Measurement of Recombination Fluctuations from $^{14}\text{C}$

$$\sigma_R^2 = R(1 - R) \cdot N_i + \left( F_0 \exp \left( \frac{-(Y - F_1)^2}{2F_2^2} \right) \right)^2 N_i^2 \quad (5.13)$$

### 5.4 Yields and Recombination from Updated NEST Model

### 5.5 Measurement of the Shape of the $^{14}\text{C}$ Beta-Spectrum

## Appendix A: Alternate Doke-Plot Corrections

### A.1 No $^{37}\text{Ar}$

### A.2 Three Point Doke-Plot

## Appendix B: Alternate Tail Model

### B.1 Flat

### B.2 Poisson

## Bibliography

- [1] Live chart of nuclides. <https://www-nds.iaea.org/relnsd/vcharthtml/VChartHTML.html>. Accessed: 2017-11-21.
- [2] Mcmc and fitting models to data. <https://sciencehouse.wordpress.com/2010/06/23/mcmc-and-fitting-models-to-data/>. Accessed: 2017-11-25.
- [3] P. A. R. Ade et al. Planck 2015 results. XIII. Cosmological parameters. *Astron. Astrophys.*, 594:A13, 2016.
- [4] D. S. Akerib, S. Alsum, H. M. Araújo, X. Bai, A. J. Bailey, J. Balajthy, P. Beltrame, E. P. Bernard, A. Bernstein, T. P. Biesiadzinski, E. M. Boulton, R. Bramante, P. Brás, D. Byram, S. B. Cahn, M. C. Carmona-Benitez, C. Chan, A. A. Chiller, C. Chiller, A. Currie, J. E. Cutter, T. J. R. Davison, A. Dobi, J. E. Y. Dobson, E. Druszkiewicz, B. N. Edwards, C. H. Faham, S. Fiorucci, R. J. Gaitskell, V. M. Gehman, C. Ghag, K. R. Gibson, M. G. D. Gilchriese, C. R. Hall, M. Hanhardt, S. J. Haselschwardt, S. A. Hertel, D. P. Hogan, M. Horn, D. Q. Huang, C. M. Ignarra, M. Ihm, R. G. Jacobsen, W. Ji, K. Kamdin, K. Kazkaz, D. Khaitan, R. Knoche, N. A. Larsen, C. Lee, B. G. Lenardo, K. T. Lesko, A. Lindote, M. I. Lopes, A. Manalaysay, R. L. Mannino, M. F. Marzioni, D. N. McKinsey, D.-M. Mei, J. Mock, M. Moongwelwan, J. A. Morad, A. S. J. Murphy, C. Nehrkorn, H. N. Nelson, F. Neves, K. O'Sullivan, K. C. Oliver-Mallory, K. J. Palladino, E. K. Pease, P. Phelps, L. Reichhart, C. Rhyne, S. Shaw, T. A. Shutt, C. Silva, M. Solmaz, V. N. Solovov, P. Sorensen, S. Stephenson, T. J. Sumner, M. Szydagis, D. J. Taylor, W. C. Taylor, B. P. Tennyson, P. A. Terman, D. R. Tiedt, W. H. To, M. Tripathi, L. Tvrznikova, S. Uvarov, J. R. Verbus, R. C. Webb, J. T. White, T. J. Whitis, M. S. Witherell, F. L. H. Wolfs, J. Xu, K. Yazdani, S. K. Young, C. Zhang, and LUX Collaboration. Results from a Search for Dark Matter in the Complete LUX Exposure. *Physical Review Letters*, 118(2):021303, January 2017.
- [5] D. S. Akerib et al. The Large Underground Xenon (LUX) Experiment. *Nucl. Instrum. Meth.*, A704:111–126, 2013.

- [6] D. S. Akerib et al. Low-energy (0.7-74 keV) nuclear recoil calibration of the LUX dark matter experiment using D-D neutron scattering kinematics. 2016.
- [7] D. S. Akerib et al. Tritium calibration of the LUX dark matter experiment. *Phys. Rev.*, D93(7):072009, 2016.
- [8] D. S. Akerib et al. 3D Modeling of Electric Fields in the LUX Detector. 2017.
- [9] G. Alimonti, G. Angloher, C. Arpesella, M. Balata, G. Bellini, J. Benziger, S. Bonetti, L. Cadonati, F.P. Calaprice, G. Cecchet, M. Chen, N. Darnton, A. De Bari, M. Deutsch, F. Elisei, F. Von Feilitzsch, C. Galbiati, F. Gatti, M.G. Giannotti, D. Giugni, T. Goldbrunner, A. Golubchikov, A. Goretti, T. Hagner, F.X. Hartmann, R. Von Hentig, G. Heusser, A. Ianni, J. Jochum, M. Johnson, M. Laubenstein, P. Lombardi, S. Magni, S. Malvezzi, I. Manno, G. Manuzio, F. Masetti, U. Mazzucato, E. Meroni, M. Neff, A. Nostro, L. Oberauer, A. Perotti, A. Preda, R.S. Raghavan, G. Ranucci, E. Resconi, M. Ruscitti, R. Scardoni, S. Schnert, O. Smirnov, R. Tartaglia, G. Testera, P. Ullucci, R.B. Vogelaar, S. Vitale, and O. Zaimidoroga. Measurement of the  $^{14}\text{c}$  abundance in a low-background liquid scintillator. *Physics Letters, Section B: Nuclear, Elementary Particle and High-Energy Physics*, 422(1-4):349–358, 1998. cited By 73.
- [10] C. A. Baker et al. An Improved experimental limit on the electric dipole moment of the neutron. *Phys. Rev. Lett.*, 97:131801, 2006.
- [11] Jacob D. Bekenstein and Robert H. Sanders. A primer to relativistic MOND theory. 2005. [EAS Publ. Ser.20,225(2006)].
- [12] Denis E. Bergeron, Raphael Galea, Lizbeth Laureano-Prez, and Brian E. Zimmerman. Comparison of  $^{14}\text{c}$  liquid scintillation counting at {NIST} and {NRC} canada. *Applied Radiation and Isotopes*, 109:30 – 35, 2016. Proceedings of the 20th International Conference on Radionuclide Metrology and its Applications 811 June 2015, Vienna, Austria.
- [13] Lars Bergström. Nonbaryonic dark matter: Observational evidence and detection methods. *Rept. Prog. Phys.*, 63:793, 2000.
- [14] R. Bernabei, P. Belli, F. Cappella, V. Caracciolo, S. Castellano, R. Cerulli, C. J. Dai, A. d’Angelo, S. d’Angelo, A. Di Marco, H. L. He, A. Incicchitti, H. H. Kuang, X. H. Ma, F. Montecchia, D. Prosperi, X. D. Sheng, R. G. Wang, and Z. P. Ye. Final model independent result of dama/libra–phase1. *The European Physical Journal C*, 73(12):2648, Nov 2013.
- [15] H. A. Bethe and R. F. Bacher. Nuclear physics a. stationary states of nuclei. *Rev. Mod. Phys.*, 8:82–229, Apr 1936.

- [16] E.M. Boulton, E. Bernard, N. Destefano, B.N.V. Edwards, M. Gai, S.A. Hertel, M. Horn, N.A. Larsen, B.P. Tennyson, C. Wahl, and D.N. McKinsey. Calibration of a two-phase xenon time projection chamber with a 37 ar source. *Journal of Instrumentation*, 12(08):P08004, 2017.
- [17] F. P. Calaprice and B. R. Holstein. Weak magnetism and the beta spectra of  $^{12}\text{B}$  and  $^{12}\text{N}$ . *Nuclear Physics A*, 273:301–325, November 1976.
- [18] W. Craig Carter. 3.21 spring 2002: Lecture 08, February 2002. Accessed: 2017-07-03.
- [19] Masud Chaichian, Josef Kluso?, Markku Oksanen, and Anca Tureanu. Can TeVeS be a viable theory of gravity? *Phys. Lett.*, B735:322–326, 2014.
- [20] V Chepel and H Araujo. Liquid noble gas detectors for low energy particle physics. *Journal of Instrumentation*, 8(04):R04001, 2013.
- [21] Ryan Cooke, Max Pettini, Regina A. Jorgenson, Michael T. Murphy, and Charles C. Steidel. Precision measures of the primordial abundance of deuterium. *Astrophys. J.*, 781(1):31, 2014.
- [22] A. Dobi et al. Xenon purity analysis for EXO-200 via mass spectrometry. *Nucl. Instrum. Meth.*, A675:40–46, 2012.
- [23] Attila Dobi. *Measurement of the Electron Recoil Band of the LUX Dark Matter Detector with a Tritium Calibration Source*. PhD thesis, University of Maryland, 2014.
- [24] Attila Dobi, Clayton G Davis, Carter Hall, Thomas Langford, Simon Slutsky, and Yung-Ruey Yen. Detection of krypton in xenon for dark matter applications. *Nucl. Instrum. Meth.*, A665:1–6, 2011.
- [25] Leanne D Duffy and Karl van Bibber. Axions as dark matter particles. *New Journal of Physics*, 11(10):105008, 2009.
- [26] Loyal Durand. Electron screening corrections to beta-decay spectra. *Phys. Rev.*, 135:B310–B313, Jul 1964.
- [27] Carlos H. Faham. *Prototype, Surface Commissioning and Photomultiplier sacterization for the Large Underground Xenon (LUX) Direct Dark Matter Search Experiment*. PhD thesis, Brown University, Providence, Rhode Island, 2014.
- [28] Jonathan L. Feng. Dark matter candidates from particle physics and methods of detection. *Annual Review of Astronomy and Astrophysics*, 48(1):495–545, 2010.
- [29] A.G.M. Ferreira and L.Q. Lobo. The sublimation of argon, krypton, and xenon. *The Journal of Chemical Thermodynamics*, 40(12):1621 – 1626, 2008.

- [30] A. K. Ganguly. *Introduction to Axion Photon Interaction in Particle Physics and Photon Dispersion in Magnetized Media*. Part. Phys. 2012.
- [31] A. García and B. A. Brown. Shape of the  $\beta$  spectra in the  $a=14$  system. *Phys. Rev. C*, 52:3416–3427, Dec 1995.
- [32] H. Genz, G. Kühner, A. Richter, and H. Behrens. Phenomenological wave functions for the mass  $a=14$  system and a consistent description of beta decay observables. *Zeitschrift für Physik A Hadrons and Nuclei*, 341(1):9–24, Mar 1991.
- [33] W. C. Haxton.  $^{37}\text{Ar}$ . *Phys. Rev. C*, 38:2474–2477, Nov 1988.
- [34] Richard H. Helm. Inelastic and Elastic Scattering of 187-Mev Electrons from Selected Even-Even Nuclei. *Phys. Rev.*, 104:1466–1475, 1956.
- [35] Gerard Jungman, Marc Kamionkowski, and Kim Griest. Supersymmetric dark matter. *Phys. Rept.*, 267:195–373, 1996.
- [36] L. W. Kastens, S. Bedikian, S. B. Cahn, A. Manzur, and D. N. McKinsey. A  $^{83}\text{Kr}^m$  source for use in low-background liquid Xenon time projection chambers. *Journal of Instrumentation*, 5:5006, May 2010.
- [37] L. W. Kastens, S. B. Cahn, A. Manzur, and D. N. McKinsey. Calibration of a Liquid Xenon Detector with Kr-83m. *Phys. Rev.*, C80:045809, 2009.
- [38] Richard Knoche. *Signal Corrections and Calibrations in the LUX Dark Matter Detector*. PhD thesis, University of Maryland, College Park, Maryland, 2016.
- [39] Andriy Kurylov and Marc Kamionkowski. Generalized analysis of weakly interacting massive particle searches. *Phys. Rev.*, D69:063503, 2004.
- [40] V. V. Kuzminov and N. Ja. Osetrova. Precise measurement of 14c beta spectrum by using a wall-less proportional counter. *Physics of Atomic Nuclei*, 63(7):1292–1296, Jul 2000.
- [41] E.W. Lemmon, M.O. McLinden, and D.G. Friend. “*Thermophysical Properties of Fluid Systems*” in *NIST Chemistry WebBook, NIST Standard Reference Database Number 69*. National Institute of Standards and Technology, Gaithersburg MD, 20899. Accessed: 2017-07-13.
- [42] D. S. Leonard, A. Dobi, C. Hall, L. Kaufman, T. Langford, S. Slutsky, and Y. R. Yen. A simple high-sensitivity technique for purity analysis of xenon gas. *Nucl. Instrum. Meth.*, A621:678–684, 2010.
- [43] John Lewin and P F Smith. Review of mathematics, numerical factors, and corrections for dark matter experiments based on elastic nuclear recoil. 6, 12 1996.

- [44] LUX Collaboration, D. S. Akerib, S. Alsum, H. M. Araújo, X. Bai, A. J. Bailey, J. Balajthy, P. Beltrame, E. P. Bernard, A. Bernstein, T. P. Biesiadzinski, E. M. Boulton, P. Brás, D. Byram, S. B. Cahn, M. C. Carmona-Benitez, C. Chan, A. A. Chiller, C. Chiller, A. Currie, J. E. Cutter, T. J. R. Davison, A. Dobi, J. E. Y. Dobson, E. Druszkiewicz, B. N. Edwards, C. H. Faham, S. R. Fallon, S. Fiorucci, R. J. Gaitskell, V. M. Gehman, C. Ghag, M. G. D. Gilchriese, C. R. Hall, M. Hanhardt, S. J. Haselschwardt, S. A. Hertel, D. P. Hogan, M. Horn, D. Q. Huang, C. M. Ignarra, R. G. Jacobsen, W. Ji, K. Kamdin, K. Kazkaz, D. Khaitan, R. Knoche, N. A. Larsen, C. Lee, B. G. Lenardo, K. T. Lesko, A. Lindote, M. I. Lopes, A. Manalaysay, R. L. Mannino, M. F. Marzioni, D. N. McKinsey, D. M. Mei, J. Mock, M. Moongweluhan, J. A. Morad, A. S. J. Murphy, C. Nehrkorn, H. N. Nelson, F. Neves, K. O'Sullivan, K. C. Oliver-Mallory, K. J. Palladino, E. K. Pease, L. Reichhart, C. Rhyne, S. Shaw, T. A. Shutt, C. Silva, M. Solmaz, V. N. Solovov, P. Sorensen, S. Stephenson, T. J. Sumner, M. Szydagis, D. J. Taylor, W. C. Taylor, B. P. Tennyson, P. A. Terman, D. R. Tiedt, W. H. To, M. Tripathi, L. Tvrznikova, S. Uvarov, V. Velan, J. R. Verbus, R. C. Webb, J. T. White, T. J. Whitis, M. S. Witherell, F. L. H. Wolfs, J. Xu, K. Yazdani, S. K. Young, and C. Zhang. Limits on spin-dependent WIMP-nucleon cross section obtained from the complete LUX exposure. *ArXiv e-prints*, May 2017.
- [45] Maxim Markevitch, A. H. Gonzalez, D. Clowe, A. Vikhlinin, L. David, W. Forman, C. Jones, S. Murray, and W. Tucker. Direct constraints on the dark matter self-interaction cross-section from the merging galaxy cluster 1E0657-56. *Astrophys. J.*, 606:819–824, 2004.
- [46] N. Marquardt. Introduction to the principles of vacuum physics. 1999.
- [47] Christopher McCabe. The earth's velocity for direct detection experiments. *Journal of Cosmology and Astroparticle Physics*, 2014(02):027, 2014.
- [48] Nicholas Metropolis, Arianna W. Rosenbluth, Marshall N. Rosenbluth, Augusta H. Teller, and Edward Teller. Equation of state calculations by fast computing machines. *The Journal of Chemical Physics*, 21(6):1087–1092, 1953.
- [49] M. Milgrom. A modification of the Newtonian dynamics as a possible alternative to the hidden mass hypothesis. *apj*, 270:365–370, July 1983.
- [50] A. Moljk and S. C. Curran. Beta spectra of  $c^{14}$  and  $s^{35}$ . *Phys. Rev.*, 96:395–398, Oct 1954.
- [51] Julio F. Navarro, Carlos S. Frenk, and Simon D. M. White. The Structure of cold dark matter halos. *Astrophys. J.*, 462:563–575, 1996.
- [52] J. H. Oort. The force exerted by the stellar system in the direction perpendicular to the galactic plane and some related problems. *bain*, 6:249, August 1932.

- [53] R. D. Peccei and Helen R. Quinn. CP. *Phys. Rev. Lett.*, 38:1440–1443, Jun 1977.
- [54] Eric Roth. *Nucleation and Heat Transfer in Liquid Nitrogen*. PhD thesis, Portland State University, 1993.
- [55] V. C. Rubin, W. K. Ford, Jr., and N. Thonnard. Rotational properties of 21 SC galaxies with a large range of luminosities and radii, from NGC 4605 /R = 4kpc/ to UGC 2885 /R = 122 kpc/. *apj*, 238:471–487, June 1980.
- [56] B. Ryden. *Introduction to cosmology*. Addison-Wesley, San Francisco, USA, 2003.
- [57] P. Salucci and M. Persic. Dark matter halos around galaxies. 1996. [ASP Conf. Ser.117,1(1997)].
- [58] Richard W. Schnee. Introduction to dark matter experiments. pages 775–829, 2011.
- [59] Ch. Sonntag, H. Rebel, B. Ribbat, S. K. Thio, and W. R. Gramm. Experimental evidence for the nonstatistical shape of the beta spectrum of  $^{14}\text{C}$ . *Lettore al Nuovo Cimento (1969-1970)*, 4(15):717–719, Oct 1970.
- [60] Ian P. Stern. Axion Dark Matter Searches. *AIP Conf. Proc.*, 1604:456–461, 2014.
- [61] P. Tisserand et al. Limits on the Macho Content of the Galactic Halo from the EROS-2 Survey of the Magellanic Clouds. *Astron. Astrophys.*, 469:387–404, 2007.
- [62] P Venkataramaiah, K Gopala, A Basavaraju, S S Suryanarayana, and H Sanjeeviah. A simple relation for the fermi function. *Journal of Physics G: Nuclear Physics*, 11(3):359, 1985.
- [63] J. R. Verbus et al. Proposed low-energy absolute calibration of nuclear recoils in a dual-phase noble element TPC using D-D neutron scattering kinematics. *Nucl. Instrum. Meth.*, A851:68–81, 2017.
- [64] M. Weber and W. de Boer. Determination of the local dark matter density in our Galaxy. *aap*, 509:A25, January 2010.
- [65] F. E. Wietfeldt, E. B. Norman, Y. D. Chan, M. T. F. da Cruz, A. García, E. E. Haller, W. L. Hansen, M. M. Hindi, R.-M. Larimer, K. T. Lesko, P. N. Luke, R. G. Stokstad, B. Sur, and I. Žlimen. Further studies on the evidence for a 17-kev neutrino in a  $^{14}\text{doped germanium detector}$ . *Phys. Rev. C*, 52:1028–1040, Aug 1995.
- [66] DH Wilkinson. Evaluation of beta-decay: I. the traditional phase space factors. *Nuclear Instruments and Methods in Physics Research Section A: Accelerators, Spectrometers, Detectors and Associated Equipment*, 275(2):378–386, 1989.
- [67] F. Zwicky. On the Masses of Nebulae and of Clusters of Nebulae. *apj*, 86:217, October 1937.